# FNITE ELEMENT MODELLING
# OF
# TWO-COMPONENT, SOLID-LIQUID MIXTURES

By

MATTHEW PRINGLE, B.SC.E.

A Thesis

Submitted to the School of Graduate Studies

in Partial Fulfilment of the Requirements

for the Degree

Doctor of Philosophy

McMaster University

# FINITE ELEMENT MODELLING OF TWO COMPONENT MIXTURES

DOCTOR OF PHILOSOPHY McMaster, University
(Civil Engineering) Hamilton, Ontario

Title: Finite Element Modeling of Two-Component, Solid-Liquid Mixtures

Author: Matthew Pringle, B.Sc.E. (Queen's University)

Supervisor: Professor, D.F. Stolle

Number of Pages: xiii, 195

## ABSTRACT

The scope of this thesis is to present a framework for the modelling of two-component, liquid/solid mixtures using the finite element method. The presentation is applicable to a wide range of two-component phenomena, however, special attention is paid to the liquefaction of sandy soils which is of particular concern to the civil engineer.

In the past, much of the focus of research has been placed on the creation of models capable of capturing the mechanism of excess pore pressure development leading to liquefaction. Comparatively little attention has been placed on modelling the post-liquefaction event. This thesis provides a framework that allows the civil engineer to model soil deposits, predicting the onset of liquefaction and simulating the events that follow, namely post-liquefaction flow and the re-consolidation of the soil.

The mixtures considered in this thesis are treated as two viscous fluids having momentum exchange between them via hydrodynamic drag. Two sets of Navier-Stokes equations are used to model the two-component mixture. The thesis presents the derivation of these equations along with the closure equations required to model the hydrodynamic drag and shear stress constitutive behaviour. A simple, novel approach to modelling the compaction/dilation behaviour of granular materials under the action of shear strain is also presented. It is shown that a recasting of the equations with a new set of variables is helpful in solving the equations via standard Galerkin finite element methods. An outgrowth of this recasting is also presented, that allows, for one-dimensional problems, to reduce the variable set from four unknowns to one, greatly simplifying the solution process and computation effort.

Finally, several applications of the model are presented in order to validate the model and to demonstrate the wide range for which the model may be used.

# ACKNOWLEDGEMENTS

I would like to first thank Dr. Dieter Stolle for his supervision, advice and mostly, for his patience over the past six years. I choose to supplement my graduate education with activities important to me and I am grateful he was willing to accommodate them. I would also like to thank the Natural Sciences and Engineering Research Council without whom I likely would not have chosen the path to graduate school. I would like to thank my colleague Spencer Smith for being there all these years as we both worked through our thesis.

I would like to thank the McMaster Solar Car Team, especially Andrew Baerg, for giving me the outlet I so often needed and the United States Golf Association for their support through the completion of my thesis.

Mostly though I would like to thank my parents for the sacrifices they have made to give me the opportunities I have had, and to my wife Tracy for her love, encouragement and for helping me learn the value of me.

*"He conquers who endures"*

*- Persius*

# TABLE OF CONTENTS

**4.0 FINITE ELEMENT MODELING** (cont'd)

5.0 MODEL VERIFICATION AND ANALYSIS (cont'd)

# LIST OF FIGURES

## CHAPTER 1

## CHAPTER 2

## CHAPTER 3

CHAPTER 3 (cont'd)

CHAPTER 4

CHAPTER 5

**CHAPTER 5** (cont'd)

# 1 INTRODUCTION

Earthquakes are of particular interest to civil engineering fields as they represent one of the highest potentials for devastation of structures for which these engineers are responsible. Results of the destructive forces of earthquakes are well known to all. Therefore, the ability of the civil engineer to estimate the effects of earthquakes on their structures is vitally important.

The most obvious effect of earthquakes is the elevated loads that are imposed on buildings, dams, retaining walls, etc. A less common, but potentially more destructive, effect of earthquakes is the liquefaction of the soil on which these structures are constructed. Liquefaction occurs under the special conditions where fluid, trapped in the spaces between individual soil grains, increases in pressure under the action of the earthquake and unloads the soil skeleton. When the soil is unloaded, it loses its stiffness and behaves similarly to a very viscous fluid. This phenomenon (known as liquefaction) can lead to the rapid collapse of structures, large movement of the soil and considerable settlement.

Considerable attention has been paid to explaining and predicting the onset of liquefaction under earthquake loading. Many finite element codes have been developed to model this complex phenomenon. However, these models are not intended to estimate the response of the soil after liquefaction has occurred. Rather, the engineer is often limited to design guidelines and rules of thumb (Seed, 1987). In addition to applied mechanics approaches involving finite element modelling, practical guidelines have been investigated employing standard soil property tests such as penetration tests to evaluate potential for liquefaction (Robertson and Campanella, 1985, Ishihara, 1985, Seed and Idriss, 1982)

The intent of this study is to provide a framework within which a model may be created to study the flow of liquefied materials. In the following chapters, the results of investigations on the constitutive and finite element modelling of liquefied (and fluidized) liquid/solid mixtures is presented. The focus of this thesis is on modelling the liquefied system as a two-component fluid, with associated constitutive models, rather than on taking the more traditional approach of viewing the soil as an elasto-plastic solid.

As is often the case, in creating such a model, many unforeseen obstacles have provided opportunities to contribute to the body of knowledge both directly in the field of post-liquefaction analysis and in the related field of fluidization modelling. This chapter contains an overview of these contributions which are described in greater detail in the chapters that follow.

The following sections of this chapter provide an introduction to the phenomenon of liquefaction and show how it is a true, two-component problem. This is followed by an outline of the current state of modelling soils in the liquefied state. Next, the governing equations used in this thesis are presented. Finally, each contribution to the body of knowledge is summarized in brief.

## 1.1 Effects of Liquefaction

The loss of soil strength associated with liquefaction can have devastating effects on structures. There are many ways in which liquefied soils can cause damage:

- Loss of soil strength allows structures to overturn
- Increased pressure in soil collapses foundations and buried structures
- Loss of soil strength causes failure of soil structures such as earth dams
- Fluid nature of liquefied soil can result in landslides

There have been several major earthquakes which have caused significant damage due to liquefaction. A classical example is the 1964 Niigata earthquake where liquefaction caused the overturning of several apartment complexes as shown in Figure 1.1. In the same year, Alaska suffered a very large earthquake that caused landslides and buckling of roadways. In 1971, the San Fernando earthquake very nearly caused severe devastation. The earthquake caused the liquefaction of a very large earth dam and the soil beneath the dam. The dam barely avoided collapsing, which would have caused the flooding of downstream, populated areas. More recently, the 1995 earthquake near Kobe, Japan caused liquefaction damage to waterfront pier areas, where container handling equipment and wharf areas suffered collapse due to structural overturing and lateral spreading of the surface.

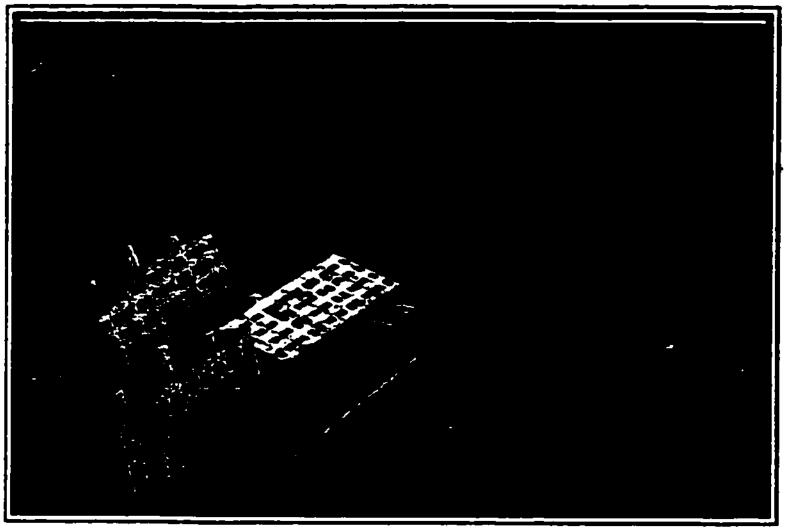

**Figure 1.1**: Overturned Buildings, Niigata, Japan, 1964 (University of Washington, Soil Liquefaction Web Site)

Liquefaction is not the only example of devastating two-component flows encountered in the field of civil engineering. The failure of tailings dams results in the flow of soil/water mixtures that can often lead to disaster (Blight, 1997, Chandler and Tosatti, 1995). Finally, it appears that there is interest in modelling the fluidization of soil in situ to determine the potential for remediating contaminated soils (Niven and Kalili, 1998). The model described herein would be suitable for such applications.

## 1.2 The Concept of Effective Stress

In this research, saturated soils (more specifically sands) will be treated as a continuum. However, referring to Figure 1.2, one must not lose sight of the fact that the soil is comprised of solid granular particles and a pore fluid (usually water and/or air). This distinction is vital to understanding the behaviour of soils subject to both self weight and external loading.

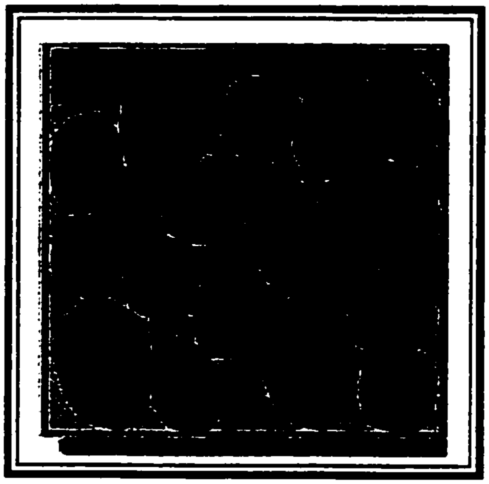

**Figure 1.2:** Soil Particles with Pore Fluid (University of Washington, Soil Liquefaction Web Site)

It has long been recognized that the shear strength of a soil, unlike many continuous materials, is highly dependent on the confining pressure applied to the particles. A common criterion to describe the condition for soil failure is the Mohr-Colomb model in which the shear strength of the soil is proportional to the normal effective stress on the failure plane in the soil. Figure 1.3 shows this relationship graphically. In a non-cohesive soil, such as sand, when the normal stress of the soil is reduced to zero, the shear resistance becomes negligible.

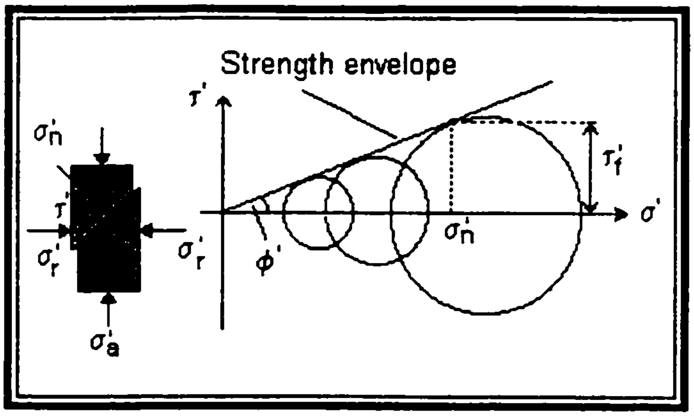

**Figure 1.3**: Mohr-Coulomb Failure Criteria (University of West England, 2000)

Consider the volume of soil shown in Figure 1.2. Using indicial notation (Malvern, 1969), the total stress in the soil, $\sigma_{ij}$, may be divided into two parts, that carried by the pressure of the pore fluid, p, and that carried by the soil skeleton, $\sigma'_{ij}$. The stress associated with the soil skeleton is referred to as the effective stress of the soil and is defined as:

$$\sigma'_{ij} = \sigma_{ij} - p\delta_{ij} \tag{1.1}$$

where compressive stresses are taken as positive here.

Terzaghi (1936) recognized that the response of the soil should be a function of the effective stress only and not the total stress. He provides the following definition:

> "the effective stress represents the part of the total stress which produces measurable effects such as compaction or an increase of shearing resistance"

Stolle (2000) provides a short review of the effective stress principle.

It follows from Terzaghi's observation that changes in effective stress (and not total stress) must, in general, be accompanied by a change in the strain of the soil skeleton. Mathematically, one may define this statement as:

$$d\sigma'_{ij} = D_{ijkl} d\varepsilon_{kl} \tag{1.2}$$

where the constitutive matrix $D_{ijkl}$ is the tangent modulus of the soil, which depends in general on the effective stress conditions and strain history (Malvern, 1969).

## 1.3 Pore Pressure Response to Straining

A sandy soil consisting of a collection of particles is packed in a certain state, with a given amount of void space (filled by water in the saturated condition). In the case of loose sands, the particles are packed in an inefficient manner with large void spaces. As the soil is strained, the particles reorient themselves in a more efficient manner, leaving less void space, provided that the fluid is free to drain.

If the soil is highly permeable, the pore fluid rapidly seeps out of the collapsing voids, making way for the more densely packed particles of the soil. Under such conditions, the pore pressure is little affected by the straining action. This type of behaviour is referred to in soil mechanics as the drained response of the soil. On the other hand, if the soil is impermeable (or if drainage is artificially prevented in the laboratory), the fluid will be unable to escape the pores. If it is assumed that the solid particles are incompressible when compared to the compressibility of the fluid, any change in the packing of the particles, must be accompanied by a compression of the pore fluid. The volumetric strain of the fluid, causes a change of fluid density proportional to the change in pressure via (Malvern, 1969):

$$dp \approx c^2 d\rho \tag{1.3}$$

where $\rho$ is the density of the fluid and c is the sound speed of the fluid.

It may be observed, that if a loose, saturated, sandy soil is strained either mechanically in a laboratory, or by the influence of an earthquake in the field, the resulting shear strains can cause an increase in the pore pressure and a decrease in the effective confining pressure in the soil skeleton. If the strains are sufficiently large and occur quickly enough, the pressure increase in the fluid may be sufficient to reduce the effective spherical stress to zero. As mentioned previously, if this occurs, the shear resistance of the soil becomes negligible, yielding a material that behaves as a viscous fluid.

Figure 1.4 shows the results of a combined centrifuge/finite element study on the response of the pore water pressure to shaking. One can observe that, as the shaking progresses, the pore fluid pressure rises to a maximum that is equal to the total stress. At this point, the soil liquefies, so that the resistance to shear is only a function of the viscosity of the mixture.

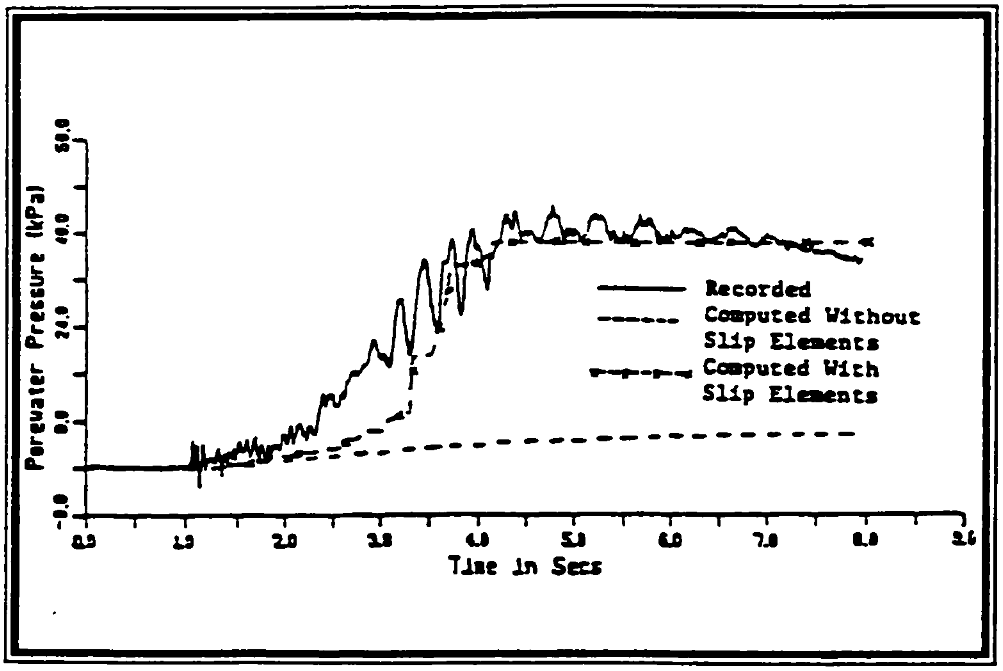

Figure 1.4: Measured and Computed Pore Pressures (NRC, 1985)

## 1.4 Liquefaction of Real Soils

In the laboratory, liquefaction is most often studied by artificially preventing the escape of pore fluid (undrained conditions). Of course, soils in situ, have a finite permeability, which allows some of the pore fluid to drain as the soil is strained. This drainage delays, or even prevents, liquefaction from occurring. The pore pressure increase depends therefore, on the following (Pande & Zienkiewicz, 1982):

- the permeability of the soil
- the distance to a free drainage point
- the rate of straining

The permeability has an obvious effect on the potential for liquefaction. If it is very high, then the fluid drains easily without significant pressure build up. Conversely, if the permeability is very low, pressure in the soil initially builds up quickly and then slowly decreases as the fluid drains and the soil settles into a new configuration (consolidation).

In a similar manner, if a drainage point is very close to a point of interest, then the fluid can drain even in a low permeability soil. Figure 1.5 demonstrates this point. This figure shows the pore pressures at various times and depths for three soils having different permeability. Although the pore pressure in the lowest permeability soil can build up to a value that is

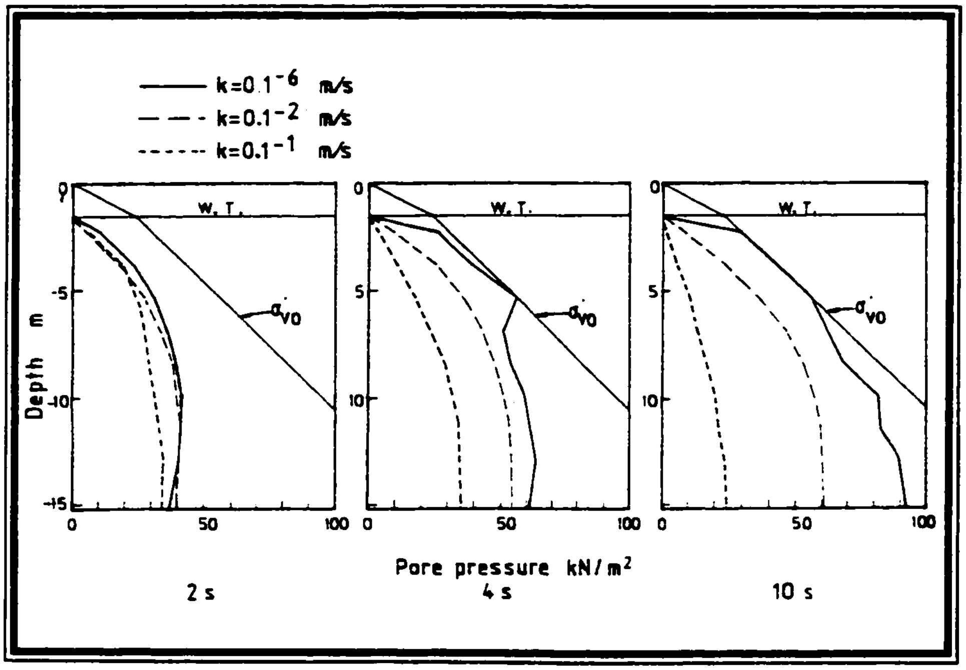

Figure 1.5: Simulated Pore Pressure Response (Pande & Zienkiewicz, 1982)

equal to the initial vertical effective stress ($\sigma'_{vo}$) at depths ranging from 1m to 6m, the pore pressure cannot build up in the top layer because of its proximity to the surface.

The time scale of straining (via a seismic event, for instance) must also be considered. If straining occurs quickly, relative to the time scale for drainage, even a very porous soil may undergo a significant pore pressure increase.

It is apparent that the phenomenon of earthquake induced liquefaction is complex and not easily modelled via continuum mechanics. In an effort to provide a simple basis for predicting liquefaction, a variety of models have been developed. For example, Davis and Berrill (1982) attempt to predict liquefaction statistically using dissipated seismic energy as a measure of the liquefaction potential. Seed forwarded an attractive idea of excess pore pressure as a function of equivalent stress cycles (Martin et al., 1975 for example).

## 1.5 Current State of Post-Liquefaction Modelling

A great deal of research has been focussed on the development of models for predicting the behaviour of soils up to the point when the soil (or a portion of the soil) liquefies. These models are capable of successfully capturing the behaviour of real soils as observed in laboratory testing and field observations; see for example, Figure 1.5. Figure 1.6 shows typical results of one of these numerical models. Owing to the incremental stress/strain form of these models, and due to the loss of static shear strength upon liquefaction, these models break down when the effective stress is zero. This may be seen in Figure 1.6, whereupon the horizontal displacement of the soil increases without bound following liquefaction.

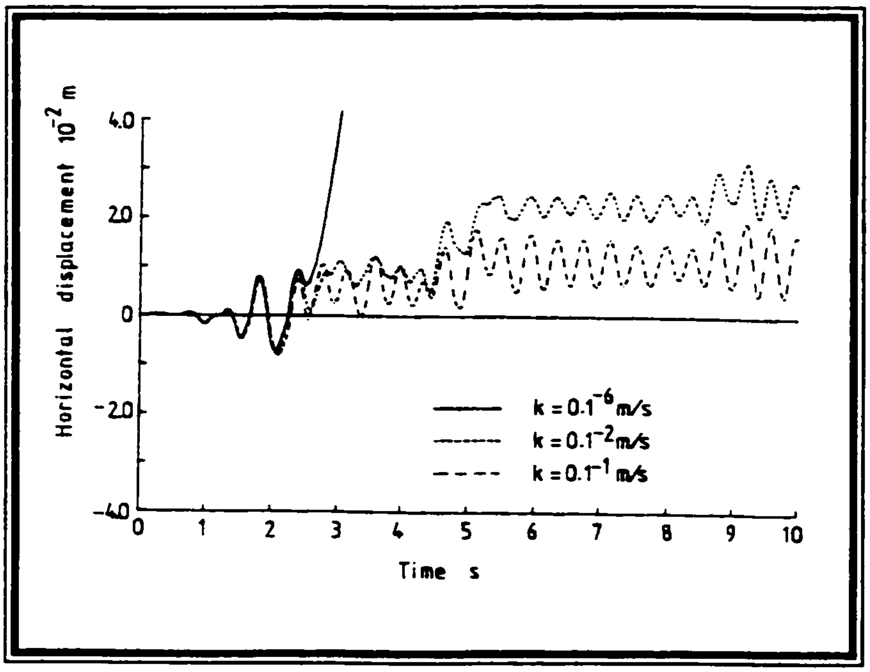

**Figure 1.6:** Typical Liquefaction Analysis Results (Pande & Zienkiewicz, 1982)

In a more recent review, (Isihara, 1993), the progress of soil modelling was outlined as shown in Figure 1.7. This chart shows that the analysis of post-liquefaction was limited to cases where the soil does not flow; ie., ground movement is caused only by settlement following consolidation of the soil. In addition to the types of analyses outlined by Isihara, there have been a limited number of attempts to model the

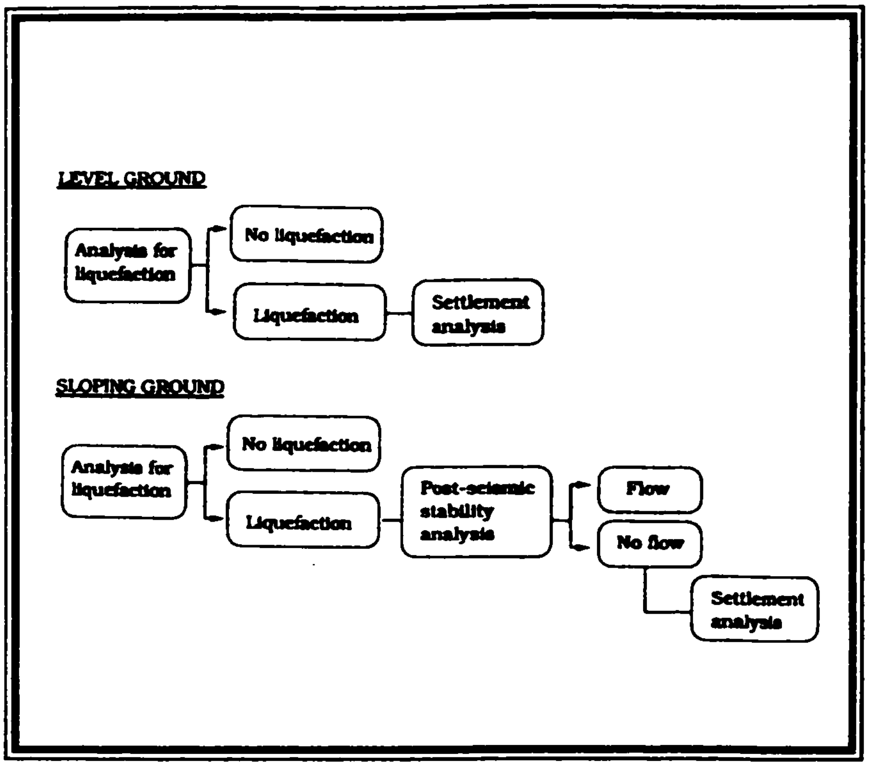

**Figure 1.7**: Flow Chart of Liquefaction Analysis (Isihara, 1993)

behaviour of soils after liquefaction. For example, Hamada et al. (1987) attempted to predict the movement of a solid surface layer "floating" on a layer of liquefied soil having zero shear strength. This layer was subject to gravity loads and boundary conditions of zero axial stress where cracks were found, since the cracks cannot resist axial loads.

Several authors (Pillai & Stewart, 1994, Pillai & Salgado, 1994, Byrne et. al., 1994, Vaid & Thomas, 1995, Talaganov, 1996, Vaid et. al., 1989, Poulos, 1981, Seed, 1979) suggest that the steady-state or residual strength concept may be used to model post-liquefaction behaviour. It is postulated, in these works, that beyond a certain level of straining, the soil maintains a fixed level of strength that depends on, among other things, the initial stress level and ratio of shear stress to normal stress. Poulos (1981) points out that the steady state strength also depends heavily on the rate of deformation of the soil (ie., flow velocity), which is consistent with an analysis based on viscous flow. A review by Ishihara (1993) outlines the significant effort that has been made over the past forty years to develop effective modelling techniques to predict liquefaction response.

In any case, analyses based on the steady strength principle fail to include the coupling between the pore pressure and the flow. From a fluid mechanics perspective, such coupling would allow the flow of liquefied soils to be driven by pressure and for the flow of the soil to potentially relieve pore pressures. A further problem with the steady state types of analyses, is that they do not consider the draining and re-consolidation of the soil after liquefaction which may be responsible for halting flows sooner than the models predict.

Only very recently has the analysis of post-liquefaction flows involved treating the liquefied material as a viscous fluid. Uzuoka et al. (1998) present a model that treats the soil as a Bingham fluid (Malvern, 1969). The shear stress to initiate flow is based on the so-called steady state stress (Castro, 1975) and the Bingham viscosity is based on the experimentally determined strain rate/stress response of sand/water mixtures. Tamte and Towhata (1999) also treat the soil as a fluid, but with a rather simplistic constant viscosity assumption.

The Bingham fluid assumption appears to be consistent with the behaviour of a fluidized saturated soil. It is also a relatively simple model to incorporate into a finite element analysis. It does however have a major drawback, in that it is difficult to reliably predict liquefaction and subsequent consolidation when the two-component nature of the soil is neglected.

## 1.6 Two-Component, Two-Phase Flow Model of Liquefied Soils

This study proposes a model where soil in a liquefied state is treated as a two-component mixture. It is shown that the model can capture, both the liquefied soil's fluid like behaviour, without neglecting the essentials of liquefaction, and consolidation.

### 1.6.1 Hydrodynamic Model

The granular and fluid components in this model are each treated as a fluid having viscous properties (referred to as a two-fluid model) with velocity, pressure and porosity being the principal unknowns of the system. The hydrodynamic model is comprised of the conservation of mass and the conservation of momentum equations, for both the solid particle and the pore fluid components. It is assumed that the soil is isothermal and hence energy conservation is not considered. These equations are the Navier-Stokes equations for each phase, amended by the addition of an interphase momentum exchange term and statement of volume conservation. The resulting four equations, summarized by Gidaspow (1994), for the five unknowns (fluid and solid velocity, $u_f$ and $u_s$, pressure $p_f$ and $p_s$, and porosity, n) are given in Table 1.1. It should be noted that the pressure terms are included in the stress tensor in the conservation of momentum equation which is discussed in later sections. Tension is defined to be positive. The nomenclature of Table 1.1 is given at the end of this chapter and a complete description of the equations is given in Chapter 2.

**Conservation of Mass for Pore Fluid Phase**

$$\frac{\partial}{\partial t}\left(n\rho_f\right) + \nabla\cdot\left(n\rho_f\bar{\mathbf{u}}_f\right) = 0$$

**Conservation of Mass for Solid Particle Phase**

$$\frac{\partial}{\partial t}\left((1-n)\rho_s\right) + \nabla\cdot\left((1-n)\rho_s\bar{\mathbf{u}}_s\right) = 0$$

**Conservation of Momentum for Pore Fluid Phase**

$$\frac{\partial}{\partial t}\left(n\rho_f\bar{\mathbf{u}}_f\right) + \nabla\cdot\left(n\rho_f\bar{\mathbf{u}}_f\bar{\mathbf{u}}_f\right) = \nabla\cdot\sigma_f + \beta\left(\bar{\mathbf{u}}_s - \bar{\mathbf{u}}_f\right) + n\rho_f\mathbf{f}$$

**Conservation of Momentum for Solid Particle Phase**

$$\frac{\partial}{\partial t}\left((1-n)\rho_s\bar{\mathbf{u}}_s\right) + \nabla\cdot\left((1-n)\rho_s\bar{\mathbf{u}}_s\bar{\mathbf{u}}_s\right) = \nabla\cdot\sigma_s + \beta\left(\bar{\mathbf{u}}_f - \bar{\mathbf{u}}_s\right) + (1-n)\rho_s\mathbf{f}$$

**Table 1.1**: Basic Hydrodynamic Equations (Gidaspow, 1994)

### 1.6.2 Expansion of The Stress Tensor

The total stress on a fluid ($\sigma_f$) or solid ($\sigma_s$) element may be divided into two parts; the deviatoric portion ($\tau$) and the mean stress portion; i.e. generically, one has (Malvern, 1969)

$$\sigma_{ij} = \tau_{ij} - \delta_{ij} p \tag{1.4}$$

where $\tau_{ij}$ is assumed to obey the following constitutive equation:

$$\tau_{ij} = 2\mu\left(\dot{\varepsilon}_{ij} - \tfrac{1}{3}\delta_{ij}\dot{\varepsilon}_{kk}\right) \tag{1.5}$$

and $\mu$ is the shear viscosity.

The rate of deformation tensor, $\dot{\varepsilon}$, may be defined in terms of the velocity gradients; i.e.,

$$\dot{\varepsilon}_{ij} = \frac{1}{2}\left(\frac{\partial u_i}{\partial x_j} + \frac{\partial u_j}{\partial x_i}\right) \tag{1.6}$$

In order to determine the stress in a fluid, therefore, the shear viscosity ($\mu$) and bulk viscosity ($\xi$) must be provided for each component under consideration. The pore fluid viscosity ($\mu_f$) may of course be found in any fluid mechanics handbook and may be treated as a constant for isothermal conditions. Furthermore, there appears to be little evidence of the existence of a bulk viscosity for fluids and this term is therefore generally ignored (Zienkiewicz & Taylor, 1991).

Unfortunately, the corresponding terms for the granular component are not as simple. It has been found, in both this and other investigations, that the viscosity for a liquid/granular solid mixture exhibits complex behaviour. This viscosity depends on the following factors:

- material properties of the granular component (size, shape, roughness, uniformity)
- liquid component properties
- proportion of the granular component suspended in the liquid
- shear rate, in mixtures with a large proportion of granular component

## CONTRIBUTION #1

The viscous behaviour of fluidized sand/water mixtures has been tested over a wide range of porosity values and over a wide range of shear rates using a Brookfield viscometer immersed in a fluidization chamber. A new correlation equation has been developed that fits the data with a very high coefficient of determination. The data collected is in good agreement with previous studies which use more complex experimental methods.

The four hydrodynamic equations (Table 1.1) allow four principal unknowns to be determined. In order to solve for the additional unknowns, the use of closure relations are required that express the additional unknowns as a function of the principal unknowns. One such additional unknown is the pressure in the granular component.

Granular material behaviour is further complicated by the fact that under the influence of shear strains, the material has a tendency to change volume (compaction or dilation). As discussed previously, this behaviour is responsible for the liquefaction during earthquakes. There are a wide range of models available for simulating this behaviour, unfortunately they tend to be complex and computationally intensive. Owing to the focus of this study on post-liquefaction behaviour, a simple alternative to the complex elasto/plastic constitutive models for soils was developed.

**CONTRIBUTION #2**

A novel constitutive model for the granular component pressure as a function of porosity has been developed. The validity of this model has been tested in the simulation of settlement experiments.

**CONTRIBUTION #3**

An artificial neural network (ANN) has been implemented to model the volume change behaviour of the granular component. This network was trained using a commercial neural network software package and the resulting non-linear matrix equations were added to the hydrodynamic equations for closure.

It is believed that this is the first use of an ANN in a transient finite element simulation to model soil volumetric strain behaviour. This model was used to analyse the liquefaction of a one-dimensional soil deposit. It provided predictions that were qualitatively similar to those obtained using more complex constitutive descriptions.

### 1.6.3 Hydrodynamic Drag

The fluid and solid components interact through the hydrodynamic drag, which transfers momentum from one phase to the other. For instance, if the fluid is travelling with high velocity and the solid particles are moving slowly, the fluid will tend to speed up the particles, while the particles will tend to slow down (or reduce the pressure of) the fluid phase. This phenomenon couples the two conservation of momentum equations and is a large source of non-linearity in the system

The drag term may be developed in several ways. A soil mechanist may choose to treat it using the conventional seepage theory of Darcy (Bear, 1972), which, for horizontal flow is

$$i = \frac{\Delta p}{\Delta x}\frac{1}{\rho g} = -\left(u_f - u_s\right)\frac{1}{k} \tag{1.7}$$

where i is the hydraulic gradient. This approach is however, generally applicable only to a narrow range of volume fractions and soil particle size.

In order to improve the above statement of Darcy's law, many authors (Pritchett et. al. 1979, Gidaspow, 1986, Bouillard et. al. 1989, Hong et. al. 1995, Boemer et. al. 1997) have chosen to model the drag with a non-linear coefficient, β.

$$n\frac{\partial p}{\partial x} = \beta\left(u_f - u_s\right) \tag{1.8}$$

where n is the porosity of the granular component. Two separate expressions for β have been used by these authors; that of Ergun (1952) for dense flow (n < 0.6) and the drag on an individual sphere for dilute flow (n > 0.6). The two expressions are discussed in detail in Chapter 3.

### 1.6.4 Revised Equation Set

In the early stages of using the hydrodynamic models for studying fluidization, it was found that the equations are highly unstable and that solutions to practical problems were very difficult to achieve.

In order to overcome this, two new variables were introduced:

$$\begin{aligned} V &= nU_f + (1-n)U_s \\ W &= nU_f - (1-n)U_s \end{aligned} \tag{1.9}$$

Chapter 2 shows that the substitution of **V** and **W** into the hydrodynamic equations linearize the originally non-linear conservation of mass equations. This linearization greatly stabilizes the solution, permitting the standard Galerkin formulation of the finite element equations. Bird, Stewart and Lightfoot (1960) report on the use of the first variable given in Equation 1.9. However, the use of both of these variables in an effort to stabilize a finite element code for two-component flow is original.

**CONTRIBUTION #4**

It has been shown in this research that replacing the primitive velocities in the hydrodynamic equations with the pseudo-velocities **V** and **W** (cross sectional averaged) creates a more stable equation set, which permits solutions to practical problems using standard finite element techniques.

### 1.6.5 Reduced Variable Model

In addition to the very significant benefit of making the conservation of mass equations linear, the use of **V** and **W**, along with discretization of the equations, permits the reduction of the full equation set to a single unknown system for one-dimensional problems.

**CONTRIBUTION #5**

For one-dimensional problems, the full hydrodynamic model has been reduced to a single unknown system. This has clear benefits with respect to solution stability and computational efficiency.

## 1.7 Summary

The objective of this thesis is to present a framework for a model of the flow of liquefied and fluidized materials. In the following chapters, the results of investigations on the constitutive and finite element modelling of liquefied (and fluidized) liquid/solid mixtures are presented.

The body of the thesis is divided into four chapters. Chapter 2 covers the presentation of the hydrodynamic model, which is a revised set of hydrodynamic equations that allow a stable solution to be achieved.

Chapter 3 is concerned with the closure relations required to solve the basic hydrodynamic equations. Specifically, the drag between the solid and liquid components and the shear stress and the volumetric strain behavior of the solid component are discussed.

Chapter 4 presents the finite element equivalent of the hydrodynamic equations. Details of the solution technique are provided along with a reduced variable equation that allows, in certain situations, for a single equation to replace the full hydrodynamic equation set.

Chapter 5 demonstrates the capacity of the model to analyze an array of flow situations, which include:

- One and two dimensional fluidization
- One dimensional settlement and consolidation
- One dimensional liquefaction

Finally, conclusions and recommendations for future work are provided in Chapter 6.

## NOMENCLATURE

| | |
|---|---|
| $c$ | Speed of sound in fluid |
| $D_{ijkl}$ | Tensor of elastic constants |
| $E_{fluid}$ | Elastic modulus of fluid component |
| $E_{solid}$ | Elastic modulus of solid component |
| $i$ | Hydraulic gradient |
| $k$ | Hydraulic conductivity |
| $n$ | Porosity |
| $p$ | Pressure |
| $p_f$ | Pressure in fluid component |
| $p_s$ | Pressure in solid component |
| $u_f$ | Velocity of fluid component |
| $u_s$ | Velocity of fluid component |
| $\mathbf{V}$ | Pseudo mixture velocity (cross sectional averaged) |
| $\mathbf{W}$ | Pseudo difference velocity (cross sectional averaged) |

### Greek Symbols

| | |
|---|---|
| $\delta_{ij}$ | Kronecker delta function |
| $\varepsilon$ | Strain tensor |
| $\dot{\varepsilon}$ | Rate of Deformation Tensor |
| $\mu$ | Viscosity |
| $\xi$ | Bulk viscosity |
| $\sigma$ | Stress tensor |
| $\sigma'$ | Effective stress tensor |
| $\sigma'_{vo}$ | Initial effective vertical stress |
| $\tau$ | Shear stress tensor |

## REFERENCES

Bear, J.
***Dynamics of Fluids in Porous Media***
Dover Publications, New York, 1972

Bird, R.B., Stewart, W.E., Lightfoot, E.N.
***Transport Phenomena***
John Wiley & Sons, New York, 1960

Blight, G.E.
***Destructive Mudflows as a Consequence of Tailings Dyke Failures***
Proc. Instn. Civ. Engrs. Geotech. Engng., Vol. 125, pp. 9 - 18, 1997

Byrne, P.M., Imrie, A.S., Morgenstern, N.R.
***Results and Implications of Seismic Performance Studies for Duncan Dam***
Can. Geotech. J., Vol. 31, pp. 979 - 988, 1994

Castro, G.
***Liquefaction and Cyclic Mobility of Saturated Sands***
J. Geotech. Eng., Vol. 101, pp. 551 - 569, 1975

Chandler, R.J., Tosatti, G.
***The Stava Tailings Dams Failure, Italy, July 1985***
Proc. Instn. Civ. Engrs. Geotech. Engng., Vol. 113, pp. 67 - 79, 1995

Davis, R.O., Berrill, J.B.
***Energy Dissipation and Seismic Liquefaction in Sands***
Earthquake Eng. And Structural Dynamics, Vol., 10, pp. 59 - 68, 1982

Gidaspow, D.
***Multiphase Flow and Fluidization, Continuum and Kinetic Theory Descriptions***
Academic Press, Boston, 1994

Hamada, M., Towhata, I., Yasuda, S., Isoyama, R.
***Study on Permanent Ground Displacement Induced by Seismic Liquefaction***
Comp & Geotech., Vol. 4, pp. 197 - 220, 1987

Ishihara, K.
***Stability of Natural Deposits During Earthquakes***
Proc. 11th Int. Conf. Soil Mech. & Foundation Eng., pp. 321 - 376, 1985

Ishihara, K.
***Liquefaction and Flow Failure During Earthquakes***
Geotechnique, Vol. 43, pp. 351 - 415, 1993

Malvern, L.E.
***Introduction to the Mechanics of a Continuous Medium***
Prentice-Hall, New Jersey, 1969

Martin, G.R., Finn, W.D.L., Seed H.B.
***Fundamentals of Liquefaction Under Cyclic Loading***
J. Geotech. Eng., Vol. 101., pp. 423 - 439, 1975

Niven, R.K., Khalili, N.
***In Situ Multiphase Fluidization ("upflow washing") for the Remediation of Hydrocarbon Contaminated Sands***
Can. Geotech. J., Vol. 35, pp. 938 - 960, 1998

(NRC) Committee on earthquake Engineering, National Research Council
***Liquefactions of Soils During Earthquakes***
National Academy Press, Washington, D.C., 1985

Pande G.N., Zienkiewicz, O.C. (Eds.)
***Soil Mechanics - Transient and Cyclic Loads***
John Wiley & Sons, 1982

Pillai, V.S, Salgado, F.M.
***Post-Liquefaction Stability and Deformation Analysis of Duncan Dam***
Can. Geotech. J., Vol. 31, pp. 967 - 978, 1994

Pillai, V.S., Stewart, R.A.
***Evaluation of Liquefaction Potential of Foundation Soils at Duncan Dam***
Can. Geotech. J., Vol. 31, pp. 951 - 967, 1994

Poulos, S.J.
***The Steady State of Deformation***
J. Geotech. Eng., Vol. 107, pp. 553 - 561, 1981

Robertson, P.K., Campanella, R.G.
***Liquefaction Potential of Sands Using the CPT***
J. Geotech. Eng., Vol. 111, pp. 384 - 403, 1985

Seed, H.B.
***Soil Liquefaction and Cyclic Mobility Evaluation for Level Ground During Earthquakes***
J. Geotech. Eng., Vol. 105, pp. 201 - 255,

Seed, H.B.
***Design Problems in Soil Liquefaction***
J. Geotech. Eng., Vol. 113, pp. 827 - 845, 1987

Seed, H.B., Idriss, I.M.
***Ground Motions and Soil Liquefaction During Earthquakes***
EERI, 1982

Stolle D.F., 2000
***Course Notes, Civil Engineering 3A03, McMaster University***
http://www.eng.mcmaster.ca/civil/undergraduate/courses/civ3a03/article.htm

Talaganov, K.V.
***Stress-Strain Transformations and Liquefaction of Sands***
Soil Dynamics and Earthquake Eng., Vol. 15, pp. 411 - 418, 1996

Tamate, S., Towhata, I.
***Numerical Simulation of Ground Flow Caused by Seismic Liquefaction***
Soil Dynamics and Earthquake Eng., Vol. 18, pp. 473 - 485, 1999

Terzaghi, K.
***The Shearing Resistance of Saturated Soils and the Angle Between Planes of Shear***
Proc. 1st Int. Conf. Soil Mech. & Foundation Eng., pp. 54 - 56, 1936

University of Washington
***Soil Liquefaction Web Site***
http://www.ce.washington.edu/~liquefaction/html/what/what1.html

University of West England
***Basic Mechanics of Soils Web Site***
http://fbe.uwe.ac.uk/public/geocal/soilmech/basic/soilbasi.htm#MECHCRITM

Uzuoka, R., Yashima, A., Kawakami, T., Konrad, J.M.
***Fluid Dynamics Based Prediction of Liquefaction Induced Lateral Spreading***
Comp. & Geotech., Vol. 22, pp. 243 - 282, 1998

Vaid, Y.P., Chung, E.K.F., Kuerbis, R.H.
***Stress Path and Steady State***
Can. Geotech. J., Vol. 27, pp. 1 - 7, 1990

Vaid, Y.P., Thomas, J.
***Liquefaction and Postliquefaction Behavior of Sand***
J. Geotech. Eng., Vol. 121, pp. 163 - 173, 1995

# 2 HYDRODYNAMIC MODEL

The laws of mass, momentum and energy conservation are the most widely used principles in engineering and science. They provide the fundamental governing relations for the class of problems considered in this thesis and therefore a review of their derivation will prove useful to the understanding of the specific, two-phase flow models that are developed later.

As mentioned in the opening chapter, the class of problem addressed is comprised of two components; a fluid component and a granular solid component, which consists of discrete particles. Given the small size and large number of solid particles, it is assumed, that their behavior may be averaged in such a way that the principles of continuum mechanics apply. This assumption is consistent with the work of many previous researchers (Bear, 1972).

This chapter presents a series of partial differential equations that model the flow behavior of a two-component mixture of a granular material and a fluid. These equations have been used extensively in other studies to model fluidized beds. Although the use of the spatial description outlined here may be considered uncharacteristic for the analysis of soil liquefaction, it has been used extensively in other studies to model fluidization (Boemer et al., 1997, Di Felice, 1994, for example). The main purpose of adopting this framework, rather than the usual Lagrangian description, is to better model the behavior of a soil that can flow in a liquefied condition.

## 2.1 The General Conservation Equation

In many engineering analyses, the conservation of specific properties such as mass, momentum and energy is vital to understanding the behavior of a system. The problems addressed in this research consider the conservation of both mass and momentum. It is useful therefore, to first consider the conservation of a generic property and then derive specific equations for the conservation of mass and momentum. It is assumed that the systems addressed in this study are isothermal and energy conservation is therefore not considered. The reader should note that the exposition presented in this section follows loosely that of Brodkey and Hershey (1988).

Consider the concentration of a generic quantity ($\psi$) (amount of the property per unit volume) and the associated flux ($\mathbf{\Psi}$) of this quantity (quantity of the property transferred per unit area per unit time). For example, when considering heat transfer, the concentration $\psi$ would be the amount of heat per unit volume, and the flux, $\mathbf{\Psi}$ would be the flow rate of this heat. In order to simplify the presentation, let us restrict ourselves to a two-dimensional volume of unit thickness (such as that shown in Figure 2.1), given by:

$$dV = 1 \cdot dx \cdot dy = dx \cdot dy \tag{2.1}$$

Although the presentation is in two dimensions, the vector form of the equations apply to three dimensions as well.

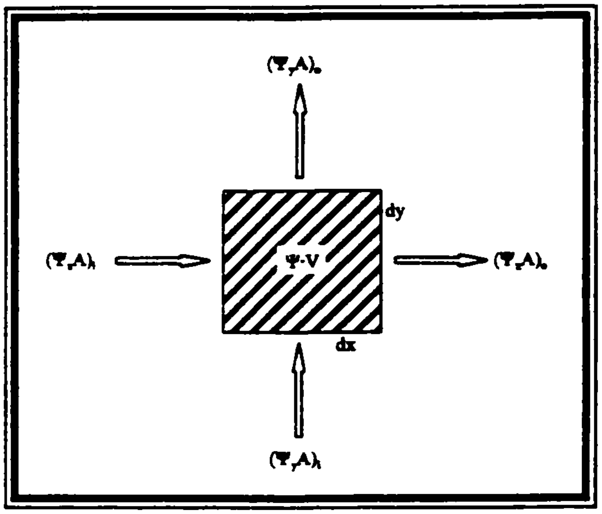

**Figure 2.1**: General Property Balance for a Two-dimensional Region

In general, the balance of influx, outflux and internal generation of a property results in a net change in accumulation of this property. The rate of accumulation and internal generation of a generic property within the region (dV) may be written as

$$\frac{\partial \psi}{\partial t} \cdot dV \tag{2.2}$$

and

$$\dot{\psi}_G \cdot dV \tag{2.3}$$

respectively, with the net flux of the property into (or out of) the region given by:

$$\Psi_{x_i} \cdot dy + \Psi_{y_i} \cdot dx - \Psi_{x_o} \cdot dy - \Psi_{y_o} \cdot dx \tag{2.4}$$

(noting again that $\Psi$ is the flux associated with the property $\psi$)

Now, applying a first order Taylor's expansion:

$$\begin{aligned} \Psi_{x_o} &= \Psi_{x_i} + \frac{\partial \Psi_x}{\partial x} \cdot dx \\ \Psi_{y_o} &= \Psi_{y_i} + \frac{\partial \Psi_y}{\partial y} \cdot dy \end{aligned} \tag{2.5}$$

and substituting equation 2.5 into equation 2.4 yields the net flux into the region:

$$-\left(\frac{\partial \Psi_x}{\partial x} + \frac{\partial \Psi_y}{\partial y}\right) dx \cdot dy \tag{2.6}$$

Since the net flux plus the internal generation must equal the accumulation of the property, we have:

$$\frac{\partial \psi}{\partial t} \cdot dx \cdot dy = \dot{\psi}_G \cdot dx \cdot dy - \left(\frac{\partial \Psi_x}{\partial x} + \frac{\partial \Psi_y}{\partial y}\right) dx \cdot dy \tag{2.7}$$

or,

$$\frac{\partial \psi}{\partial t} = \dot{\psi}_G - \nabla \cdot \Psi \tag{2.8}$$

Equation 2.8 is the conservation equation in its most general form.

A generic property can move (transport) via two processes; through molecular level interactions (such as heat conducting through a body due to molecular interaction) or by physically moving the quantity from one location to another. These modes of transferring the quantity ($\psi$) are referred to as diffusion and convection, respectively (Brodkey and Hershey, 1988).

The process of diffusion is a complex phenomenon. Fortunately, it has been found that the flux generated is often proportional to the gradient of the property, as in Fourier's Law for heat conduction, Fick's Law for mass diffusion and Newton's Law for laminar flow for example; i.e.,

$$\Psi_{diffusion} = -\vartheta \nabla \psi \qquad \textbf{(2.9)}$$

where ($\vartheta$) is a constant of proportionality (thermal conductivity ($k$), as an example).

The rate with which the property is transferred convectively is simply the concentration multiplied by the velocity at which it is traveling, i.e.:

$$\Psi_{convection} = \psi \mathbf{U} \qquad \textbf{(2.10)}$$

where $\mathbf{U}$ is the velocity vector of the quantity.

Substituting equations 2.9 and 2.10 into equation 2.8, we arrive at a general expression for the conservation of ($\psi$).

$$\frac{\partial \psi}{\partial t} = \dot{\psi}_G + \nabla \cdot \left( \vartheta \nabla \psi - \psi \mathbf{U} \right) \qquad \textbf{(2.11)}$$

Equation 2.11 is the basis for the equations used to describe the flow of the two-component systems considered in this study.

## 2.2 Single Component Systems

A description of the mass and momentum equations for a single component system is given first, in order to simplify the presentation. Thereafter, the extension of these equations to two phases is presented.

### 2.2.1 Conservation of Mass

For a single component system, the concentration of mass is simply the mass per unit of volume; i.e., density ($\psi = \rho$). In this study, there is no internal generation or dissipation of mass. The constant of proportionality is often represented by the symbol D, the diffusion constant (Brodkey and Hershey, 1988). Therefore, the mass conservation equation analogous to equation 2.11 for a single component is:

$$\frac{\partial\rho}{\partial t} = \nabla \cdot \left(D\nabla\rho - \rho\mathbf{U}\right) \qquad \textbf{(2.12)}$$

For incompressible fluids, $\nabla \cdot \rho = 0$, so equation 2.12 becomes the familiar conservation of mass equation for a single component, incompressible fluid:

$$\frac{\partial\rho}{\partial t} = -\rho\nabla \cdot \mathbf{U} \qquad \textbf{(2.13)}$$

## 2.2.2 Conservation of Momentum

Newton observed that the momentum of a body is conserved. The same has been shown to be true for all physical systems. Therefore, we may apply the general conservation equation to the momentum concentration ($\psi = \rho\mathbf{U}$). Unlike the conservation of mass however, there will be internal momentum generation and dissipation. This topic and the diffusion of momentum will be discussed below. It should be noted that the quantity $\psi$ is now a vector.

### *(i) Momentum Diffusion*

It has been found that the momentum flux due to molecular interaction (diffusion) is related to the deviatoric stress in the fluid ($\tau$) (Malvern, 1969). The deviatoric stress in a viscous fluid is:

$$\tau = \mu\left[\nabla\mathbf{U} + \mathbf{U}\nabla - \tfrac{2}{3}\nabla\cdot\mathbf{U}\mathbf{I}\right] \tag{2.14}$$

where $\mu$ is the viscosity which, depending on the particular material, may be a function of such quantities as shear rate, pressure, etc. The momentum diffusion is therefore taken as

$$\vartheta\,\nabla\,\psi = \nabla\cdot\tau \tag{2.15}$$

### *(ii) Momentum Generation*

For the moment, let us consider an element of ideal fluid with negligible viscosity, having distributed normal and body forces acting upon it (as shown in Figure 2.2).

For incompressible fluids, Newton's Second law requires, in the x-direction for example, that

$$P_x \cdot dy - \left(P_x + \Delta P_x\right) \cdot dy + F_x\rho \cdot dx \cdot dy = \rho \cdot dx \cdot dy \cdot \frac{dU_x}{dt} \tag{2.16}$$

A similar relation may be formed for the y-direction.

Recalling that

$$\Delta P_x \approx \frac{\partial P_x}{\partial x} \cdot \partial x \tag{2.17}$$

and dividing by dx·dy yields

$$-\frac{dP_x}{dx} + F_x\rho = \rho\frac{dU_x}{dt} \tag{2.18}$$

and if the fluid is incompressible, this relation reduces to

$$-\frac{dP_x}{dx} + F_x\rho = \frac{d\rho U_x}{dt} = \dot{\psi}_{G_x} \tag{2.19}$$

Note that the vector equivalent of equation 2.19 is

$$\dot{\psi}_G = -\nabla P + \rho\mathbf{F} \tag{2.20}$$

The presence of a pressure gradient and/or body forces (such as gravity) may be interpreted as internal generation of momentum and substituted into the conservation equation as such. In traditional developments of the momentum balance equation, the stresses are treated in a force balance, which must be in equilibrium with both the body forces and the acceleration of the fluid element. However, the treatment presented here attempts to explain the stresses in a manner consistent with the generic property balance containing diffusion, generation and convection.

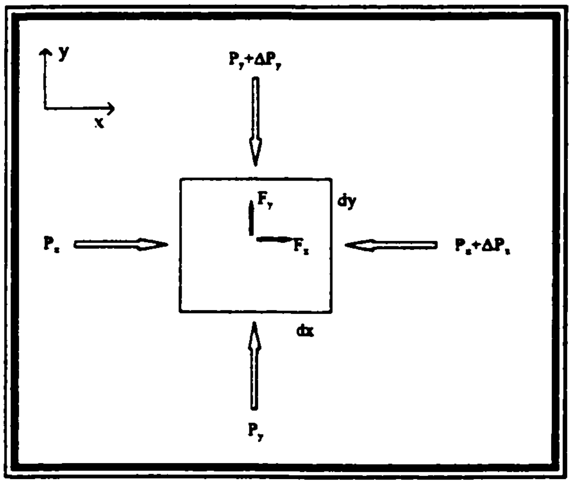

**Figure 2.2**: Normal Forces and Body Loads

### *(iii)* *Momentum Balance Equation for a Single Phase Fluid*

Substituting $\psi = \rho \mathbf{U}$ and equations 2.15 and 2.20 into the general property balance equation, eq 2.11, yields the momentum balance equation for a single component fluid:

$$\frac{\partial(\rho\mathbf{U})}{\partial t} = -\nabla P + \rho\mathbf{F} + \nabla\cdot\left(\tau - \rho\mathbf{U}\mathbf{U}\right) \tag{2.21}$$

## 2.3 Two-Component Systems

As previously mentioned, the problems addressed in this research deal primarily with two component systems. The equations describing the flow of such mixtures are very similar to those describing single component systems. The differences are primarily:

- separate mass and momentum conservation equations for each component
- control volume occupied by two components
- exchange of momentum (but not mass) between components

The sections that follow outline the additional terms that are added to the basic conservation equations.

### 2.3.1 Porosity Defined

In single component systems, the control volume is occupied by only one material. However, in two component systems, that volume is shared by two materials. In general flow scenarios of two-component mixtures, the proportion of the two components will vary both temporally and spatially. As a result, a new variable has to be defined to monitor these proportions. In fluidization and soil mechanics, there are a few choices for such a variable. Porosity (n) has been selected here.

Porosity (or void fraction, $\varepsilon_f$, in some sources) is defined as the proportion of the total volume occupied by the continuous fluid phase; i.e. (Holtz and Kovacs, 1981):

$$n = \frac{V_{void}}{V_{total}} = \frac{V_{void}}{V_{void} + V_{particles}} \tag{2.22}$$

The range of porosity is from 0 (100% solid component) to 1 (100% fluid component). Clearly, if there are only two components in the control volume, then that space not taken by one component must be occupied by the other. Therefore,

$$\frac{V_{particles}}{V_{total}} = 1 - \frac{V_{void}}{V_{total}} = 1 - n \tag{2.23}$$

### 2.3.2 Mass Conservation Equations for Two Component Systems

The mass concentration of each of the two components in a control volume is the density of the component multiplied by the proportion of the space occupied by that component. The mass concentration of each component, then, is

$$\begin{aligned} \psi_f &= n \cdot \rho_f \\ \psi_s &= (1-n) \cdot \rho_s \end{aligned} \tag{2.24}$$

By substituting these equations into the general conservation equation (eq. 2.11), the conservation of mass equations (known as the continuity equations) for the fluid and solid components, are as follows

$$\begin{aligned} \frac{\partial\left(n\rho_f\right)}{\partial t} &= -\nabla \cdot \left(D\nabla\left(n\rho_f\right) - n\rho_f \mathbf{U}_f\right) \\ \frac{\partial\left((1-n)\rho_s\right)}{\partial t} &= -\nabla \cdot \left(D\nabla\left((1-n)\rho_s\right) - (1-n)\rho_s \mathbf{U}_s\right) \end{aligned} \tag{2.25}$$

The velocities $\mathbf{U}_f$ and $\mathbf{U}_s$ in equation 2.25, refer to the actual velocities of the components, and not-mass averaged velocities.

### *(i) Discussion of the Diffusion of Mass in Solid/Fluid Systems*

Included in the continuity equations (equation 2.25) are the diffusion terms (assuming constant diffusivity coefficient):

$$D\nabla\left(n\rho_f\right), \quad D\nabla\left((1-n)\rho_s\right)$$

For the solid/liquid systems, such as those addressed in this study, it is reasonable to assume that both components are incompressible such that the diffusion terms become:

$$\rho_f D\nabla\left(n\right), \quad \rho_s D\nabla\left(1-n\right)$$

These terms suggest that the presence of a gradient in the void fraction ***may*** be sufficient to induce a flux of the individual components. This phenomenon was possibly first observed by Richards (1906) when photographs of fluidized beds revealed a wider dispersion of particles than would be predicted by segregation due to variations in particle size alone. Several researchers (Kennedy and Bretton, 1966, Yutani and Fan, 1985, Dutta et al., 1988) have investigated this phenomenon and attribute it to the random movement of particles due to stochastic variation in the properties of individual particles.

It is certainly reasonable to assume that such variations and hence such diffusion will occur in any and all fluidized systems. However, it has been observed that the diffusion coefficient is small (order $10^{-4}$ m$^2$/s) and becomes even smaller as porosity is reduced. Therefore diffusion due to porosity gradients will be ignored in this study. The resulting continuity equations thus become:

$$\begin{aligned}
&\frac{\partial(n\rho_f)}{\partial t}+\nabla\cdot(n\rho_f\mathbf{U}_f)=0\\
&\frac{\partial((1-n)\rho_s)}{\partial t}+\nabla\cdot((1-n)\rho_s\mathbf{U}_s)=0
\end{aligned} \tag{2.26}$$

which for a system with uniform material properties yields:

$$\begin{aligned}
&\frac{\partial n}{\partial t}+\nabla\cdot(n\mathbf{U}_f)=0\\
&\frac{\partial(1-n)}{\partial t}+\nabla\cdot((1-n)\mathbf{U}_s)=0
\end{aligned} \tag{2.27}$$

The presence of mass diffusion in fluidized and liquefied systems presents an intriguing concept. It is suggested that this area, in the context of a diffusion coefficient for continuum models, would be an interesting area of study for improving such models in cases where this phenomenon may be important to the overall flow.

### 2.3.3 Momentum Conservation Equations for Two-Component Systems

Similar to the mass conservation equation, the presence of multiple components in the flow slightly complicates the momentum conservation equation. In the case of a two component mixture, the conserved properties are

$$\begin{aligned}
\psi_f&=n\rho_f\mathbf{U}_f\\
\psi_s&=(1-n)\rho_s\mathbf{U}_s
\end{aligned} \tag{2.28}$$

Both components have nearly identical equations for momentum conservation. However, there is a key difference in the treatment of pressure relating to the averaging of the granular solid component as was discussed earlier.

### *(i) Pressure in the Individual Components*

The stress in the single phase fluid is divided into a deviatoric (or shear) portion and a spherical portion, usually referred to as pressure. The same stress division is applied to the individual constituents of a two-component flow.

The fluid component pressure ($P_f$) is real and exerts itself on both the fluid and solid components. Each granular particle may be considered a buoyant body, and so any pressure gradient in the fluid will result in a net force exerted on the particle. The solid component pressure ($P_s$) on the other hand, is a contrived term, which is defined as the averaging of contact forces between individual granular particles. Since these contact forces are not transmitted to the fluid component, neither will the solids component pressure be transmitted. Further explanation of this pressure is provided in the following chapter.

### *(ii) Momentum Source (or sink) Through Hydrodynamic Drag*

Whenever a fluid phase is moving with a velocity different than that of the solid particle phase, there is a hydrodynamic drag force exerted by one phase on the other. Consider a solid/fluid mixture. In the absence of acceleration, velocity gradients and self weight, the momentum equation for the fluid component reduces to (in the y-direction for example):

$$-\frac{d\left(nP_f\right)}{dy}+\dot{M}_{D_y}=0 \tag{2.29}$$

that is, the pressure drop in the fluid is equal to the momentum flux lost to the solid phase through hydrodynamic drag. In order to conserve the overall momentum of the mixture, any loss from one phase must equal the gain to the other phase. This momentum source (or sink) is represented by $\dot{\mathbf{M}}_D$.

A dot has been introduced to reinforce the notion that the pressure drop is function of the rate of momentum loss. This term is discussed further in the following chapter.

### *(iii)* *Conservation of Momentum Equations for the Individual Components*

The resulting conservation of momentum equations for the fluid and granular solid components, respectively, are

$$\frac{\partial\left(n\rho_f\mathbf{U}_f\right)}{\partial t}=-\nabla\left(nP_f\right)+n\rho_f\mathbf{F}+\dot{\mathbf{M}}_D+\nabla\cdot\left(n\tau_f-n\rho_f\mathbf{U}_f\mathbf{U}_f\right) \tag{2.30}$$

and

$$\begin{aligned}\frac{\partial\left((1-n)\rho_s\mathbf{U}_s\right)}{\partial t}&=-\nabla\left((1-n)P_f+P_s\right)+(1-n)\rho_s\mathbf{F}-\dot{\mathbf{M}}_D\\&\quad+\nabla\cdot\left((1-n)\tau_s-(1-n)\rho_s\mathbf{U}_s\mathbf{U}_s\right)\end{aligned} \tag{2.31}$$

These equations, combined with the continuity equations, equation 2.27, form the set of simultaneous relations that must be solved to predict the flow response of a two component system. The corresponding unknowns are the fluid component velocity ($\mathbf{U}_f$), the solid particle component velocity ($\mathbf{U}_s$), the fluid pressure ($\mathbf{P}_f$) and the porosity ($\mathbf{n}$). Quantities such as $\tau_s$, $\tau_f$, and $\mathbf{P}_s$ are functions of these unknowns. These quantities will be addressed in detail in Chapter 3.

Several researchers have applied the conservation equations to develop solutions for complex flows of fluidized materials in the chemical process areas. Jackson (1963),Pritchett et al. (1978), Gidaspow (1986) and Ding (1990) are widely cited and provide good insight into the utility of this model. Gidaspow (1994) provides an excellent introduction and summary of the formulation as well as various forms of constitutive models. However, the research described in this thesis appears to be the first to use such a form in the modeling of soil/fluid systems under liquefaction conditions.

Reviewing equations 2.30 and 2.31 reveals several coefficients and secondary unknowns that must be determined as functions of the primary unknowns. These include the fluid phase shear stress ($\boldsymbol{\tau}_f$), the solid phase shear stress ($\boldsymbol{\tau}_s$), the momentum source (and sink) term due to hydrodynamic drag ( $\dot{\mathbf{M}}_D$ ) and the solids phase pressure ($\mathbf{P}_s$). A portion of this research is dedicated to collecting expressions for these via the following

- direct implementation of previous findings reported in the literature
- re-interpreting previous findings reported in the literature that were intended for application in other systems
- development of new concepts

## 2.4 Revised Hydrodynamic Model

A simple finite element solution of the hydrodynamic equations (equations. 2.27, 2.30 and 2.31) of a simple, cross sectional averaged, one-dimensional flow scenario was performed to determine whether a stable solution can be found. In this simple analysis, a column containing a fluidized mixture was subjected to a step change in the inlet flow velocity of the fluid. A schematic representation of this is given in Figure 2.3.

In this simple example, a tube containing the mixture is fluidized by the fluid flowing through a porous plate at the bottom of the tube. At time $t=t_0$, the fluid flow rate is increased causing a disturbance to propagate upwards through the mixture. At $t = t_{1/2}$, the disturbance has traveled halfway up the bed. Finally, at $t = t_1$, the bed has reached a new equilibrium porosity level.

In the preliminary numerical analyses, it was very difficult (usually impossible) to achieve a stable solution for even this simple problem. It was found that the numerical instability developed quickly with porosity taking on unrealistic values. To overcome these difficulties, the equations were re-arranged in conjunction with newly defined variables to reduce the non-linearity of the equation set.

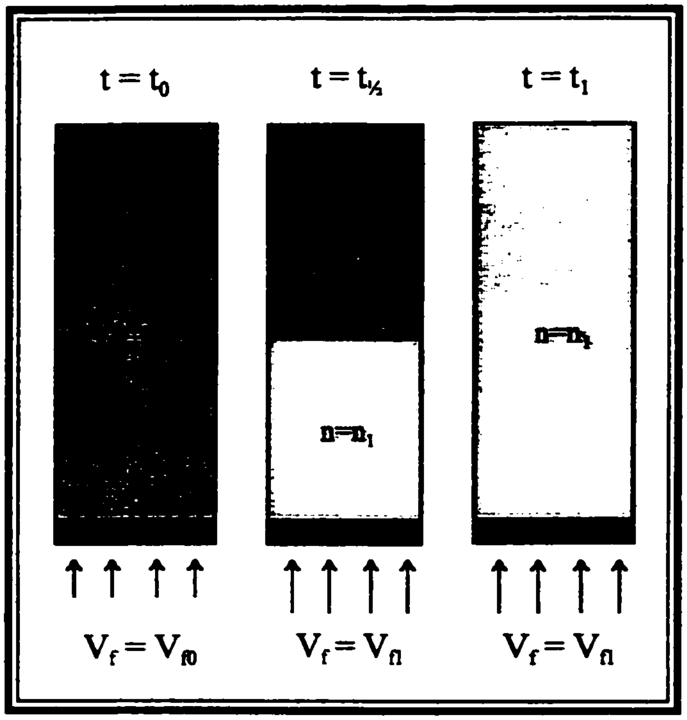

**Figure 2.3**: Simple, One-Dimensional Fluidization Analysis

### 2.4.1 Revised Continuity Equations

Recall the continuity equations (equation 2.26):

$$\frac{\partial\left(n\rho_f\right)}{\partial t} = -\nabla\cdot\left(n\rho_f\mathbf{U}_f\right)$$
$$\frac{\partial\left((1-n)\rho_s\right)}{\partial t} = -\nabla\cdot\left((1-n)\rho_s\mathbf{U}_s\right) \tag{2.32}$$

assuming that the fluid and solid are incompressible, and noting that ∇·(1-n) = -∇·n, equation 2.32 simplifies to

$$\begin{aligned} &\frac{\partial n}{\partial t}+\nabla\cdot\left(n\mathbf{U}_f\right)=0 \\ -&\frac{\partial n}{\partial t}+\nabla\cdot\left((1-n)\mathbf{U}_s\right)=0 \end{aligned} \qquad \textbf{(2.33)}$$

These two equations can be summed to

$$\nabla\cdot\left[n\mathbf{U}_f+(1-n)\mathbf{U}_s\right]=0 \qquad \textbf{(2.34)}$$

whereas taking their difference results in

$$2\frac{\partial n}{\partial t}+\nabla\cdot\left[n\mathbf{U}_f-(1-n)\mathbf{U}_s\right]=0 \qquad \textbf{(2.35)}$$

Two new variables are introduced at this time

$$\begin{aligned} \mathbf{V}&=n\mathbf{U}_f+(1-n)\mathbf{U}_s \\ \mathbf{W}&=n\mathbf{U}_f-(1-n)\mathbf{U}_s \end{aligned} \qquad \textbf{(2.36)}$$

Substituting these new variables into the revised continuity equations yields

$$\begin{aligned} \nabla\cdot\mathbf{V}&=0 \\ 2\frac{\partial n}{\partial t}+\nabla\cdot\mathbf{W}&=0 \end{aligned} \qquad \textbf{(2.37)}$$

Whereas the original continuity equations are non-linear, due to the coupling of velocity and porosity, equations 2.37 are uncoupled, linear partial differential equations. This improvement greatly simplifies the solution process.

The reader may recognize that the pseudo-velocity $\mathbf{V}$ is the area averaged volume flux of the mixture whereas the pseudo-velocity $\mathbf{W}$ may be interpreted as the area averaged volume flux of the fluid with respect to the solid. In any case, both $\mathbf{V}$ and $\mathbf{W}$ may be regarded as numerical conveniences, created to achieve the linearization objectives.

### 2.4.2 Conservation of Momentum Equations

Recalling the original conservation of momentum equations

$$\frac{\partial\left(n\rho_f\mathbf{U}_f\right)}{\partial t}=-\nabla\left(nP_f\right)+n\rho_f\mathbf{F}+\dot{\mathbf{M}}_D+\nabla\cdot\left(n\tau_f-n\rho_f\mathbf{U}_f\mathbf{U}_f\right)\qquad\textbf{(2.38)}$$

and,

$$\begin{aligned}\frac{\partial\left((1-n)\rho_s\mathbf{U}_s\right)}{\partial t}&=-\nabla\left((1-n)P_f+P_s\right)+(1-n)\rho_s\mathbf{F}-\dot{\mathbf{M}}_D\\&\quad+\nabla\cdot\left((1-n)\tau_S-(1-n)\rho_s\mathbf{U}_s\mathbf{U}_s\right)\end{aligned}\qquad\textbf{(2.39)}$$

The addition of these two momentum equations yields

$$\begin{aligned}&\frac{\partial\left[n\rho_f\mathbf{U}_f+(1-n)\rho_s\mathbf{U}_s\right]}{\partial t}=-\nabla P_f-\nabla P_s+\left[n\rho_f+(1-n)\rho_s\right]\mathbf{F}\\&+\nabla\cdot\left[n\tau_f+(1-n)\tau_s\right]-\nabla\cdot\left[n\rho_f\mathbf{U}_f\mathbf{U}_f+(1-n)\rho_s\mathbf{U}_s\mathbf{U}_s\right]\end{aligned}\qquad\textbf{(2.40)}$$

Observing that

$$n\mathbf{U}_f = \frac{\mathbf{V}+\mathbf{W}}{2}, \quad (1-n)\mathbf{U}_s = \frac{\mathbf{V}-\mathbf{W}}{2} \tag{2.41}$$

and substituting these into equations 2.38 and 2.40, the two revised momentum conservation equations become

$$\begin{aligned}&\frac{\rho_f}{2}\frac{\partial}{\partial t}\left[\mathbf{V}+\mathbf{W}\right]+\frac{\rho_f}{2}\nabla\cdot\left[\mathbf{V}\mathbf{U}_f+\mathbf{W}\mathbf{U}_f\right]-\frac{1}{2}\nabla\cdot\left[\tau_{f_v}+\tau_{f_w}\right]\\&+\nabla(nP)+\dot{\mathbf{M}}_{D_w}-\rho_f n\mathbf{g}=0\end{aligned} \tag{2.42}$$

for the fluid phase, and

$$\begin{aligned}&\frac{\partial}{\partial t}\left[\mathbf{V}\left(\frac{\rho_s+\rho_f}{2}\right)-\mathbf{W}\left(\frac{\rho_s-\rho_f}{2}\right)\right]-\frac{1}{2}\nabla\cdot\left[\tau_{s_v}-\tau_{s_w}\right]+\nabla P_f\\&+\nabla P_s+\nabla\cdot\left[\mathbf{V}\left(\frac{\rho_s\mathbf{U}_s+\rho_f\mathbf{U}_f}{2}\right)-\mathbf{W}\left(\frac{\rho_s\mathbf{U}_s-\rho_f\mathbf{U}_f}{2}\right)\right]-\bar{\rho}\mathbf{g}=0\end{aligned} \tag{2.43}$$

for the mixture with $\bar{\rho}$ being the bulk density of the mixture.

***Note:*** ***The specific form of equations 2.42 and 2.43 takes advantage of a simplification stemming from the discretization process. The reader is referred to chapter 4 for more details.***

## 2.5 Summary

A general conservation equation was developed in this chapter. This general equation served as the foundation for the development of a set of hydrodynamic equations for a single component fluid. This in turn provided a basis for the development of partial differential equations to describe the flow of a two-component mixture of granular solids and a continuous fluid (summarized in Table 2.1). A new, more stable set of equations was developed to facilitate a numerical solution.

The set of four equations requires additional closure relations to be solved. These include relations for the shear stress in both components and the pressure in the granular solid component. These relations are developed in the following chapter.

**Conservation of Mass**

$$\nabla \cdot \mathbf{V} = 0$$

$$2\frac{\partial n}{\partial t} + \nabla \cdot \mathbf{W} = 0$$

**Conservation of Momentum**

$$\frac{\rho_f}{2}\frac{\partial}{\partial t}[\mathbf{V} + \mathbf{W}] + \frac{\rho_f}{2}\nabla \cdot \left[\mathbf{V}\mathbf{U}_f + \mathbf{W}\mathbf{U}_f\right] - \frac{1}{2}\nabla \cdot \left[\tau_{f_v} + \tau_{f_w}\right] + \nabla(nP) + \dot{\mathbf{M}}_{D_w} - \rho_f n\mathbf{g} = 0$$

$$\frac{\partial}{\partial t}\left[\mathbf{V}\left(\frac{\rho_s + \rho_f}{2}\right) - \mathbf{W}\left(\frac{\rho_s - \rho_f}{2}\right)\right] - \frac{1}{2}\nabla \cdot \left[\tau_{s_v} - \tau_{s_w}\right] + \nabla P_f + \nabla P_s$$
$$+\nabla \cdot \left[\mathbf{V}\left(\frac{\rho_s\mathbf{U}_s + \rho_f\mathbf{U}_f}{2}\right) - \mathbf{W}\left(\frac{\rho_s\mathbf{U}_s - \rho_f\mathbf{U}_f}{2}\right)\right] - \bar{\rho}\mathbf{g} = 0$$

**Table 2.1**: Summary of Reformulated Hydrodynamic Equations

## NOMENCLATURE

| | |
|---|---|
| dV | Elemental volume (scalar) $(L^{3})$ |
| D | Mass diffusion constant $(L^{2}\cdot t^{-1})$ |
| **F** | Body force (vector) $(F\cdot M^{-1})$ |
| $\mathbf{M}_D$ | Momentum source (or sink) due to hydrodynamic drag (vector) $(F\cdot L^{-3})$ |
| n | Void Ratio (scalar) (dimensionless) |
| P | Pressure (scalar) $(F\cdot L^{-2})$ |
| **U** | Velocity (vector) $(L\cdot t^{-1})$ |
| **V** | Mixture pseudo-velocity (vector) $(L\cdot t^{-1})$ |
| $V_{particles}$ | Volume occupied by granular particles (scalar) $(L^{3})$ |
| $V_{total}$ | Volume occupied by granular particles and fluid (scalar) $(L^{3})$ |
| $V_{void}$ | Volume occupied by fluid (scalar) $(L^{3})$ |
| **W** | Difference pseudo-velocity (vector) $(L\cdot t^{-1})$ |

### Greek Symbols

| | |
|---|---|
| $\delta$ | Diffusion coefficient of proportionality (scalar) (units depend on application) |
| $\mu$ | Viscosity (scalar) $(F\cdot t\cdot L^{-2})$ |
| $\psi$ | Concentration of a general quantity (scalar) $(X\cdot L^{-3})$ |
| $\psi_G$ | Internal generation of $\psi$ (scalar) $(X\cdot L^{-3}\cdot t^{-1})$ |
| $\boldsymbol{\Psi}$ | Flux of $\psi$ (vector) $(X\cdot L^{-2}\cdot t^{-1})$ |
| $\boldsymbol{\Psi}_{diffusion}$ | Flux of $\psi$ attributed to diffusion (vector) $(X\cdot L^{-2}\cdot t^{-1})$ |
| $\boldsymbol{\Psi}_{convection}$ | Flux of $\psi$ attributed to convection (vector) $(X\cdot L^{-2}\cdot t^{-1})$ |
| $\rho$ | Density (scalar) $(M\cdot L^{-3})$ |
| $\boldsymbol{\tau}$ | Shear stress (2nd order tensor) $(F\cdot L^{-2})$ |
| $\boldsymbol{\tau}_{pq}$ | Shear stress of component p based on pseudo-velocity q (2nd order tensor) $(F\cdot L^{-2})$ (p = f,s; q = f,s) |

## NOMENCLATURE (CONT'D)

### Operator

| | |
|---|---|
| $\nabla A$ | $A_{k,m}$ where A is a vector field |

### Subscripts

| | |
|---|---|
| f | denotes fluid component |
| s | denotes solid component |

## REFERENCES

Bear, J.
***Dynamics of Fluids in Porous Media***
Diver Publications, New York, 1972

Boemer, A., Qi, H., Renz, U.
***Eulerian Simulation of Bubble Formation at a Jet in a Two-Dimensional Fluidized Bed***
Int. J. Multiphase Flow, Vol. 23, pp. 927-944, 1997

Brodkey, R.S., Hershey, H.C.
***Transport Phenomena: A Unified Approach***
Mc-Graw Hill, New York, 1988

Di Felice, R.
***The Voidage Function for Fluid-Particle Interaction Systems***
Int. J. Multiphase Flow, Vol. 20, pp. 153-159, 1994

Ding.J., Gidaspow, D.
***A Bubbling Fluidization Model Using Kinetic Theory of Granular Flow***
A.I.Ch.E.J., Vol. 36, pp. 523-538, 1990

Dutta, B.K., Bhattacharya, S., Chaudhury, S.K., Barman, B.
***Mixing and Segregation in a Liquid Fluidized Bed of Particles with Different Size and Density***
Can. J. Ch. Eng., Vol. 66, pp. 676-680, 1988

Gidaspow, D.
***Hydrodynamics of Fluidization and Heat Transfer: Supercomputer Modelling***
Appl. Mech. Rev., Vol. 39, pp. 1-23, 1986

Gidaspow, D.
***Multphase Flow and Fluidization: Continuum and Kinetic Theory Descriptions***
Academic Press, Boston, 1994

Holtz, R.D., Kovacs, W.D.
***An Introduction to Geotechnical Engineering***
Prentice Hall, New Jersey, 1981

Jackson, R.
***The Mechanics of Fluidised Beds: Part 1: The Stability of the State of Uniform Fluidisation***
Trans. Instn. Chem, Engrs., Vol. 41, pp. 13-21, 1963

Jackson, R.
***The Mechanics of Fluidised Beds: Part 2: The Motion of Fully Developed Bubbles***
Trans. Instn. Chem, Engrs., Vol. 41, pp. 22-28, 1963

Kennedy, S.C., Bretton, R.H.
***Axial Dispersion of Spheres Fluidized with Liquids***
A.I.Ch.E.J., Vol. 12, pp. 24-30, 1966

Malvern, L.E.
***Introduction to the Mechanics of a Continuous Medium***
Prentice Hall, New Jersey, 1969

Pritchett, J.W., Blake, T.R., Sabodh, K.G.
***A Numerical Model of Gas Fluidised Beds***
A.I.Ch.E. Symp. Ser., Vol. 74, pp. 134-148, 1978

Richards, R.H.
***A Textbook on Ore Dressing***
McGraw-Hill, New York, 1906

Yutani, N., Fan, L.T.,
***Mixing of Randomly Moving Particles in Liquid-Solid Fluidized Beds***
Powder Tech., Vol. 42, pp. 145-152, 1985

# 3 CLOSURE EQUATIONS

In the preceding chapter, the equations for the conservation of mass and momentum were developed for a two component mixture comprised of a granular solid component and a fluid component. Recall that the mass conservation equations are:

$$\begin{gathered} \nabla \cdot \boldsymbol{V} = 0 \\ 2\frac{\partial n}{\partial t} + \nabla \cdot \boldsymbol{W} = 0 \end{gathered} \tag{3.1}$$

and the momentum conservation equations are

$$\begin{gathered} \frac{\rho_f}{2}\frac{\partial}{\partial t}[\boldsymbol{V} + \boldsymbol{W}] + \frac{\rho_f}{2}\nabla \cdot \left[\boldsymbol{V}\boldsymbol{U}_f + \boldsymbol{W}\boldsymbol{U}_f\right] - \frac{1}{2}\nabla \cdot \left[\boldsymbol{\tau}_{f_V} + \boldsymbol{\tau}_{f_W}\right] \\ + \nabla\left(nP_f\right) + \dot{\boldsymbol{M}}_{D_W} - \rho_f n\boldsymbol{g} = \boldsymbol{0} \end{gathered} \tag{3.2}$$

for the fluid phase, and

$$\begin{gathered} \frac{\partial}{\partial t}\left[\boldsymbol{V}\left(\frac{\rho_s + \rho_f}{2}\right) - \boldsymbol{W}\left(\frac{\rho_s - \rho_f}{2}\right)\right] - \frac{1}{2}\nabla \cdot \left[\boldsymbol{\tau}_{s_V} - \boldsymbol{\tau}_{s_W}\right] + \nabla P_f \\ + \nabla P_s + \nabla \cdot \left[\boldsymbol{V}\left(\frac{\rho_s\boldsymbol{U}_s + \rho_f\boldsymbol{U}_f}{2}\right) - \boldsymbol{W}\left(\frac{\rho_s\boldsymbol{U}_s - \rho_f\boldsymbol{U}_f}{2}\right)\right] - \bar{\rho}\boldsymbol{g} = \boldsymbol{0} \end{gathered} \tag{3.3}$$

for the mixture. All symbols used above are the same as defined in the preceding chapter.

Reviewing these equations reveals the need for additional relations in order that only the mixture pseudo-velocity (V), the difference pseudo-velocity (**W**), the fluid pressure ($P_f$) and the porosity (n) remain as unknowns. These additional relations are known as closure equations. For this particular model, the following closure equations are required for:

- Hydrodynamic drag ( $\dot{\mathbf{M}}_D$ )
- Fluid component shear stress ($\tau_f$)
- Solid component pressure ($P_s$)
- Solid component shear behavior ($\tau_s$)

Individual relations are presented, for each quantity, in the following sections.

## 3.1 Momentum Source (or sink) Through Hydrodynamic Drag

Whenever the fluid phase is moving with a velocity different from that of the solid particle phase, there is a hydrodynamic drag force exerted by one phase on the other. One can consider, for example, a solid/fluid mixture. In the absence of acceleration, velocity gradients and gravity, the momentum equation (in the y-direction for example) for the fluid component reduces to

$$\frac{d(nP_f)}{dy} + \dot{M}_{D_y} = 0 \tag{3.4}$$

indicating that, the pressure drop in the fluid is equal to the momentum flux lost to the solid phase through hydrodynamic drag. Of course, in order to conserve the overall momentum of the mixture, any loss from one phase must exactly equal the gain to the other phase. Considerable attention has been paid to the quantization of this hydrodynamic drag. Owing to the fact that a large number of successful relations available in the literature, it was decided that selected relations would be adopted in this study rather than attempting to develop new ones in this area.

As is common, the hydrodynamic correlations adopted in this study are separated according to the porosity regime of the two component mixture. See, for example, Bird et al. (1960), Gidaspow (1986), Gidaspow (1994). In this study two regimes are used:

- dilute conditions ($0.6 \leq n \leq 1.0$)
- dense conditions ($0.3 < n < 0.6$)

### 3.1.1 Dense Conditions

Most drag correlations found in the fluidized bed literature for dense conditions have their basis in early research on pressure loss through packed and sediment beds. These are found extensively in chemical process industries and in soil mechanics (especially for dense solids ratios).

It was recognized by early researchers that the pressure loss can be attributed to two sources in this regime; (i) viscous losses and (ii) kinetic energy losses due to turbulent flow around the particles (Ergun, 1952). Blake, as reported in Carman (1937) presents correlations based on two dimensionless groups

$$\frac{\Delta P}{\rho U^2}\frac{d_p}{L}\frac{n^3}{1-n} \quad and \quad \frac{\Delta P}{\rho U^2}\frac{d_p}{L}\frac{n^3}{1-n}\frac{d_p \rho U}{\mu(1-n)} \tag{3.5}$$

for kinetic and viscous losses, respectively (where $d_p$ is a representative particle diameter and L is the length (height) of the bed).

Carmen recognized that the correlations of Blake reduces to the Kozeny equation for low flow velocities

$$\frac{\Delta P}{L} = k_1 \frac{(1-n)^2}{n^3} \frac{\mu U}{d_p^2} \tag{3.6}$$

(with $k_1$=180, civil engineers commonly use equation 3.6 to find a correlation for permeability with state parameters and fundamental material properties). U is the discharge relative velocity between the fluid and solid phases.

For high velocities, Blake (Carmen, 1937) proposes

$$\frac{\Delta P}{L} = k_2 \frac{1-n}{n^3} \frac{\rho U^2}{d_p} \tag{3.7}$$

As a direct extension of equations 3.6 and 3.7 for a more general range of flow velocities, Ergun (1952) proposes the following equation, widely used for packed beds, which has found acceptance among some researchers in modeling fluidized bed systems

$$\frac{\Delta P}{L} = \left[ 150 \frac{(1-n)^2}{n^3} \frac{\mu U}{d_p^2} + 1.75 \frac{(1-n)}{n^3} \frac{\rho U^2}{d_p} \right] \tag{3.8}$$

Equation 3.8 is limited due to the narrow porosity range tested by Ergun; i.e., $n \approx 0.4$. As a result, the appropriateness of applying equation 3.8 to intermediate situations ($0.6 \leq n \leq 0.8$) as many researchers do, may be questioned. In this study, the use of equation 3.8 is limited strictly to dense flow situations where porosity is below 0.6.

Equation 3.8, in its current form, is not suitable for direct substitution into the hydrodynamic equations. It must first be modified somewhat. Recalling equation 3.4 and assuming uniform porosity, one may write

$$\frac{dP}{dy} = \frac{\dot{M}_{D_y}}{n} \tag{3.9}$$

Although the choice of the form for the model of $\dot{\mathbf{M}}_D$ is somewhat arbitrary, it is convenient to select one of the unknowns in the hydrodynamic equations as an independent variable

$$\dot{M}_D \equiv \beta \cdot V_r \tag{3.10}$$

where β is an experimentally determined drag coefficient and $\mathbf{V}_r$, the relative velocity between the granular solid component and the fluid component. Relating the relative velocity to the superficial relative velocity (U) via

$$U = V_r n \tag{3.11}$$

allows us to establish an expression for β. Substituting equations 3.11 into 3.8, 3.9 into 3.4 and equating the results, yields the following

$$\beta = 150\frac{(1-n)^2}{n}\frac{\mu_f}{d_p^2} + 1.75\frac{(1-n)}{n}\frac{\rho_f|V_r|}{d_p} \tag{3.12}$$

It is important to recognize that this relation for β is assumed to be applicable for packed bed conditions only.

In the case of slow flow ($R_e$<1), equation 3.12 simplifies to

$$\beta = 150\frac{(1-n)^2}{n}\frac{\mu_f}{d_p^2} \tag{3.13}$$

which reduces the non-linearity of the drag term when compared with equation 3.12. Figure 3.1 shows the variation of drag coefficient with porosity and flow velocity for a specific particle size and sphericity.

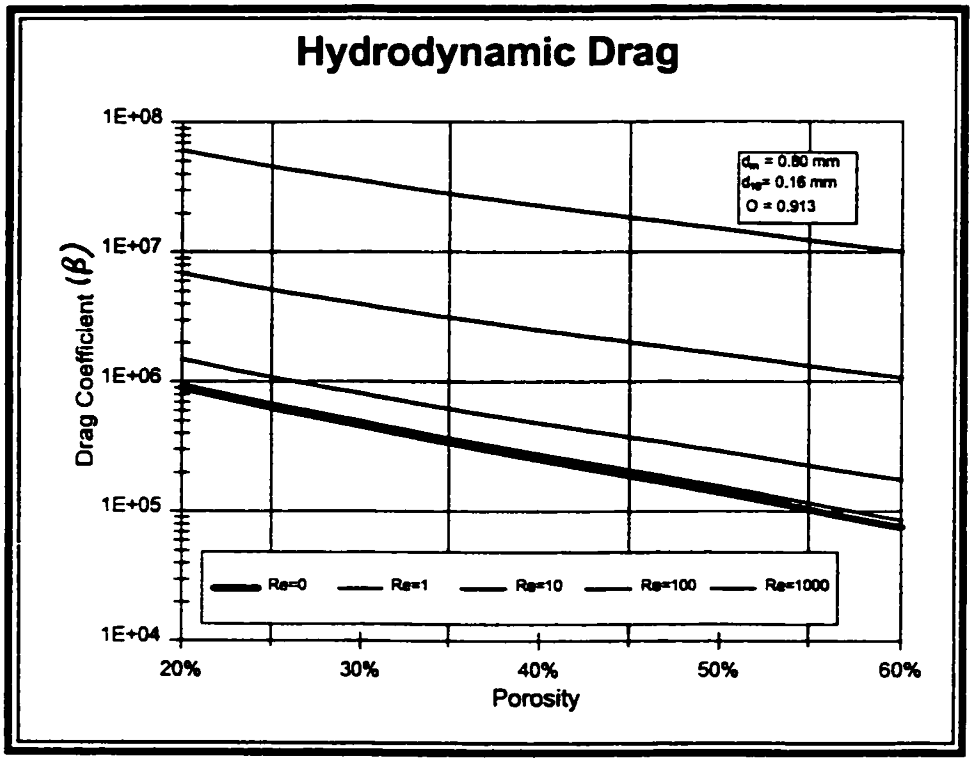

Figure 3.1: Drag Coefficient for Dense Flow Conditions

### 3.1.2 Dilute Conditions

Richardson and Zaki (1954) provide an approach for determining pressure loss through a fluidized bed for dilute conditions. In their work, they analyze the terminal velocity of particles, determined through both fluidization and sedimentation experiments, to determine pressure losses. Consider, for example, a spherical particle of diameter $d_p$, with density $\rho_s$, falling through a fluid having a density $\rho_f$ and a viscosity $\mu_f$. The buoyant weight of the particle is

$$W_p = \frac{\pi d_p^3}{6}(\rho_s - \rho_f)g \tag{3.14}$$

with, the upward force due to the hydrodynamic drag on a single isolated sphere being given by

$$F_D = \frac{1}{2}C_D\rho_f V_r^2 \tag{3.15}$$

where $V_r$ is the relative velocity between the fluid and the particle and $C_D$ is the coefficient of drag on a single, isolated particle. Richardson and Zaki show that, in the range of the porosity considered ($0.65 \le n \le 1.0$), the upward force on a particle within a suspension of similar particles ($F_U$) can be related to that of an isolated particle by the relation:

$$\frac{\hat{F}_D}{F_D} = \frac{\hat{C}_D}{C_D} = f(n) \tag{3.16}$$

where $C_D$ is the coefficient of drag on a single particle.

In steady fluidization or sedimentation (no acceleration of the solid particles) the upward force must equal the downward weight of the particle, therefore

$$V_r^2 = \frac{\pi}{3} d_p^3 (\rho_s - \rho_f)\, g \frac{1}{\rho_f\, C_D\, f(n)} \tag{3.17}$$

Now, when the solid particles are fully suspended in a steady, stationary suspension, the pressure drop must equal the weight of the suspension; i.e:

$$-\frac{dP}{dy} = \left[(1-n)\rho_s + n\rho_f\right] g \tag{3.18}$$

Once again, consider equation 3.4, for steady, uniform mixtures, where

$$\frac{dP}{dy} = \frac{\dot{M}_D}{n} \tag{3.19}$$

and

$$\dot{M}_D = \beta \cdot V_r \tag{3.20}$$

One obtains, after substituting equations 3.20, 3.4 and 3.17 into 3.18

$$\beta\left[\frac{4}{3} d_p (\rho_s - \rho_f) \frac{g}{\rho_f\, C_D\, f(n)}\right] = -\left[(1-n)\rho_s + n\rho_f\right] g V_r \tag{3.21}$$

After rearranging terms, β is given by

$$\beta = \frac{3}{4} \frac{\rho_f\, C_D\, f(n)}{d_p} \left[\frac{\rho_s}{\rho_s - \rho_f} - n\right] \left|V_r\right| n \tag{3.22}$$

Over a wide range of porosities and flow regimes, Richardson and Zaki found that

$$f(n) = n^{-3.65} \tag{3.23}$$

According to Rowe (1961), the drag coefficient for an isolated sphere is

$$C_D = \begin{cases} \frac{24}{R_e}\left(1 + 0.15 R_e^{0.687}\right), & R_e < 1000 \\ 0.44, & R_e \geq 1000 \end{cases} \tag{3.24}$$

where the Reynolds number is defined as

$$R_e = \frac{\rho_f V_r d_p}{\mu_f} \tag{3.25}$$

The findings of Richardson and Zaki were later updated by Kahn and Richardson (1987, 1990) to include a correction in the intermediate range of $0.2 < R_e < 500$. Since the simulations of this study are limited, in general, to low Reynold's number flows, this correction is not considered in this thesis.

### *(i) A Modification to the Richardson-Zaki Relation*

A controversial topic (Gibilaro & Foscolo, 1984, Clift et al., 1987, Gibilaro et al., 1987) in the development of drag correlations for fluidization and sedimentation is the so-called buoyancy force ($F_b$) on the particle. Any introductory fluid mechanics textbook will show this force to be given by:

$$F_b = \rho_f g \frac{\pi d_p^3}{6} \tag{3.26}$$

However, this force is not strictly due to "the volume of fluid displaced" as is sometimes indicated, but rather is due to the asymmetric pressure distribution on the body due to the pressure gradient is given by:

$$\frac{dP}{dy} = -\rho_f g \tag{3.27}$$

that occurs in a **static** fluid column. Equation 3.26 is a convenient expression for highly specific, although quite common conditions.

Strictly speaking, equation 3.27 applies only for the case of an isolated particle suspended or moving in a homogenous fluid. In the steady fluidization or sedimentation (the conditions under which the measurements of Richardson and Zaki are made), the fluid pressure gradient is

$$\frac{dP}{dy} = -\left[(1-n)\rho_s + n\rho_f\right] g \tag{3.28}$$

This pressure gradient is real and measurable by a piezometer and is not simply localized around individual particles. By recognizing that the pressure gradient in the fluid is given by equation 3.28, the buoyant weight of the particle becomes

$$W_p' = \frac{\pi d_p^3}{6} n\left(\rho_s - \rho_f\right) g \tag{3.29}$$

not that given in eq. 3.14.

When the correct net weight on the particle is introduced, equation 3.17 becomes

$$V_r^2 = \frac{\pi}{3} d_p^3 \left(\rho_s - \rho_f\right) g \frac{1}{\rho_f C_D f'(n)} \tag{3.30}$$

In order for this expression to match the data of Richardson and Zaki,

$$f'(n) = n^{-4.65} \tag{3.31}$$

the drag coefficient becomes

$$\beta = \frac{3}{4}\frac{\rho_f\, C_D\, f'(n)}{d_p}\left[\frac{\rho_s}{\rho_s - \rho_f} - n\right]|V_r|n^2 \tag{3.32}$$

### (ii) Simplification of the Modified Richardson-Zaki Drag Coefficient

For low Reynolds number flows, equation 3.24 reduces to Stokes Law for flow around a sphere, that is

$$C_D = \frac{24}{R_e} = \frac{24\mu_f}{\rho_f\, V_r\, d_p} \tag{3.33}$$

Substituting this into equation 3.32 yields

$$\beta = 18\frac{\mu_f\, f'(n)}{d_p^2}\left[\frac{\rho_s}{\rho_s - \rho_f} - n\right]n^2 \tag{3.34}$$

which substantially reduces the non-linearity of the drag term. Equation 3.34 is plotted in figure 3.2 for typical properties found in this study.

### (iii) A Note on Drag Correlations for General Fluidization

The data collected by Richardson and Zaki (1954), as well as numerous other investigators have a common limitation. The data was collected at the steady state fluidization or sedimentation velocity for a particular porosity value. In general however, the relative fluid velocity may not be limited to the sedimentation velocity due to the inertia of the particles.

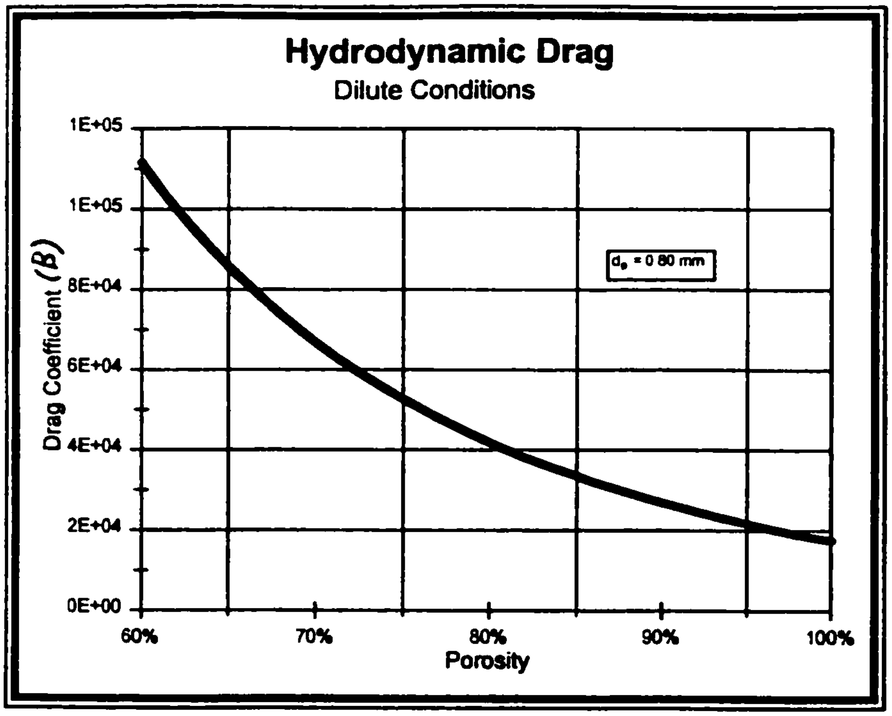

**Figure 3.2**: Hydrodynamic Drag for Dilute Conditions

In other words, under steady conditions of fluidization, each state of porosity has an associated relative velocity between the particle and the fluid. On the other hand, for more general fluidization conditions, this is not the case. Transient conditions will result in other relative velocities, either greater and less than those of steady fluidization. The correlations summarized here are therefore extrapolations beyond the test conditions.

It is recommended that future work be devoted to determining the accuracy of the drag correlations at various porosities, for relative velocities that differ from the steady fluidization values.

## 3.2 Shear Stress in the Fluid Component

The fluid under investigation in this study is water, which may be treated as a Newtonian fluid. Therefore, the shear stress ($\tau_{ij}$) in this component is simply:

$$\tau_{f_{ij}} = 2\mu_f\left(\dot{\varepsilon}_{ij} - \delta_{ij}\frac{\dot{\varepsilon}_{kk}}{3}\right) \tag{3.35}$$

where $\mu_f$ is the temperature dependant viscosity of the water and $\dot{\varepsilon}_{ij}$ is the rate of deformation tensor. Malvern (1969) provides an excellent description of the stress/strain rate behavior in viscous fluids.

## 3.3 Constitutive Modeling of the Granular Phase

In contrast to the simplicity of the fluid component, the granular component is a complex material with behavior dependent on a wide range of conditions. Any reasonable model has to accommodate these conditions. The shear stress-strain behavior is highly non-linear and shear straining in a packed bed of granular material is accompanied by volumetric straining that is the cause of liquefaction as outlined in the introductory chapter. Therefore, modeling this medium presents significant challenges. The objective of this section is to develop equations to describe the shear stress and volumetric straining when shear strains are applied.

Findings reported in the literature (Henriksen & Østergaard, 1974, Darton, R.C., 1985,Cheremisinoff, 1984, Jeffrey & Acrivos, 1976, Schügerl et al., 1961, Savage and McKeown, 1983, Tsuchiya et al., 1997) and experiments carried out for this study suggest that the shear stress in the granular component can be characterized by two distinct regimes:

- Newtonian, porosity dependent, viscous region
- Non-linear, shear-rate dependent region.

The description of the behavior of the granular component in these two regions is outlined below. This is followed by a description of the modeling of the volumetric strain behavior.

### 3.3.1 Newtonian Region

It is regularly reported in the literature (Tsuchiya, 1997 for a recent example) that for low solids concentration, a mixture of a fluid and a granular solid component behaves as a Newtonian fluid. That is, the shear stress is proportional to the shear strain rate (via the viscosity). Owing to the Newtonian behavior of the mixture, albeit with a porosity-dependent viscosity, the characterization of this behavior has tended towards simple correlations of viscosity to solids concentration.

A large number of references in the literature that report the results of various measurements of viscosity as a function of solids concentration for a wide variety of granular and fluid materials. To describe each is beyond the scope of this research. It is sufficient to outline the following:

- the rheological properties of liquid/granular mixtures
- the procedures used to measure such a quantity

- the results for materials similar to those of interest in this research

## *(i) Variability of Rheology for Granular/Fluid Mixtures*

Although, somewhat dated, Rutgers (1962) provides a comprehensive survey of many previously published experimental findings on the viscosity of granular solids suspended in Newtonian fluids. The results of this work are summarized in Figure 3.3. The following summary provides some key insight into the behavior of liquid-solid mixtures as identified in his report:

- Newtonian behavior of the liquid-solid mixture may be expected up to a solids concentration of at least 25% and possibly as high as 45%
- For solids concentration below 20%, the relative viscosity (that is, the viscosity of the mixture normalized by the viscosity of the fluid component) for all mixtures is grouped within one order of magnitude. Above this concentration however, there is very high dispersion of the data.
- Each individual combination of liquid and granular material has a unique porosity/viscosity.
- The Newtonian behavior depends on "loose and random" contacts between solid particles, as one would expect, without any "structure" forming between the solid grains.

These findings provide limits for the expected region of Newtonian behavior and motivation for determining the viscosity/porosity relationship for the material of interest in this research.

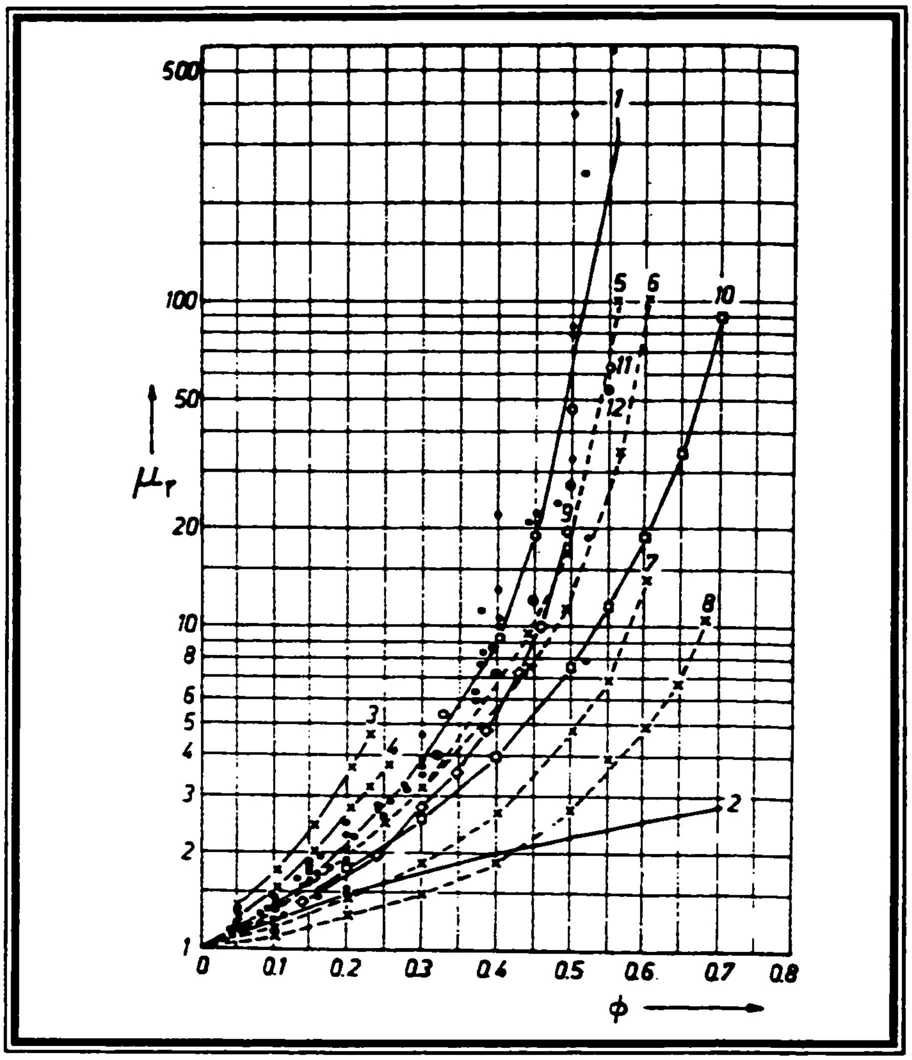

Figure 3.3: Viscosity/Solids Volume Fraction Dependancy (Rutgers, 1962)

## (ii) *Viscosity Measurement*

There are three methods commonly used for the measurement of viscosity in mixtures of granular solids with fluids.

- Couette parallel plate viscometer (Savage & McKeown, 1983, Schügerl et al., 1961)
    - Brookfield type viscometer
    - Rising bubble (Henriksen & Østergaard, 1974, Tsuchiya et al., 1997)

The vast majority of the measurements for fluidized beds reported in the literature use the third method. This method is described in detail in Darton and Harrison (1974) and more recently in Tsuchiya et al. (1997). In brief, the experiment is based on the assumption that the viscosity of the mixture may be estimated from the rise velocity of a bubble using a Stokes flow approximation, with the realization of course that the bubble diameter grows as the bubble rises through the mixture.

The shear stress measurement used in both the Couette and Brookfield devices, on the other hand, allow a more direct determination of the mixture viscosity and precise control over shear rate. Owing to these advantages, a Brookfield device was selected for this research. The Brookfield device was chosen over the Couette type as it is believed that it would be difficult, if not impossible, to properly fluidize a mixture uniformly, given the close proximity of the walls of the rotor and stator in a Couette device. The use of direct measurement also allows the findings of this research to be compared to that of similar materials measured by others via the rising bubble method.

Although Brookfield type devices have been used to investigate the rheological properties of suspensions, its use in determining properties of liquefied sands is unique.

### *(iii)* *Experimental Viscosity Measurement*

A device was designed and fabricated to allow the fluidization of sand in water, and to allow the viscosity of this mixture to be measured by a Brookfield type viscometer. Figure 3.4 shows schematically the operation of the device.

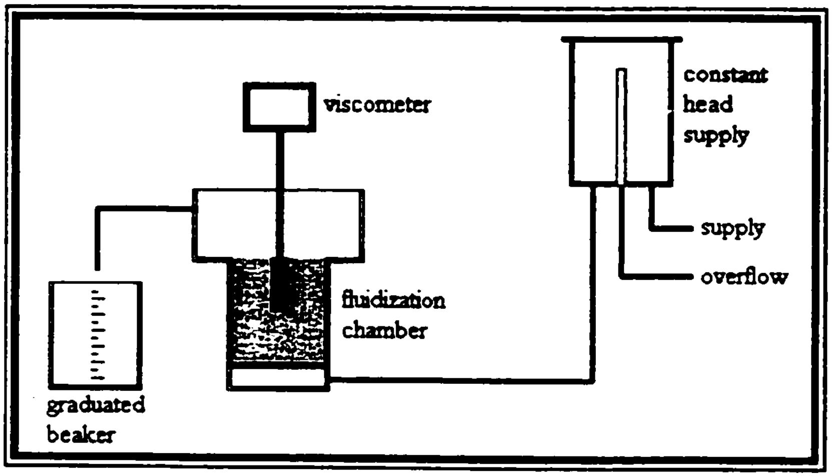

**Figure 3.4**: Schematic Diagram of Viscosity Measuring Device

The operation of the device is simple. A reservoir, filled with ordinary tap water, and having constant head is piped to the inlet of the fluidization chamber, measuring 100mm in diameter and 100mm in height. The water is introduced through two inlet pipes and a porous stone is used to disperse the flow uniformly across the cross section of the fluidized bed. The chamber contains a known mass of Barnes sand, the fluidized granular material. Knowing of the volume of the vessel (and accounting for the presence of the viscometer rotor), the mass of the sand and assuming homogenous fluidization, the porosity of the bed can calculated to a high degree of accuracy. The fluidization chamber is topped by an expansion chamber which slows the flow of water and prevents the flow of sand above the desired height of the fluidized region.

The outlet flow of water is directed to a graduated container allowing the flow rate to be accurately measured. The height of the constant head reservoir may be adjusted to accommodate a range of bed porosities. Direct reading piezometers were used to determine the pressure drop across the fluidized bed.

As previously mentioned, the fluidized granular material was sand, specifically #40 Barnes sand. The sand was sieved to produce a material with a more homogenous particle size distribution. Three particle size distributions were analyzed. Two of these distributions where normal while the third is a bimodal mixture of equal proportions of the first two. Specifically, the particle size ranges are:

- 100% 75μm - 150μm (WS 75/150)
- 100% 150μm - 300μm (WS 150/300)
- 50% 75μm - 150μm + 50% 150μm - 300μm (WS 75/150+150/300)

A photograph of the sand taken under a microscope showing the particle shape is given in Figure 3.5.

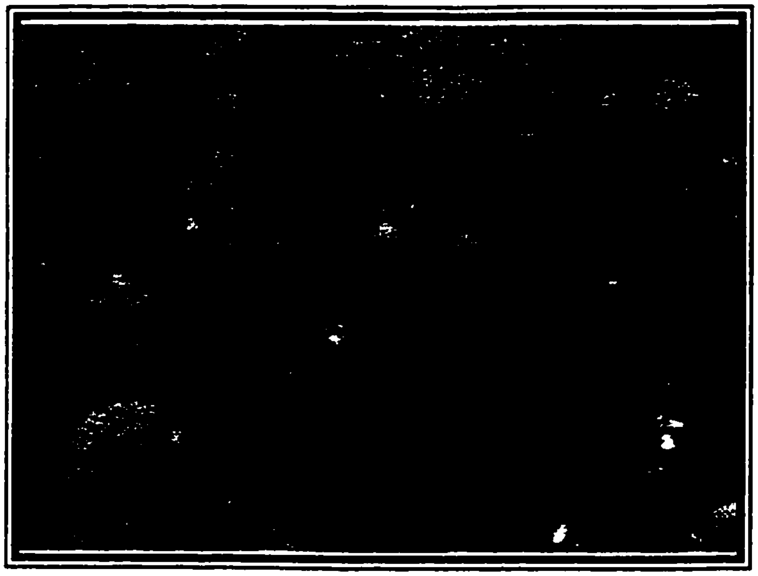

**Figure 3.5**: Photograph of Barnes Sand

The viscometer is a rotating cylinder, immersed in the fluidized mixture. The torque (and hence shear stress) on the cylinder was measured, which in turn converted to the viscosity of the mixture. The resulting viscosity measurements for the grain size distributions considered are given in Figure 3.6. Figure 3.7, shows viscosity as a function of shear rate. It can be seen that above 50% solids concentration ($\varepsilon_s = 1\text{-n}$), the relative viscosity decreases strongly with shear rate and so the mixture may no longer be considered Newtonian.

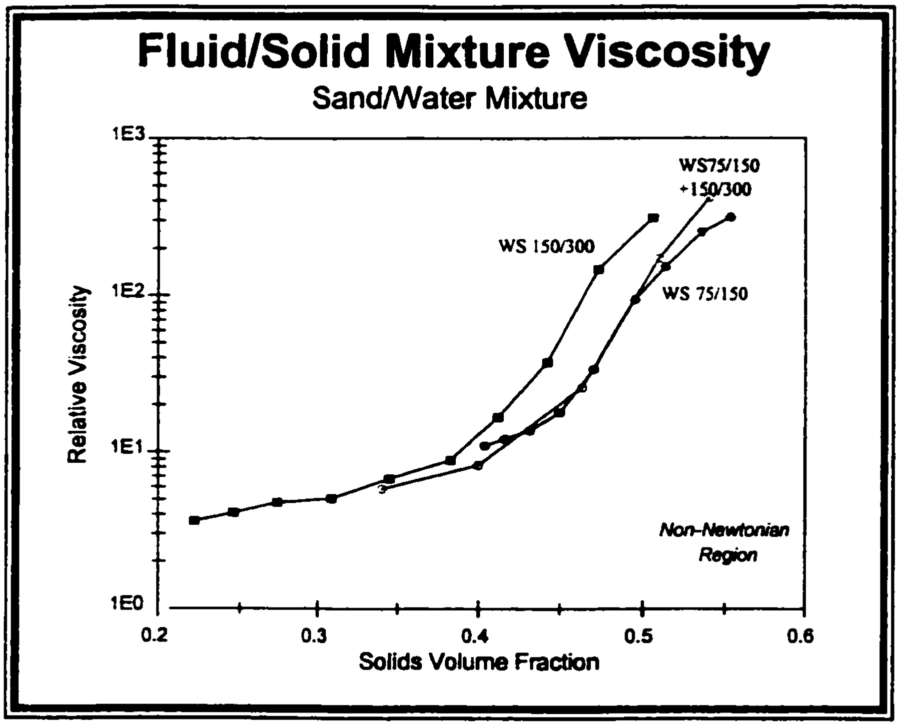

**Figure 3.6**: Viscosity Measurements using Brookfield Viscometer

It may be observed that viscosity depends weakly on shear rate below $\varepsilon_s$= 0.5. However, it rapidly becomes shear-rate dependent above this concentration. An examination of the curves in Figure 3.7 indicates that the material is shear thinning in the non-Newtonian region. Rutgers (1962) indicates that Newtonian behaviour of the mixture depends on "loose and random" contact between the granular particles to achieve momentum diffusion. At low porosity levels (0.5 in this case) this contact becomes more structured and the momentum no longer diffuses via the Newtonian description.

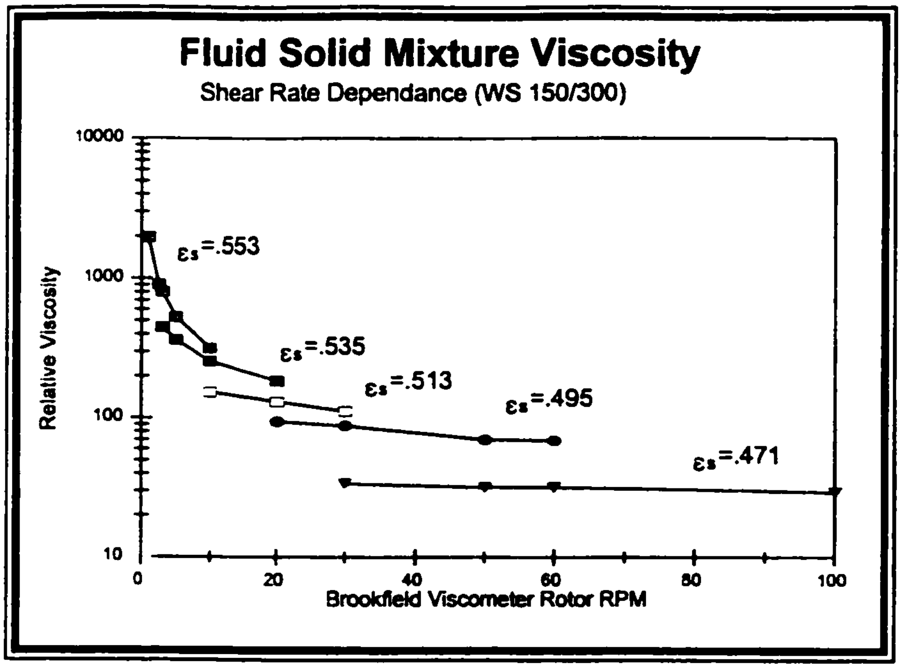

**Figure 3.7**: Dependance of Viscosity on Shear Rate

### 3.3.2 Comparison of Results to Previous Work

Given the very large variability of the mixture viscosities found in the literature, it is of particular importance that the current findings be compared to previous studies. As previously mentioned, Rutger provides viscosities for a wide range of mixtures **in suspension**, while Tsuchiya reports data from **fluidized** sands and glass beads. Figure 3.8 shows Rutger's "average curve" of the data as well as that reported by Tsuchiya. Superimposed on this figure is the data from the current research.

It can be seen that the results from this research lie within the region reported in the previous studies. The agreement of the data reported herein with that provided in the literature provides support

- that the measurements made for sand water systems are repeatable
- that the measurements are not specific to the apparatus used
- that correlations developed by other researchers are applicable

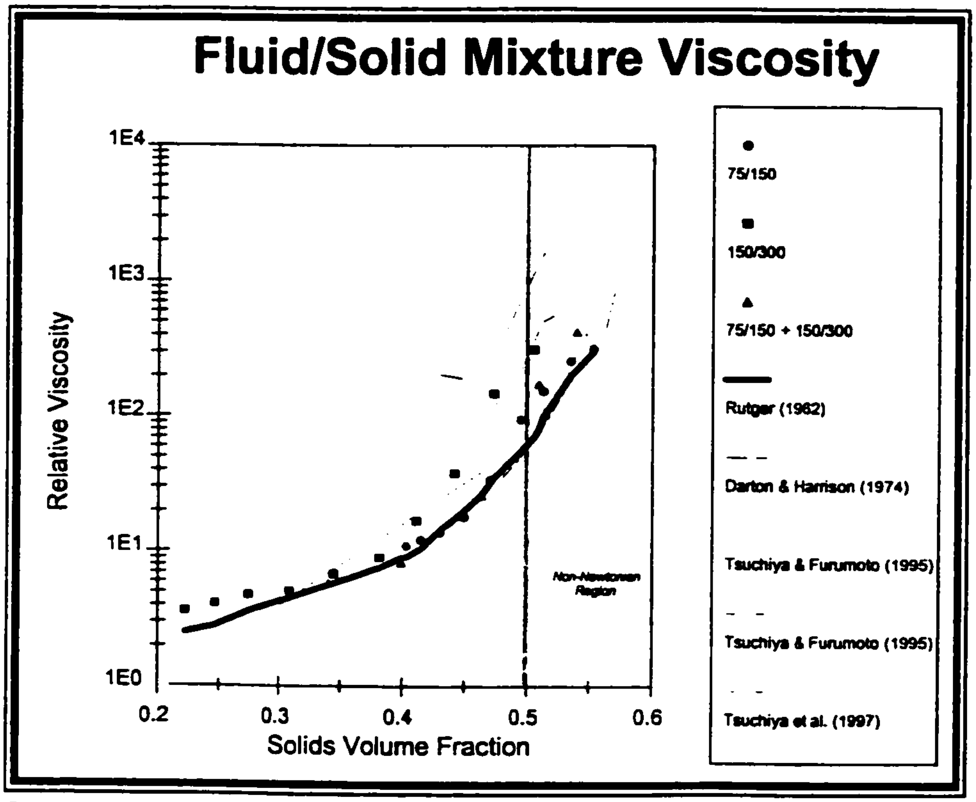

**Figure 3.8**: Comparison of Current Findings to Previous Research

A slightly modified form of Mooney's (1951) correlation is considered in this study. This has the form

$$\frac{\mu_m}{\mu_l} = \exp\left\{ \exp\left[ \frac{\varepsilon_s}{k_\mu^1 + k_\mu^2 \varepsilon_s} \right] \right\} \tag{3.36}$$

where $\varepsilon_s$ is the solids volume fraction ($\varepsilon_s = 1 - n$). This equation may be rearranged as

$$\frac{1}{\ln\left[\ln\left(\frac{\mu_m}{\mu_f}\right)\right]} = k_\mu^1\left(\frac{1}{\varepsilon_s}\right) + k_\mu^2 \qquad (3.37)$$

which is of a form suitable for determining the constants using the slope and vertical intercept of the plot of $1/\ln(\ln(\mu_m/\mu_f))$ versus $1/\varepsilon_s$, as shown in Figure 3.9.

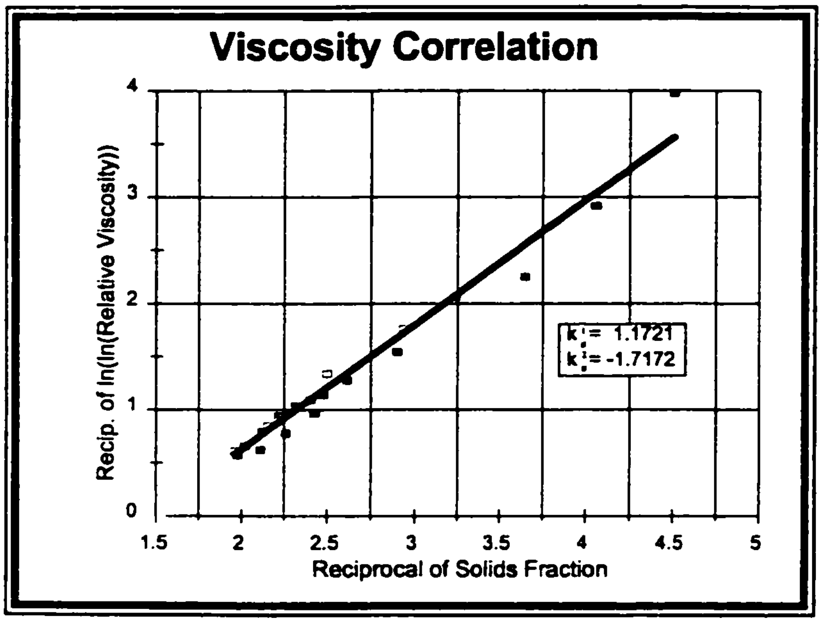

**Figure 3.9**: Linearized Viscosity Data

It is apparent, in Figure 3.6 that the various size distributions of sand give slightly different viscous behaviors. However, for the purpose of demonstrating the utility of the model, these differences are neglected and a single group of correlation constants is used for all sands. A linear regression analysis of the data plotted in Figure 3.9, yields the correlation constants:

$$k_\mu^1 = 1.1721$$

$$k_\mu^2 = -1.7172$$

The coefficient of determination ($R^2$) is 0.9724, indicating an exceptionally good fit of the data.

The above constants are strictly applicable only to the particular sand under consideration. If other materials are to be considered, new constants (or even new correlation equations) should be developed based on applicable experimental data.

### 3.3.3 Non-Newtonian Region

When a fluid/granular mixture becomes densely packed ($n < 0.5$), it's behavior changes from a viscous Newtonian fluid to the highly non-linear behavior shown in Figure 3.7. In this study, it is assumed that the material goes from a viscous fluid at $n < 0.5$, to a non-linear elastic solid that behaves as a more classical geo-material. With this assumption, a wide range of constitutive models becomes available for the stress/strain behavior. The reader should note that the usual elastic description is not strictly consistent with the Eulerian representation of the conservation equations used in this thesis. However, when the granular component is densely packed, the strains are very small such that:

$$\varepsilon_{ij}^{d} \approx \dot{\varepsilon}_{ij}^{d} \Delta t \tag{3.38}$$

Therefore, the Eulerian and Lagrangian equations appear similar, thus allowing us to move from one description to another (Malvern, 1969).

As was mentioned in the opening chapter, constitutive models are available for geo-materials with a wide range of complexity. It is important when selecting a model to consider the importance of the stress response of the material within the context of the overall behavior of the system. In the current research, the post-liquefaction response is of primary importance. Therefore, a simple stress/strain constitutive model is sufficient for the granular component prior to liquefaction, provided that a build-up of pore pressure due to shear induced volume changes can be accounted for.

### (i) Stress/Strain Constitutive Model

Hosni (1992) provides a simple, effective stress/strain constitutive model suitable for the needs of this study. The model is for a non-linear elastic material where the shear stresses ($\tau_{ij}$) are proportional to the deviatoric strains in the usual elastic manner:

$$\tau_{ij} = G\varepsilon_{ij}^{d} \tag{3.39}$$

with the shear modulus (G) being given by the simple engineering approximation:

$$G = \left(\frac{G}{G_0}\right) \cdot 220 \cdot K_{2_{max}} \cdot P_s^{\frac{1}{2}} \qquad (kPa) \tag{3.40}$$

where $(G/G_o)$ is a decreasing function with strain (as shown in figure 3.10).

$K_{2max}$ is a constant, ranging from 0.4 to 0.6 for sandy soils, that depends on the relative density. Finally, $P_s$ is, as previously defined, the pressure in the granular component.

The decreasing shear modulus with increasing shear strain can be readily seen when the stress/strain behavior of equation 3.40 is plotted in Figure 3.11 for a range of confining pressures in the granular material.

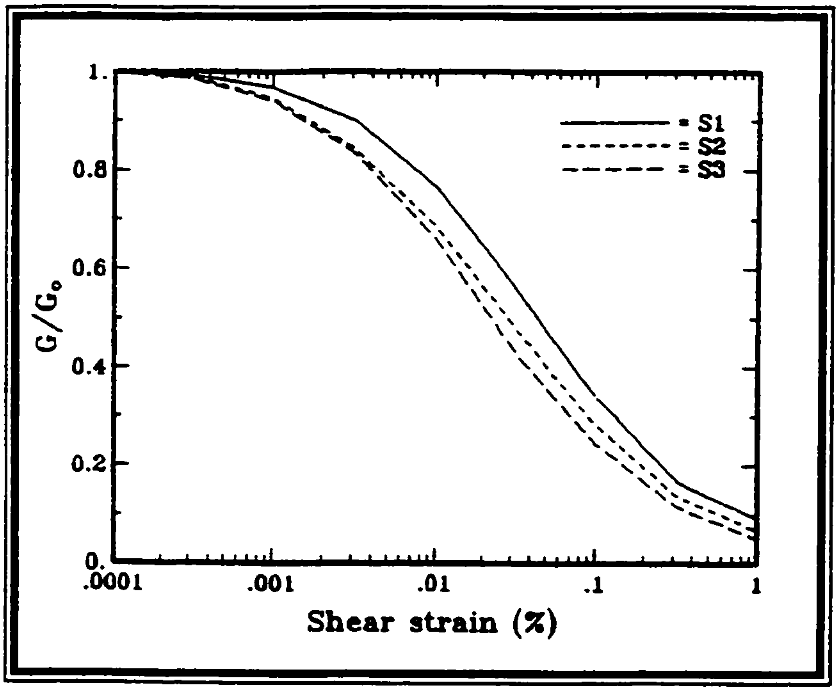

**Figure 3.10**: Effect of Shear Strain on Shear Modulus

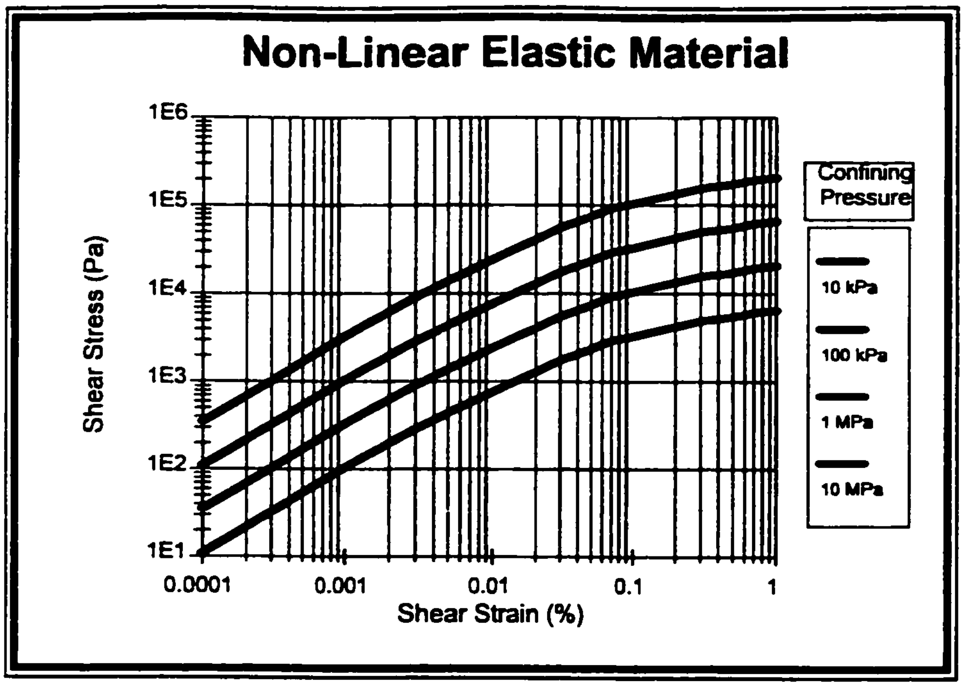

**Figure 3.11**: Stress/Strain Behavior

### (ii) Confining Pressure in The Granular Component

A key objective of this study is the analysis of post-liquefaction in sandy soils. As outlined in the introductory chapter, liquefaction is triggered by the soil skeleton tendency to compact under the action of shear strains. This compaction is prevented by the presence of the pore fluid. The pore fluid is "squeezed" by the grains attempting to compact, which, in turn, increases the pressure of the fluid and begins to transfer the spherical stress from the granular component to the fluid. At a critical point, the spherical stress (confining pressure) in the granular material is reduced to zero (or close to zero). It is well known that a granular material relies on confining pressure to provide shear resistance. In a non-cohesive material such as a sandy soil, when the confining pressure is reduced to zero, the shear strength also vanishes. (This behavior is reflected in the stress/strain constitutive model of equations 3.39 and 3.40)

Owing to the strong dependance of the shear strength on the tendency of the granular material to compact, it is vital that an accurate model of this behavior be included in the hydrodynamic model. Unfortunately, many of the traditional constitutive models employed in soil mechanics for this purpose are highly complex and computationally unwieldy. Thus, a simple constitutive model has been developed using the more traditional concepts of soil mechanics. The following derivation is original.

An accepted notion in soil mechanics is that changes in confining pressure are accompanied by volumetric strain (Malvern, 1969). A standard expression for this behavior is

$$-\frac{d\varepsilon_v}{dP_s} = \frac{A}{P_s} \tag{3.41}$$

where $\varepsilon_v$ is the volumetric strain and A is a proportionality constant. The volumetric strain can be re-written as

$$d\varepsilon_v = \frac{de}{1+\bar{e}} \tag{3.42}$$

where e is the void ratio and $\bar{e}$ is the void ratio at the beginning of a strain increment. The void ratio may be expressed in terms of porosity

$$e = \frac{n}{1-n} \tag{3.43}$$

Taking the derivative of eq. 3.43 with respect to porosity yields

$$\frac{de}{dn} = \frac{1}{(1-n)^2} \tag{3.44}$$

or

$$de = \frac{dn}{(1-n)^2} \tag{3.45}$$

Let

$$\bar{e} = \frac{\bar{n}}{1-\bar{n}} \tag{3.46}$$

Condensing equations 3.42 through 3.46 allows one to write

$$d\varepsilon_v = dn\frac{1-\bar{n}}{(1-n)^2} \tag{3.47}$$

Substituting equation 3.47 into equation 3.41 yields

$$\frac{dP_s}{dn} = -\frac{P_s}{A}\frac{1-\bar{n}}{(1-n)^2} \tag{3.48}$$

Re-arranging equation 3.48 and integrating both sides provides

$$\int\frac{1}{P_s}\,dP_s = -\frac{1-\bar{n}}{A}\int\frac{1}{(1-n)^2}\,dn + C \tag{3.49}$$

which after performing the integration gives

$$\ln P_s = -\frac{1-\bar{n}}{A}\frac{1}{1-n} + C \tag{3.50}$$

or

$$P_s = \exp\left[ -\frac{1}{A}\frac{1-\bar{n}}{1-n} + C \right] \qquad \textbf{(3.51)}$$

with C being an integration constant.

At this point, it is insightful to interpret the meaning of equation 3.51. This equation shows that, in this model, the confining pressure is essentially an exponential function of the ratio between porosity, n, and a reference porosity, $\bar{n}$. As n becomes less than $\bar{n}$, this ratio becomes greater than unity and the confining pressure increases rapidly due to the exponential nature of equation 3.51. In evaluating the constant, C, the conditions at the reference porosity must be considered. It is convenient to define this reference porosity as the level at which the confining pressure has some very low value. If $P_s$ is set to unity when $n = \bar{n}$, a simple expression results

$$1 = \exp\left[ -\frac{1}{A} + C \right] \qquad \textbf{(3.52)}$$

and therefore,

$$C = \frac{1}{A} \qquad \textbf{(3.53)}$$

Substitution of equation 3.53 into 3.51 yields

$$P_s = \exp\left[ \frac{1}{A}\left( 1 - \frac{1-\bar{n}}{1-n} \right) \right] \qquad \textbf{(3.54)}$$

The confining pressure at any porosity is thus a function of two variables; a flexibility term A and a reference porosity $\bar{n}$. Equation 3.54 indicates that decreasing A results in increasing confining pressure. The effect of this constant can be seen in Figure 3.12 (with $\bar{n} = 0.5$).

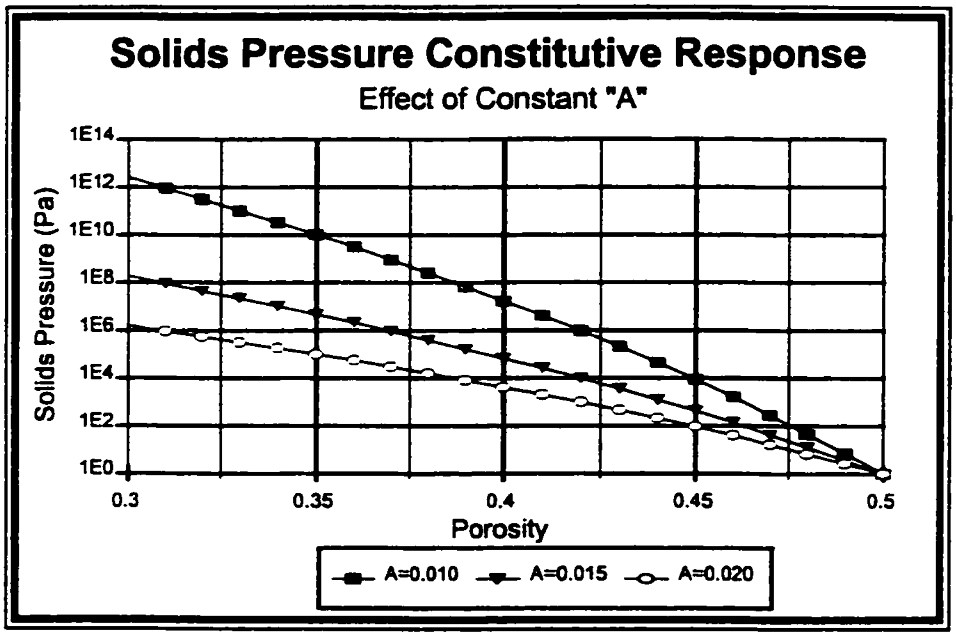

**Figure 3.12**: Effect of Flexibility Constant (A)

A well known characteristic of granular materials is that the same grains may exist at different porosities at exactly the same confining pressure. The reference porosity, $\bar{n}$, in equation 3.54 provides a vehicle to capture this behavior. $\bar{n}$ in essence "offsets" the response of the soil. This effect can be seen in Figure 3.13 (with A = 0.015). The reference porosity thus provides a powerful indicator of the state of the granular material, which is similar to the use of void ratio as an indication of state in critical state mechanics (Castro, 1969, 1975).

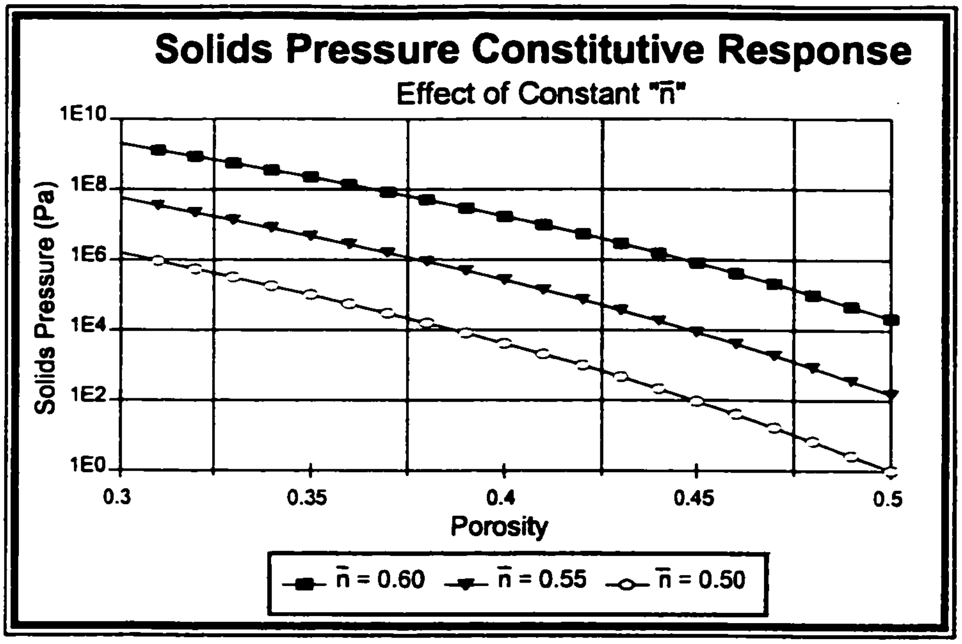

Figure 3.13: Effect of Reference Porosity (n̄)

As indicated previously, the behavior of the granular material is tied to the fluid occupying the void space. There are two extreme cases of granular/fluid behavior often referred to in soil mechanics as drained and undrained response. In the first case, the permeability of the granular material is very high (as compared to the rate of loading) such that the pore fluid is instantaneously squeezed out of the voids spaces when the granular material experiences changes in volume. As such, there is no increase of pressure in the fluid and the granular material supports any new loads without delay. In the undrained case, the permeability of the soil is reduced to zero, such that the fluid cannot escape the void spaces. Hence any new loads cause a squeezing of the incompressible fluid rather than straining the granular material and loads are transferred to the fluid rather than to the solid. In the extreme event of liquefaction, the confining pressure in the granular material is reduced to zero.

The use of equation 3.54 in the context of the overall hydrodynamic equations provides a vehicle for capturing both of these extreme cases, as well as intermediate situations. In simple terms, the tendency towards volume change is reflected by changes to the reference porosity. The basic hydrodynamic equations control the rate at which the actual porosity may change by controlling the flow of the fluid in the void space. Graphically, this is shown in Figure 3.14. In the drained case, the tendency to compact (say due to a shear strain) is reflected by a change in the reference porosity from $\bar{n}_0$ to $\bar{n}_1$. Since the fluid is free to flow uninhibited, the porosity changes such that the (effective) confining pressure, $P_s$, remains constant. In the undrained case, again the tendency to compact is reflected by a "desired" change in $\bar{n}$. This time however, the porosity cannot change. Eq. 3.54 predicts a reduction in confining pressure which, to maintain static equilibrium, must be transferred to the fluid. This is consistent with experimental results. In a real scenario, there is no such thing as undrained conditions. Eventually, over time, the fluid escapes allowing the porosity to change. This is referred to as consolidation, shown graphically in Figure 3.14. Again, the hydrodynamic equations combined with eq. 3.54 will predict this response.

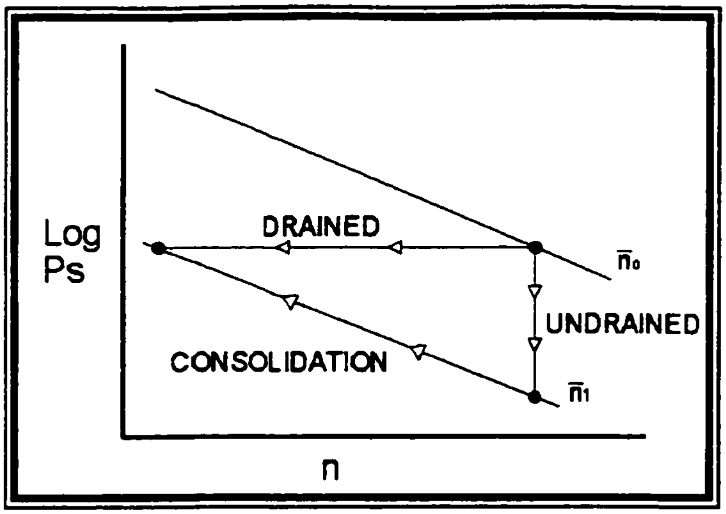

**Figure 3.14**: Densification Behavior

A final issue remains. Changes in $\bar{n}$ due to shear strains must accurately model the behavior of the granular component. The following section describes the methodology used in this study.

(iii) Modeling Changes in the Reference Porosity

Relations quantifying changes in the reference porosity must accurately reflect the behavior of the granular component. A model to quantify this change could take on the form of traditional complex constitutive models found in soil mechanics. Again the problem of computational efficiency surfaces.

Recently however, artificial neural networks (ANN's) have appeared in the soil mechanics literature for the purpose of modeling a wide range of soil behavior. Owing to the ability of neural networks to model complex, non-linear behavior, such a method could be useful for predicting changes in $\bar{n}$ due to straining. A thorough description of the principals behind ANN's is beyond the scope of this thesis. However, there are several introductory texts on the subject, which can provide a deeper understanding. (Rocha, 1992, Nelson, 1991, Khanna, 1990). In brief, the ANN is comprised of a series of simultaneous, non-linear equations. These equations contain several multipliers and constants which are determined via an optimization procedure to minimize the error between predicted and actual outputs from the network for a given series of input combinations.

In this study, a commercial neural network software package known as EasyNN (Wolstenholme, 1999) was employed to determine the multipliers (weights) and constants (biases). The values determined by the neural network model were implemented in the finite element code for solving various case studies. To train the network, data is required for the behavior of a granular material. Fortunately, the VELACS (1997) (VErification of Liquefaction Analysis by Centrifuge Studies) program has made tabulated data for undrained, cyclic, triaxial tests on sandy soils available. This data was input into the neural network software and the weights and biases where recorded. The structure of the neural network is displayed in Figure 3.15. The solids pressure model provides changes in the reference porosity as a function of shear strains.

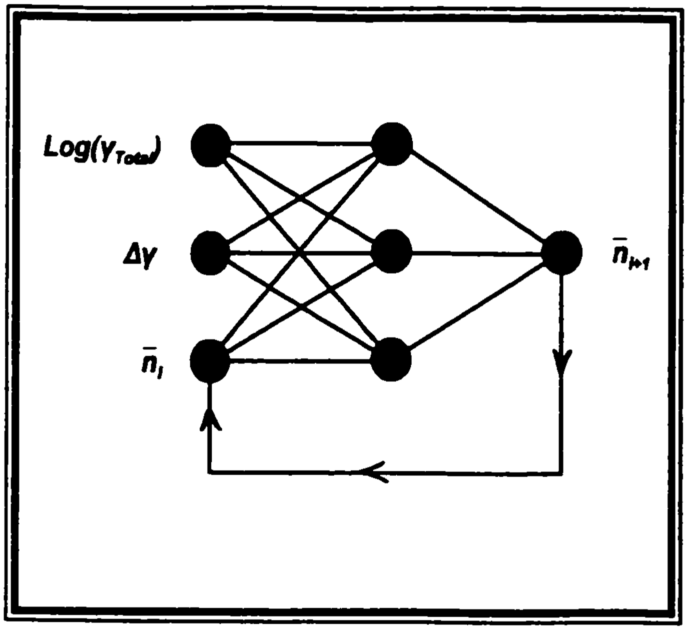

**Figure 3.15**: Neural Network Structure

Figure 3.16 shows plots of three training data histories, along with a test case showing both the measured and ANN predicted n̄ values for triaxial tests. It can be seen that there is good agreement between the measured and predicted response. The reader is referred to Appendix 3.1 for details on the implementation of an artificial neural network in a finite element code.

## 3.4 Summary

In the second chapter, a series of basic hydrodynamic equations were presented to model the flow of two-component mixtures of granular solids in a fluid. The fundamental unknowns in these equations are the mixture pseudo velocity (**V**), the difference pseudo velocity (**W**), the fluid pressure ($P_f$) and the porosity (n). Unfortunately, several terms in the equations contained other variables as well. To be able to solve the

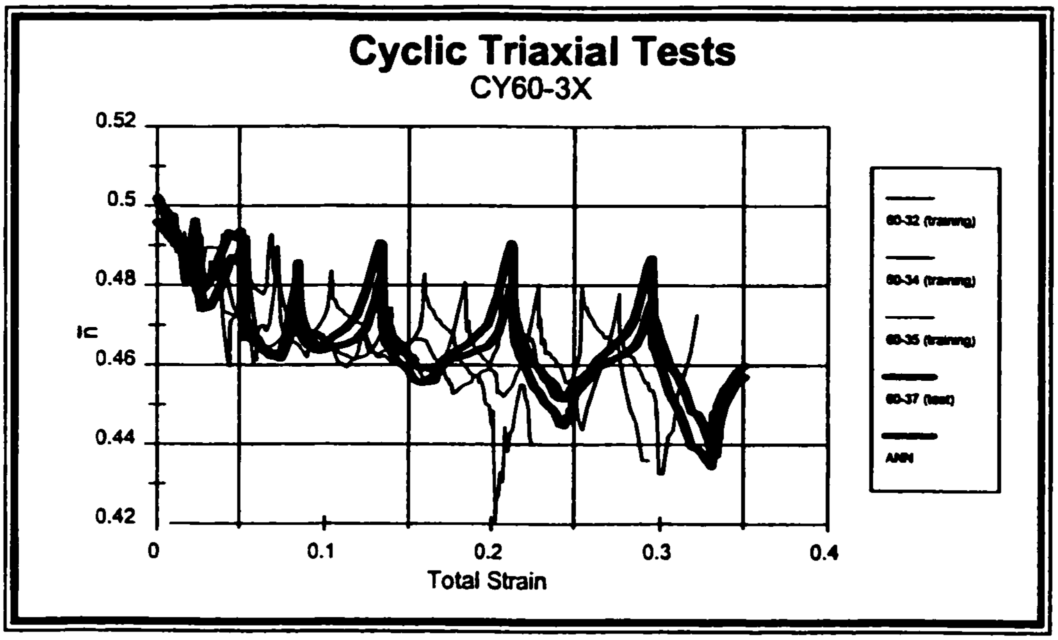

**Figure 3.16**: Results of ANN Training

hydrodynamic equations, another set of equations referred to as closure equations had to be developed so that only the fundamental unknowns remained. These closure equations were the subject of this chapter.

The three areas requiring closure equations, which were developed in the preceding sections, are:

- hydrodynamic drag between the two components
- granular component shear stress
- granular component pressure

# APPENDIX 3.1 IMPLEMENTING AN ARTIFICIAL NEURAL NETWORK IN A NON-LINEAR ELASTIC ANALYSIS CODE

An artificial neural network (ANN) is used in this study to update the reference porosity as described in section 3.3.3. Neural network may be expressed in terms of a series of simple matrix operations.

In this study, the inputs to the ANN are (refer to figure 3.15):

- Change in deviatoric strain, $\Delta\gamma$
- Log of the total deviatoric strain, Log($\gamma$)
- Current reference porosity, $\bar{n}_{t-\Delta t}$

The output is the new reference porosity $\bar{n}_t$.

In practice, the neural network code is organized as a subroutine. The inputs from the main program are passed to the subroutine and the output is passed from the subroutine back to the main program.

The first step in the ANN code is to normalize the inputs ($x_i$) between minimum and maximum values of 0 and 1 respectively. This is performed by the following operation:

$$\bar{x}_i = \frac{x_i - x_{i_{min}}}{x_{i_{max}} - x_{i_{min}}}$$

where $\bar{x}_i$ are the normalized inputs and $x_{imin}$ and $x_{imax}$ are the minimum and maximum values of the $i^{th}$ input, respectively.

The normalized inputs are then multiplied by the first hidden layer weights ($W^h_{ij}$) and a vector of biases ($b^h_j$) are added. This may be expressed as:

$$v_j = \bar{x}_i W_{ij}^h + b_j^h$$

where $v_j$ are the initial hidden layer values. Note that repeated indices imply summation. At this point, the initial hidden layer values are processed by a non-linear function. In this study, the function is of the following form:

$$V_j = \frac{1}{1 + e^{-v_j}}$$

where $V_j$ are the hidden layer outputs (having values between 0 and 1) (*e* here is the exponential function not the void ratio). If there is more than one hidden layer, these values would go through a similar procedure for each hidden layer. In this study, there is only one hidden layer. The output from the hidden layer is passed to the output layer. First, these hidden layer outputs are multiplied by the output layer weights ($W^o_{jk}$) and another vector of biases ($b^o_k$) is added:

$$y_k = V_j W_{jk}^o + b_k^o$$

where $y_k$ are the initial output values.

The initial output values are themselves processed by the same function as the initial hidden layer outputs:

$$\bar{Y}_k = \frac{1}{1 + e^{-y_k}}$$

where $Y_k$ are the normalized output values. The following converts the normalized values to the actual output values ($Y_k$):

$$Y_k = \bar{Y}_k\left(Y_{\max} - Y_{\min}\right) + Y_{\min}$$

where $Y_{kmax}$ and $Y_{kmin}$ are the maximum and minimum output values, respectively, of the kth output. These output values (which in this study is a single value, $\bar{n}_t$) are returned to the main program.

For details on Artificial Neural Networks, the reader is referred to Rocha (1992), Nelson (1991) and Khanna (1990).

The neural network used in this study consists of three input values (log of total shear strain, shear strain increment and the current value of $\bar{n}$ in that order). There are three hidden nodes and one output node (giving the new value of $\bar{n}$). The hidden layer weights ($W^h_{ij}$) are:

| | | |
|---|---|---|
| -1.159932 | -2.163154 | 8.074500 |
| -1.153477 | -2.234670 | 7.259948 |
| 1.555892 | -5.063079 | 8.430298 |

and the hidden layer biases ($b^h_j$) are:

| | | |
|---|---|---|
| -6.2368 | -5.4514 | 0.6681 |

The output layer weights ($W^o_{jk}$) are:

```
3.256640   2.570816   2.172821
```

and the output layer bias ($b^o_k$) is:

```
1.8695
```

## NOMENCLATURE

| | |
|---|---|
| $A$ | Solids pressure compressibility |
| $b^h$ | Hidden layer bias |
| $b^o$ | Output layer bias |
| $k_1$, $k_2$ | Correlation constants |
| $k^1_u$, $k^2_u$ | Correlation constants for mixture viscosity |
| $K_{2max}$ | Correlation constant for shear modulus of sand |
| $C$ | Integration constant |
| $C_D$ | Drag coefficient on a single particle |
| $C_D$ | Drag coefficient on a single particle in a granular/fluid mixture of similar particles |
| $d_p$ | Diameter of particle |
| $e$ | Void ratio |
| $f(n)$ | Function of porosity |
| $f'(n)$ | Modified function of porosity |
| $F_b$ | Buoyant force |
| $F_D$ | Force on particle due to drag |
| $F_D$ | Drag force on a single particle in a granular/fluid mixture of similar particles |
| $g$ | Gravitational acceleration |
| $G$ | Shear modulus |
| $L$ | Dimensionless length |
| $\mathbf{M}_D$ | Momentum flux due to hydrodynamic drag |
| $P$ | Pressure |
| $R_e$ | Reynolds number |
| $v$ | Initial hidden layer output |
| $V$ | Final hidden layer output |
| $\mathbf{V}$ | Mixture pseudo-velocity |
| $V_r$, $\mathbf{V}_r$ | Relative velocity |
| $U$, $\mathbf{U}$ | Velocity |
| $W^h$ | Hidden layer weights |

| | |
|---|---|
| $W^o$ | Output layer weights |
| $\mathbf{W}$ | Difference pseudo-velocity |
| $W_p$ | Net weight of a particle |
| $W'_p$ | Modified net weight of a particle |
| $x$ | Neural network input |
| $y$ | Initial output layer output |
| $Y$ | Final output layer output |

## Greek Symbols

| | |
|---|---|
| $\beta$ | Interfacial drag |
| $\varepsilon^d$ | Deviatoric strain |
| $\varepsilon_s$ | Volume ratio of granular particles |
| $\varepsilon_v$ | Volumetric strain |
| $\gamma$ | Shear strain |
| $\mu$ | Viscosity |
| $\rho$ | Density |
| $\tau$ | Shear stress |

## Subscripts

| | |
|---|---|
| f | Fluid component |
| l | Liquid |
| m | Mixture |
| s | Granular component |

## Superscripts

| | |
|---|---|
| - | Reference quantity |
| - | Normalized quantity (ANN) |

## REFERENCES

Bird, R.B., Stewart, W.E., Lightfoot, E.N.
***Transport Phenomenon***
John Wiley & Sons, New York, 1960

Carmen, P.C.
***Fluid Flow Through Granular Beds***
Trans. Inst. Chem. Engrs., Vol. 14, pp. 150-166, 1937

Castro, G.
***Liquefaction and Cyclic Mobility of Saturated Sands***
J. Geotech. Eng. Div., Vol. 101, pp. 551-569, 1975

Cheremisinoff, N.P.
***Hydrodynamics of Gas-Solids Fluidization***
Gulf Publishing, Houston, 1984

Clift, R., Seville, J.P.K., Moore, S.C, Chavarie, C.
***Comments on Buoyancy in Fluidized Beds***
Chem. Eng. Sci., Vol. 42, pp. 191-194, 1987

Darton, R.C.
***The Physical Behaviour of Three-Phase Fluidised Beds***
in Fluidization, 2nd Ed., Davidson, Clift, Harrison, Academic Press, London, 1985

Darton, R.C., Harrison, D.
***The Rise of Single Gas Bubbles in Liquid Fluidised Beds***
Trans. Instn. Chem. Engrs., Vol. 52, 1974, p. 301-306

Ergun, S.
***Fluid Flow Through Packed Columns***
Chem. Eng. Prog., Vol. 48, pp. 89-94, 1952

Gibilaro, L.G., Foscolo, P.U.
***A Fully Predictive Criterion for the Transition Between Particulate and Aggregate Fluidization***
Chem. Eng. Sci., Vol. 39, pp.1667-1675, 1984

Gibilaro, L.G., di Felice, R., Waldram, S.P.
***Authors' Reply to Comments by Clift et al.***
Chem. Eng. Sci., Vol. 42, pp.194-196, 1987

Gidaspow, D.
***Hydrodynamics of Fluidization and Heat Transfer: Supercomputer Modeling***
Appl. Mech. Rev., Vol. 39, pp. 1-23, 1986

Gidaspow, D.
***Multiphase Flow and Fluidization: Continuum and Kinetic Theory Descriptions***
Academic Press, Boston, 1994

Henriksen, H.K., Østergaard, K.
***Characteristics of Large Two-Dimensional Air Bubbles in Liquids and in Three-Phase Fluidised Beds***
Chem. Eng. J., Vol. 7, pp.141-146, 1974

Hosni, S.
***A Study of the Implications of Soil-Structure Interaction Effects on the Seismic Response of High-Rise Reinforced Concrete Buildings***
Ph.D. Thesis, McMaster University, 1992

Jeffrey, D.J., Acrivos, A.
***The Rheological Properties of Suspensions of Rigid Particles***
A.I.Ch.E.J., Vol. 22, pp. 417-432, 1976

Kahn, A.R., Richardson, J.F.
Chem. Eng. Commun., Vol. 62, pp. 135-?, 1987

Kahn, A.R., Richardson, J.F.
***Pressure Gradient and Friction Factor for Sedimentation and Fluidisation of Uniform Spheres in Liquids***
Chem. Eng. Sci., Vol. 45, pp. 255-265, 1990

Khanna, T.
***Foundations of Neural Networks***
Addison-Wesley, Reading, MA, 1990

Malvern, L.E.
***Introduction to the Mechanics of a Continuous Medium***
Prentice Hall, New Jersey, 1969

Mooney, M.
***The Viscosity of a Concentrated Suspension of Spherical Particles***
J. Colloid Sci., Vol. 6, p. 162-170

Nelson, M.
***A Practical Guide to Neural Nets***
Addison-Wesley, Reading MA, 1991

Richardson, J.F., Zaki, W.N.
***Sedimentation and Fluidisation: Part I***
Trans. Inst. Chem. Engrs., Vol. 62, pp. 35-53, 1954

Rocha, A.F.
***Neural Nets: A Theory for Brains and Machines***
Springer-Verlag, Berlin, 1992

Rowe, P.N.
***Drag Forces in a Hydraulic Model of a Fluidized Bed, Part II***
Trans. Inst. Chem. Engrs., Vol. 39, pp. 175-180, 1961

Rutgers, Ir., R.
***Relative Viscosity of Suspensions of Rigid Spheres in Newtonian Liquids***
Rheologica Acta, Vol. 2, 1962, p. 202-210

Savage, S.B., McKeown, S.
***Shear Stresses Developed During Rapid Shear of Concentrated Suspensions of Large Spherical Particles Between Concentric Cylinders***
J. Fluid. Mech., Vol. 127, pp. 453-472, 1983

Schürgerl, K., Merz, M., Fetting, F.
***Rheologische Eigenshaften von Gasdurchströmten Fliessbettsystemen***
Chem. Eng. Sci., Vol. 15, pp. 1-38, 1961

Tsuchiya, K., Furumoto, A., Fan, L.S., Zhang, J.
***Suspension Viscosity and Bubble Rise Velocity in Liquid-Solid Fluidized Beds***
Chem. Eng. Sci., Vol. 52, pp. 3053-3066, 1997

VELACS Cyclic Triaxial Data
Obtained from VELACS website (http://rccg03.usc.edu/velacs/)

Wolstenholme, S.
***EasyNN, Neural Network Software***
Version 3.2, 1999

# 4 FINITE ELEMENT MODELING

In the second chapter, a series of partial differential equations were presented that describe the flow behavior of a two-component mixture of soil and fluid. This chapter presents these equations in their integral form and then in a discretized form via the finite element method. As is usual with the finite element method, the discretization process allows the unknown quantities to be determined at discrete locations within the domain.

Similar to the presentation of Chapter 2, single component flow equations are presented first followed by their extension to two-component mixtures. This allows the finite element concepts to be more clearly understood without the complication of the large number of terms that are present in the two component systems.

## 4.1 Principle of Virtual Work (Malvern, 1969)

The principle of virtual work, which is closely related to Galerkin procedures, provides a basis for the development of the integral form of equations from the continuous partial differential equations. This in turn allows the unknown quantities to be determined at a finite number of locations within the domain, via the finite element discretization.

This principle is in essence, a statement that the internal work done on a body must be equal to the external work applied. For example, consider a body having a stress field (**σ**), and both internal body forces (**b**) and external forces (**t**) applied on the surface (**Γ**). If the body is moved through arbitrary displacements (δ**u**) and stretched by corresponding strains (δε = S**δu**, where S is a linear operator defining strains in terms of displacements), the internal and external virtual work in the domain, Ω must be equal,

$$\int_{\Omega} \delta\varepsilon^{T}\boldsymbol{\sigma}\, d\Omega - \int_{\Omega} \delta \boldsymbol{U}^{T}\boldsymbol{b}\, d\Omega = \int_{\Gamma} \delta \boldsymbol{U}^{T}\boldsymbol{t}\, d\Gamma \qquad (4.1)$$

The reader should note that the analogy in fluid dynamics is the application of an arbitrary velocity field rather than a displacement field. In this case, it is the **rate** of internal work done on the body that must equal the **rate** of external work applied to the body.

## 4.2 Finite Element Equations for Single Component Flows

Single component fluids are considered first, to simplify the introduction of the finite element equations. Following this, the extension to two-component flows is presented. Since extensive literature exists on the finite element methodology ( Zienkiewicz and Taylor, 1989, Bathe, 1996, Oden, 1976), only the important points with regard to the solution of the equations in this study are considered here.

### 4.2.1 Continuity Equation

Recall from the second chapter that the continuity equation for a single component incompressible flow is

$$\nabla \cdot \boldsymbol{U} = 0 \tag{4.2}$$

The integrated equivalent for the continuity equation is obtained by multiplying equation 4.2 by the virtual pressure $\delta P$. After integrating over the domain, we have

$$\int_{\Omega} \delta P [\nabla \cdot \boldsymbol{U}] \, d\Omega = 0 \tag{4.3}$$

At this point a fundamental concept in finite element analysis is introduced, that of the discretization of an unknown. In the finite element method, the domain is divided into smaller volumes referred to as elements. The unknown field (velocity, pressure and porosity in this work) within each element is defined in terms of interpolation functions and unknowns at a finite number of special locations, referred to as nodes. These functions are also appropriately termed, shape functions (**N**) and depend only on position within the element. Any quantity of interest, $\psi$ for example, may be determined at a point within the element via

$$\psi \approx N \bar{\psi} \tag{4.4}$$

where $\bar{\psi}$ are the values of $\psi$ at the nodes. Although there are an infinite variety of shape function forms that may be envisaged, except for special circumstances, these are usually of polynomial form. More information on shape functions and the finite element method in general can be found in Zienkiewicz and Taylor (1989).

Using the finite element method, one can approximate the exact unknown field by the shape functions and a select number of nodal unknowns. In the case of the continuity equation, equation 4.3 becomes

$$\sum_{i=1}^{num.\ elements} \left( \int_{\Omega_{element}} \delta \bar{\boldsymbol{P}}^{T} \boldsymbol{N}_{P}^{T} \left[ \nabla \cdot \boldsymbol{N}_{U} \bar{\boldsymbol{U}} \right] \, d\Omega_{element} \right) = 0 \tag{4.5}$$

i.e., the integration over the domain is replaced by the summation of the integrations over the elements. Note that for clarity, the remaining integrations will be assumed to be over an element with the summation implied unless noted otherwise. According to the convention followed here, the subscript indicates to which variable the interpolation belongs.

The nodal quantities are independent of position within the element and can therefore be removed from the integrand. Therefore, equation 4.5 becomes

$$\delta \bar{\boldsymbol{P}}^{T} \left( \int_{\Omega} \boldsymbol{N}_{P}^{T} \left[ \nabla \cdot \boldsymbol{N}_{U} \right] \, d\Omega \right) \bar{\boldsymbol{U}} = 0 \tag{4.6}$$

Since δP is arbitrary, the term inside the brackets must vanish, yielding

$$\left( \int_{\Omega} \boldsymbol{N}_{P}^{T} \left[ \nabla \cdot \boldsymbol{N}_{U} \right] \, d\Omega \right) \bar{\boldsymbol{U}} = \boldsymbol{0} \tag{4.7}$$

Equation 4.7 is the finite element integrated equivalent of equation 4.2. The integral in brackets is the contribution of the continuity equation to the overall system matrix, which contains $\bar{U}$, the nodal velocity unknowns. This equation is combined with the conservation of momentum equation, which is presented in the next section, to form the overall system matrix.

### 4.2.2 Conservation of Momentum Equation

Again, from Chapter 2, recall the conservation of momentum equation for a single component incompressible fluid

$$\rho\frac{\partial \boldsymbol{U}}{\partial t} + \nabla P - \nabla\cdot(\boldsymbol{\tau} - \rho \boldsymbol{U}\boldsymbol{U}) + \rho \boldsymbol{F} = \boldsymbol{0} \tag{4.8}$$

Similar to the continuity equation, the integrated equivalent of equation 4.8 is

$$\int_{\Omega}\delta U\left(\rho\frac{\partial \boldsymbol{U}}{\partial t} + \nabla P - \nabla\cdot(\boldsymbol{\tau} - \rho \boldsymbol{U}\boldsymbol{U}) + \rho \boldsymbol{F}\right)d\Omega = \boldsymbol{0} \tag{4.9}$$

Following the usual practice to reduce the inter-element continuity requirements and maintain symmetry in the system matrix, the shear stress and pressure terms are integrated by parts; i.e.,

$$\int_{\Omega}\delta U(\nabla P - \nabla\cdot\tau)d\Omega = \int_{\Gamma}\delta U(P - \tau)d\Gamma - \int_{\Omega}\nabla\cdot\delta U(P - \tau)d\Omega \tag{4.10}$$

where $\Gamma$ is the bounding surface of $\Omega$. It should be noted that pressure is added to only the normal stress terms. Also, the gradient $\nabla\cdot\delta\mathbf{U}$ can be replaced by $\delta\dot{\varepsilon}$ due to the symmetry associated with the stress tensor.

Now, Zienkiewicz and Taylor (1989) show that for functions containing derivatives of the n$^{th}$ order, the finite element representation of that function must be continuous to the n$^{th-1}$ order. Therefore, equation 4.10 accomplishes two things. First, it reduces the maximum order of derivatives of **U** from second to first order. Secondly, it provides a vehicle for applying boundary tractions via the boundary term. For clarity at this point however, it will be assumed that either the velocity is prescribed along the boundary (i.e., $\delta\mathbf{U} = 0$) or that the boundary is traction free. In either case, the boundary term vanishes. Substituting equation 4.10 into equation 4.8 yields

$$\int_{\Omega} \delta \boldsymbol{U} \left( \rho \frac{\partial \boldsymbol{U}}{\partial t} + \nabla \cdot \rho \boldsymbol{U}\boldsymbol{U} + \rho \boldsymbol{F} \right) d\Omega + \int_{\Omega} \nabla \cdot \delta \boldsymbol{U} ( -\boldsymbol{P} + \boldsymbol{\tau} ) d\Omega = 0 \tag{4.11}$$

applying a finite element discretization and recognizing that $\delta\mathbf{U}$ is arbitrary requires that:

$$\begin{gathered} \int_{\Omega} \left( \boldsymbol{N}_U^T \rho \boldsymbol{N}_U \dot{\boldsymbol{U}} + \boldsymbol{N}_U^T \rho \boldsymbol{U} \nabla \cdot \boldsymbol{N}_U \bar{\boldsymbol{U}} + \boldsymbol{N}_U^T \rho \boldsymbol{F} \right) d\Omega + \\ \int_{\Omega} \left( -\nabla \cdot \boldsymbol{N}_U^T \boldsymbol{N}_P \bar{\boldsymbol{P}} + \nabla \cdot \boldsymbol{N}_U^T \boldsymbol{\tau} \right) d\Omega = 0 \end{gathered} \tag{4.12}$$

Equation 4.12 is the momentum equation's contribution to the system matrix equation.

### 4.2.3 System Matrices and Load Vector for a Single Component Fluid

Equations 4.7 and 4.12 govern the flow of a single component fluid. In finite element form, they form a matrix equation which, when inverted allows the unknown nodal velocities and pressures to be determined.

Combining equations 4.7 and 4.12 in matrix form yields:

$$\begin{bmatrix} \boldsymbol{M}_U & \boldsymbol{0} \\ \boldsymbol{0} & \boldsymbol{0} \end{bmatrix} \begin{bmatrix} \dot{\boldsymbol{U}} \\ \dot{\boldsymbol{P}} \end{bmatrix} + \begin{bmatrix} \bar{\boldsymbol{K}}_U + \boldsymbol{K}_U & \boldsymbol{Q} \\ \boldsymbol{Q}^T & \boldsymbol{0} \end{bmatrix} \begin{bmatrix} \bar{\boldsymbol{U}} \\ \bar{\boldsymbol{P}} \end{bmatrix} = \begin{bmatrix} -\boldsymbol{F} \\ \boldsymbol{0} \end{bmatrix} \qquad \textbf{(4.13)}$$

The reader is referred to Appendix 4.1 for the individual matrix components.

## 4.3 Finite Element Equations for Two-Component Flow

In this section, the ideas presented in the preceding section will be extended to two-component flows, the subject of this study. To preserve the clarity of the presentation, only those concepts that are unique to two-component systems are outlined. The general notions of the finite element equations for the mixtures are identical to those presented earlier.

### 4.3.1 Continuity Equations for Two-Component Mixtures

Recalling the continuity relations from Chapter 2,

$$\nabla \cdot \boldsymbol{V} = 0 \qquad \textbf{(4.14)}$$

and

$$2\frac{\partial n}{\partial t} + \nabla \cdot \boldsymbol{W} = 0 \qquad \textbf{(4.15)}$$

Equations 4.14 and 4.15 are multiplied by virtual fluid pressures ($\delta P_f$) and virtual porosities ($\delta n$), respectively. After following the integration and discretization process outlined for a single component fluid, the resulting finite element continuity equations are

$$\int_{\Omega} N_p^T \nabla \cdot N_V \, d\Omega \; \bar{V} = 0 \tag{4.16}$$

and

$$\int_{\Omega} N_n^T 2 N_n \, d\Omega \; \dot{n} + \int_{\Omega} N_n^T \nabla \cdot N_W \, d\Omega \; \bar{W} = 0 \tag{4.17}$$

The shape function subscripts refer to the particular polynomial form used for each unknown. A discussion of this follows later in this chapter.

### 4.3.2 Conservation of Momentum Equations for Two-Component Flows

Recall the conservation of momentum equation for the mixture, noting that only slow flows are dealt with in this study. Due to the slow flows, the advective terms have been eliminated, yielding

$$\frac{\partial}{\partial t}\left[V\hat{\rho} - W\Delta\rho\right] - \frac{1}{2}\nabla\cdot\left[\tau_{s_V} - \tau_{s_W}\right] + \nabla P_f + \nabla P_s - \bar{\rho} g = 0 \tag{4.18}$$

where

$$\hat{\rho} = \frac{\rho_s + \rho_f}{2}, \qquad \Delta\rho = \frac{\rho_s - \rho_f}{2}, \qquad \bar{\rho} = \rho_s - n(\rho_s - \rho_f) \tag{4.19}$$

with the granular component stress, $P_s$, a function of porosity as outlined in Chapter 3. The conservation of momentum equation for the fluid phase is:

$$\frac{\rho_f}{2}\frac{\partial}{\partial t}\left[V + W\right] - \frac{1}{2}\nabla\cdot\left[\tau_{f_V} + \tau_{f_W}\right] + \nabla(nP) - \beta(U_s - U_f) - \rho_f n g = 0 \tag{4.20}$$

The mixture momentum requires no further explanation and its finite element equivalent results from multiplying it by the virtual velocity $\delta\mathbf{V}$, integrating over the domain and descritizing according to the finite element procedure. The resulting finite element equation is

$$\begin{aligned}&\int_\Omega N_V^T\hat{\rho}N_V\dot{V} - N_V^T\Delta\rho N_W\dot{W}\,d\Omega + \int_\Omega \nabla\cdot N_V^T\frac{1}{2}\left[\tau_{s_V} - \tau_{s_W}\right]d\Omega \\ &- \int_\Omega \nabla\cdot N_V^T N_P\bar{P}_f + \nabla\cdot N_V^T P_s\,d\Omega + \int_\Omega N_V^T(\rho_s - \rho_f)g N_n\bar{n}\,d\Omega = \int_\Omega N_V^T\rho_s g\,d\Omega\end{aligned} \tag{4.21}$$

Similarly, the fluid component equation is straight forward. However, the drag term must be converted from the original component velocities ($\mathbf{U}_s$, $\mathbf{U}_f$) into the new pseudo velocities ($\mathbf{V}$,$\mathbf{W}$). Recall that

$$V_f = \frac{V + W}{2n}, \qquad V_s = \frac{V - W}{2(1-n)} \tag{4.22}$$

which, after some simple algebra, means that

$$\beta(U_s - U_f) = \frac{\beta}{1-n}\left[W\left(\frac{1}{2n}\right) - V\left(1 - \frac{1}{2n}\right)\right] \tag{4.23}$$

Substituting equation 4.23 into equation 4.20 and once again going through the process of forming finite element equations, the finite element equivalent of the fluid component conservation of momentum equation is:

$$\begin{aligned}
&\int_\Omega N_W^T \frac{\rho_f}{2} N_V \dot{V} + N_W^T \frac{\rho_f}{2} N_W \dot{W}\, d\Omega + \int_\Omega \nabla \cdot N_W^T \frac{1}{2} \nabla \cdot \left[ \tau_{f_V} + \tau_{f_W} \right] d\Omega \\
&- \int_\Omega \nabla \cdot N_W^T n N_P \bar{P}\, d\Omega \\
&- \int_\Omega N_W^T \frac{\beta}{1-n} \left( \frac{1}{2n} \right) N_W \bar{W} - N_W^T \frac{\beta}{1-n} \left( 1 - \frac{1}{2n} \right) N_V \bar{V}\, d\Omega \\
&- \int_\Omega N_W^T \rho_f g N_n \bar{n}\, d\Omega = 0
\end{aligned} \tag{4.24}$$

The four finite element equations (equations 4.16, 4.17, 4.21 and 4.24) can be combined to form the simultaneous, non-symmetrical equations allowing the unknowns (V, W, $P_f$, n) to be solved. This matrix equation takes the form:

$$\begin{bmatrix} M_{1V} & M_{1W} & 0 & 0 \\ M_2 & M_2 & 0 & 0 \\ 0 & 0 & 0 & 0 \\ 0 & 0 & 0 & M_n \end{bmatrix} \begin{bmatrix} \dot{V} \\ \dot{W} \\ \dot{P}_f \\ \dot{n} \end{bmatrix} + \begin{bmatrix} K_{s_V} & -K_{s_W} & -Q_P & L_{P_s} + L_{n_s} \\ K_f + R & K_f - R & -Q_{P_f} & L_{n_f} \\ Q_P^T & 0 & 0 & 0 \\ 0 & Q_n^T & 0 & 0 \end{bmatrix} \begin{bmatrix} \bar{V} \\ \bar{W} \\ \bar{P}_f \\ \bar{n} \end{bmatrix} = \begin{bmatrix} f + f_{P_s} \\ 0 \\ 0 \\ 0 \end{bmatrix} \tag{4.25}$$

The reader is referred to Appendix 4.2 for the individual matrix components.

## 4.4 Transient Solution Technique

In a simplified format, the governing set of equations (equation 4.13 for a single component fluid or equation 4.25 for a two component mixture) may be written in compact form as:

$$M\dot{a} + Ka = f \tag{4.26}$$

where **a** is the vector of unknowns, $\mathbf{a}^T = \{\mathbf{V}, \mathbf{W}, \mathbf{P}_f, \mathbf{n}\}$ for the two component mixture (the overbar notation for nodal unknowns has been dropped here for clarity).

Now, assuming a finite difference scheme for **a**:

$$\dot{a} = \frac{a^{t+\Delta t} - a^{t}}{\Delta t} \tag{4.27}$$

Equation 4.26 becomes:

$$M\left[a^{t+\Delta t} - a^{t}\right] + K\Delta t a^{t+\Delta t} = f\Delta t \tag{4.28}$$

or:

$$\left[M + \Delta t K\right] a^{t+\Delta t} = f\Delta t + M a^{t} \tag{4.29}$$

This form of time integration is referred to as an implicit scheme, where the system matrix and load vector are evaluated at the end of the time step. It is often difficult for non-linear properties to obtain these in an appropriate form and so one must therefore, resort to predictor-corrector schemes.

**Step 1:** solve 4.29 using with matrices evaluated at the beginning of the time step.

**Step 2:** use the new values of the variables to evaluate the matrices at the end of the time step.

**Step 3:** Repeat Steps 1 and 2 until convergence is achieved.

Where possible, it is more efficient to ***implicitly*** include the values of various quantities at the end of the time step. One method to achieve this is to use a Taylor's expansion to estimate these values. This is especially important when a quantity undergoes large changes with small changes in the unknowns. Consider, for example, the exponential nature of the granular component pressure ($P_s$) model where small changes in porosity ($n$) can result in large changes in the $P_s$. Given that (refer to Chapter 3)

$$P_s = \exp\left[\frac{1}{A}\left(1 - \frac{1-\hat{n}}{1-n}\right)\right] \tag{4.30}$$

an implicit scheme requires that $P_s$ be evaluated at the end of the time step. To estimate this, a truncated, first-order Taylor's expansion is employed where:

$$\begin{aligned} P_s^{t+\Delta t} &= P_s^t + \left(\frac{\partial P_s}{\partial n}\right)^t \Delta n \\ &= P_s^t + \left(\frac{\partial P_s}{\partial n}\right)^t \left(n^{t+\Delta t} - n^t\right) \\ &= P_s^t + \left(\frac{\partial P_s}{\partial n}\right)^t n^{t+\Delta t} - \left(\frac{\partial P_s}{\partial n}\right)^t n^t \end{aligned} \tag{4.31}$$

The granular stress component of the momentum equation is therefore:

$$\begin{aligned} &\int_\Omega \nabla\cdot N_V^T P_s^{t+\Delta t}\, d\Omega = \\ &\int_\Omega \nabla\cdot N_V^T P_s^t\, d\Omega - \int_\Omega \nabla\cdot N_V^T \left(\frac{\partial P_s}{\partial n}\right)^t n^t\, d\Omega + \int_\Omega \nabla\cdot N_V^T \left(\frac{\partial P_s}{\partial n}\right)^t N_n n^{t+\Delta t}\, d\Omega \end{aligned} \tag{4.32}$$

This modification eliminates the need for a predictor-corrector iteration, thus improving the efficiency of the solution procedure.

## 4.5 General Element Selection Criteria

Reviewing the four finite element equations, and the boundary terms in particular, it may be observed that the unknown variables have associated with them derivatives of various order which implies different minimum continuity requirements

| Unknown | Highest Order Derivative | Continuity Requirements |
|---|---|---|
| V | 1 | $C_0$ |
| W | 1 | $C_0$ |
| P | 0 | no requirement |
| n | 0 | no requirement |

The continuity requirements provide a ***minimum*** standard for the elements. Beyond this requirement however, the underlying equations should be examined to determine whether different orders of interpolation of the variables with respect to one another are appropriate.

For example, consider a slow, steady single component flow through a one-dimensional expansion, the fluid momentum equation for this system reduces to:

$$-\frac{dP}{dx} + \frac{4}{3}\mu\frac{d^2U}{dx^2} = 0 \qquad (4.33)$$

An examination of this equation suggests that pressure should be interpolated with a function having one degree less than that used for velocity, to ensure that both terms vary in similar ways. For example, if a quadratic interpolation were to be used for velocity, pressure should vary linearly. Similar arguments can be presented for the integral equations of a two component mixture.

In general, the order of interpolation for the element is chosen as a compromise between accuracy (higher order interpolation being more accurate for equal element size) and computational efficiency (lower order interpolation having fewer degrees of freedom for a given element size).

### 4.5.1 A note on Porosity Interpolation

As just noted, it is not necessary for porosity to be continuous between elements. In fact there are good reasons to allow it to be discontinuous. Consider the sedimentation of granules in a fluid, a process distinguished by a sharp interface between clear liquid and a mixture of solid and liquid. The use of a discontinuous porosity interpolation allows this discontinuity to be more accurately modeled than a continuous interpolation.

The second reason for choosing a discontinuous interpolation (and more specifically a constant interpolation) is one of convenience. In several locations in the equations there are terms resembling:

$$\nabla \cdot (n\varphi) \tag{4.34}$$

which, after applying the chain rule, becomes:

$$n\nabla \cdot \varphi \; + \; \varphi \cdot \nabla n \tag{4.35}$$

The second term above drops out if porosity is assumed to be constant over the element. By introducing constant porosity in each element, the discretized hydrodynamic equations are greatly simplified. Of course, such a simplification does introduce numerical errors. However, this error can be decreased by increasing the number of elements.

## 4.6 One-Dimensional Problems

There are a few circumstances where the flow of a two-phase mixture can be considered to be one-dimensional. A few examples are pneumatic conveying of granular solids, slurry flow and certain classes of consolidation and liquefaction problems in soil mechanics. In addition to the analysis of these special cases, one-dimensional models allow the numerical solution technique to be verified with less complication than arises in two-dimensional analysis. For this reason, the finite element solution to some simple one-dimensional problems is considered first.

### 4.6.1 One-Dimensional Elements

A one-dimensional element considered in this section for two-phase flow has the following features:

- Unknowns: V, W, $P_f$, n
- Variable area
- Arbitrary inclination with respect to gravity

Figure 4.1 shows the general one-dimensional element. Two element types that were used and compared are:

| | |
|---|---|
| **1VW/0P/0n** | Linear velocity (V,W), constant (and discontinuous) pressure and porosity |
| **2VW/1P/0n** | Quadratic velocity (V,W), constant porosity and linear pressure |

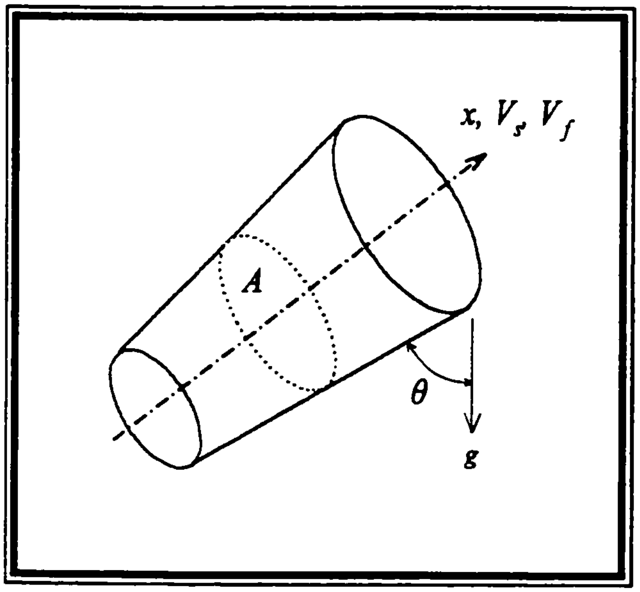

**Figure 4.1**: Flow Geometry

To compare the performance of the two elements, an analysis of a simple scenario was performed. The analysis considered is one-dimensional fluidization in a vertical column for a stationary mixture having an initial porosity of 0.65. The fluid inflow velocity was then changed to a level that produced a porosity of approximately 0.71 at steady state. The solid component was composed of individual grains, each having densities of 2600 kg/m$^3$ and a diameter of 0.30 mm. The fluidizing liquid was water at 20°C.

Figure 4.2 compares the porosity distribution in the column at an intermediate time (i.e., before reaching steady state). For this analysis, equal element sizes were used. The simulated column height is 1.0m and 100 elements were used; i.e., the element length is therefore 1cm.

It may be observed from the predicted porosity distribution shown in Figure

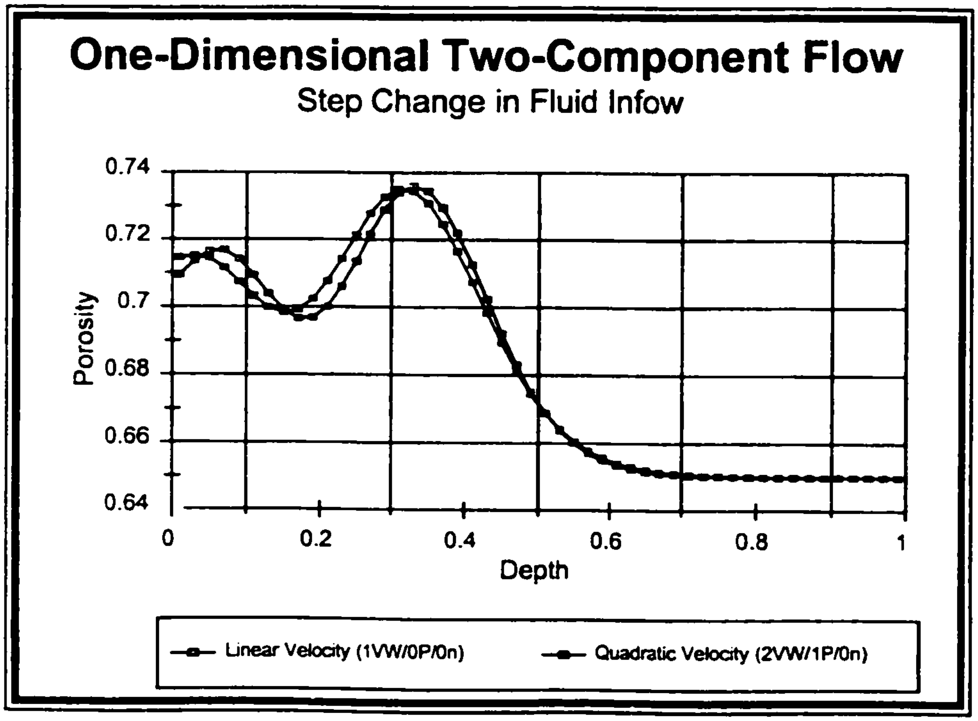

**Figure 4.2**: Comparison of 1-D Elements

4.2, that the two elements perform nearly identically. It appears that there is a very small shift in the response but this is quite slight. It may also be observed in Figure 4.2 that there is an overshoot of the final porosity level (0.716). The overshoot is not affected by the element density nor the time step size and so it is not a function of the numerical method. Rather, it is a function of the model itself. The simulation predicts that the solid particles are swept up by the rapid change in the fluid velocity. This rapid propulsion of the particles creates a zone that is partially devoid of particles and an adjacent zone that has surplus particles. As the wavefront passes, an oscillation between these two zones is created which takes some time to die out. This suggests that there may be some energy dissipation mechanism missing from the model. However, it should be noted that the overshoot is small (a maximum of ± 2% porosity) and the overall response is in good agreement with experimental results (refer to Chapter 5).

Although the above example is quite simple, it does test the movement of a porosity front sweeping through the column, which, in our experience is a challenge to model because of the sharp transition from one porosity level to another. It may be concluded that both of the proposed element formulations for one-dimensional flow analysis of two-component mixtures are adequate. The reader is referred to Chapter 5 for a more thorough description of this simulation, complete with sensitivity analysis to different properties, time increments and element sizes.

### 4.6.2 Reduced Variable Model

Lyczkowski et al. (1978) analyzed the character of the hydrodynamic equation set for two component mixtures and found that the equations are ill-posed. Therefore, a stable solution may be difficult or impossible to find (although our experience has shown this is not always the case). In order to overcome this problem, they recommend a revised set of momentum equations where fluid pressure is eliminated from the solids phase momentum equation by introducing a revised drag coefficient ($\beta_B$). For one dimensional flow with variable area, the revised equation set becomes

$$\frac{\partial}{\partial t}\left(An\rho_f\right) + \frac{\partial}{\partial x}\left(An\rho_f U_f\right) \tag{4.36}$$

$$\frac{\partial}{\partial t}\left(A(1-n)\rho_s\right) + \frac{\partial}{\partial x}\left(A(1-n)\rho_s U_s\right) \tag{4.37}$$

$$\frac{\partial}{\partial t}\left(A(1-n)\rho_s U_s\right) + \frac{\partial \boldsymbol{S}_s}{\partial x} - A\beta_B\left(U_f - U_s\right) + A\left((1-n)\rho_s + n\rho_f\right)g\cos\theta = 0 \tag{4.38}$$

$$\frac{\partial}{\partial t}\left(An\rho_f U_f\right) + \frac{\partial}{\partial x}\left(AP_f\right) + A\beta_B\left(U_f - U_s\right) + A\rho_f g\cos\theta = 0 \tag{4.39}$$

where $\mathbf{S}_s$ is the solids phase stress tensor. Equations 4.36 - 4.39 are convenient because they allow an extremely efficient form of one-dimensional problems to be extracted.

Using a procedure similar to that outlined in the previous chapter for the simplified hydrodynamic model (i.e., replacing the fluid and solid velocities with pseudo-velocities V and W), the continuity equations become

$$\frac{\partial V}{\partial x} = 0 \tag{4.40}$$

$$2A\frac{\partial n}{\partial t} + \frac{\partial W}{\partial x} = 0 \tag{4.41}$$

where in this case

$$V = A\left(nU_f + (1-n)U_s\right) \qquad W = A\left(nU_f - (1-n)U_s\right) \tag{4.42}$$

In equation 4.42, V is the volume flow rate. Integrating equation 4.40 yields

$$V = c \tag{4.43}$$

ie., the volume flow rate is constant throughout the domain (as one might expect) and equal to the boundary value flow rate, which may be prescribed at **either** the inlet or outlet. This result leaves only the difference velocity and porosity to be determined. The porosity may be eliminated via the following finite element and temporal discretization process.

The integrated equivalent of equation 4.41 is

$$\int_0^l \delta n\left(2A\frac{\partial n}{\partial t} + \frac{\partial W}{\partial x}\right)dx = 0 \tag{4.44}$$

Given constant porosity and linear interpolation for velocity, equation 4.44 becomes

$$(A_1 + A_2)\, l \frac{\partial n}{\partial t}\left(\frac{W_1 - W_2}{l}\right) = 0 \tag{4.45}$$

Equation 4.45 is strictly for a linear interpolation element but that an analogous expression can be produced for any 1-D, element type). Finally, if an implicit finite difference scheme is employed for porosity, then

$$n^{t+\Delta t} = n^{t} + \frac{\Delta t}{A_1 + A_2}\left(\frac{W_1 - W_2}{l}\right) \tag{4.46}$$

By substituting equations 4.43, 4.44 and 4.46 into the granular component momentum equation (eq. 4.38), W becomes the only variable remaining to be solved. The resulting equation is (neglecting the granular stress):

$$\frac{\rho_s}{2}\frac{\partial}{\partial t}(W - c) + \beta^{*} W - A\left[\rho_s - (\rho_s - \rho_f)n^{t+\Delta t}\right] g\cos\theta = 0 \tag{4.47}$$

The implication of equation 4.47 is that a system formally having four simultaneous equations for four unknowns has been reduced to one equation with a single unknown. This reduces the computational effort to solve this system significantly. The other variables (porosity and pressure) are updated after each time step.

Chapter 5 provides detailed discussions of simulations based on the reduced variable formulation complete with a comparison to the standard element formulations that were discussed in section 4.6.1.

## 4.7 Two-Dimensional Problems

Although there are several classes of problems that may be described as one-dimensional, two-dimensions are often required to analyze more general problems. The continuity and interpolation criteria described for the one-dimensional elements have also been used for the two-dimensional elements.

### 4.7.1 Previous Research on Two-Dimensional Elements

The vast majority of computational work in fluid dynamics has been devoted to the finite difference (FDM) and finite volume (FVM) approaches. For both tangible and less tangible reasons, the finite element method was selected to model the two-component flows under consideration in this thesis. Owing to the limited volume of work reported in the literature for finite element applications in both single and two-component flow modeling, determining suitable element formulations presented a unique challenge in this thesis. However, some work in the use of finite elements for two-component flow has been reported.

As a whole, workers in the field of two-component flows have encountered stability issues when using standard Galerkin formulations applied to the primitive variable equation set. These instabilities appear to manifest themselves as oscillations in the pressure field and macroscopic solution instability due to sharp gradients. Both of these instabilities are consistent with findings from initial work performed for this thesis (see

Chapter 2). In order to solve these stability issues, it appears that three main approaches have been used.

A great deal of research has and continues to be performed in dealing with the problem of spurious pressure oscillation (known also as "checkerboarding"). This is especially true for the very popular bi-linear velocity constant pressure element. Two avenues of dealing with this instability are to (i) choose selectively the interpolation of the velocity and pressure degrees of freedom and (ii) add so-called stabilization terms to the continuity equation.

It may be stated in general that the steady component of the system matrix for the Navier-Stokes equation has the following form:

$$\begin{bmatrix} \boldsymbol{K} & \boldsymbol{Q} \\ \boldsymbol{Q}^T & \boldsymbol{0} \end{bmatrix} \tag{4.48}$$

Several authors have attributed the pressure instability to the null diagonal term and suggest the addition of a stabilization term ( Zienkiewicz and Taylor, 1989, Nigro et al.,1994, Pastor et al., 1997).

Another method of dealing with the pressure oscillation problem is the addition of a so-called bubble function to the interpolation of velocity. The bubble function assumes a value of unity at the center of an element and zero at the edges. One can immediately see that since this additional term reduces to zero along the boundary, it has the effect of "relaxing" the constraints on velocity between elements. An excellent review of this method may be found in Fortin and Fortin (1985).

The second instability reported in the literature is due to sharp gradients in porosity. Hiltunen (1997) proposes a "discontinuity capturing operator" in his work on two-component flow modeling. A description of this method is beyond the scope of this thesis and the reader is referred to the original paper. In a general sense, the operator acts as an artificial diffusivity term with the gradient of porosity acting as the driving force, i.e.:

$$\bar{D}_s = \bar{D}_s(\kappa \nabla n) \tag{4.49}$$

where κ is a diffusivity constant. It is felt that such an additional term is artificial and, in the context of the revised equation set presented herein, unnecessary and so will be avoided in this thesis.

A third approach to stabilizing a finite element solution for both pressure and porosity induced oscillations is to disguise a finite volume method as a finite element solution. This method uses interpolation characteristics of the finite element method but employs a control volume approach to integrating the governing equations, thus avoiding the problem of extreme porosity gradients (Masson and Baliga, 1994).

### 4.7.2 Two-Dimensional Elements

Owing to the fact that in our equation set, the continuity equations are linear and the hydrodynamic drag term appears in only one of the two momentum equations, standard finite elements were successful in the solution of the equations, in spite of the negative findings of previous research mentioned in section 4.7.1. Several element types were evaluated for their performance in solving the flow of mixtures of granular solids and fluids. Table 4.1 summarizes the elements that were evaluated in the research in this thesis. Figure 4.3 gives a diagram of each of the elements studied including the node locations. To compare the elements, the simple fluidization simulation that was used to validate the one-dimensional code was again used for the two-dimensional code.

**Table 4.1: Two-Dimensional Element Descriptions**

| Reference Number | Element Shape | Number of Nodes | Velocity (V,W) Interpolation | Pressure Interpolation | Porosity Interpolation |
|---|---|---|---|---|---|
| 2DT1 | Triangular | 7 | Quadratic | Linear | Constant |
| 2DT2 | Triangular | 6 | Quadratic | Linear | Linear |
| 2DT3 | Triangular | 4 | Linear | Constant | Constant |
| 2DT4 | Triangular | 10 | 4-Linear Elements | Linear | 4-Constant Elements |
| 2DT5 | Triangular | 3 | Linear | Co-Located Constant | Constant |
| 2DQ1 | Quadrilateral | 5 | Bi-Linear | Constant | Constant |
| 2DQ2 | Quadrilateral | 5 | Bi-Linear | Co-Located Constant | Constant |

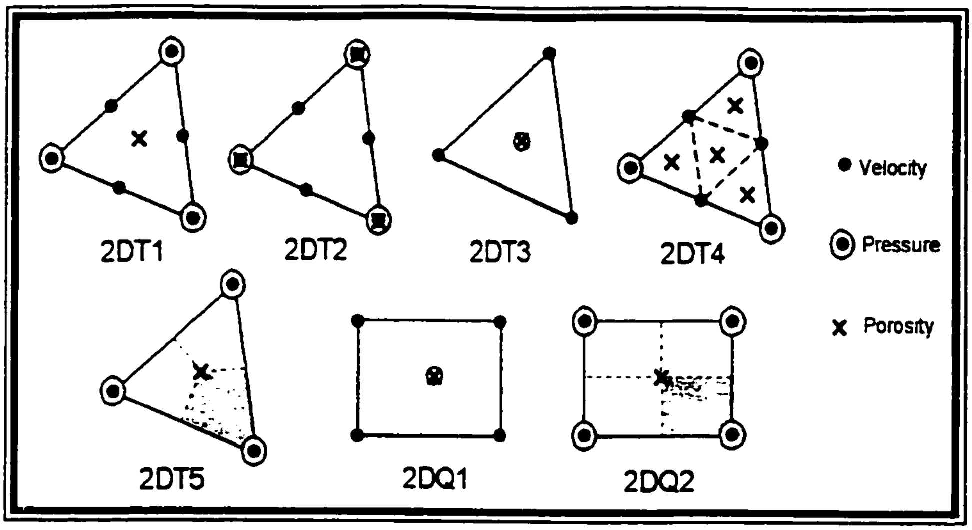

**Figure 4.3**: Element Configurations

Each of the two-dimensional elements of Table 4.1 was used to model an essentially one-dimensional problem. No special solution techniques, such as stabilization schemes, were employed. The porosity distribution in the simulated fluidization column was recorded at an intermediate time before steady state was achieved. In many cases, the solution became wildly unstable before this time. Figure 4.4 shows a plot of the porosity distributions for each of the four stable elements.

It was found that there are stability problems with those elements employing quadratic interpolation for velocity. This may be attributed to the response of quadratic interpolation to the propagation of a wave front. Therefore, only linear velocity interpolation was subsequently employed for two-dimensional analyses completed for this thesis. Figure 4.4 reveals that there are some differences in the transient response of the four stable elements (noting that the steady state results for all stable elements were identical). These are characterised by minor differences in the timing of the response which is attributable to spatial differences in the integration domain of the variables owing to the specific make-up of each element.

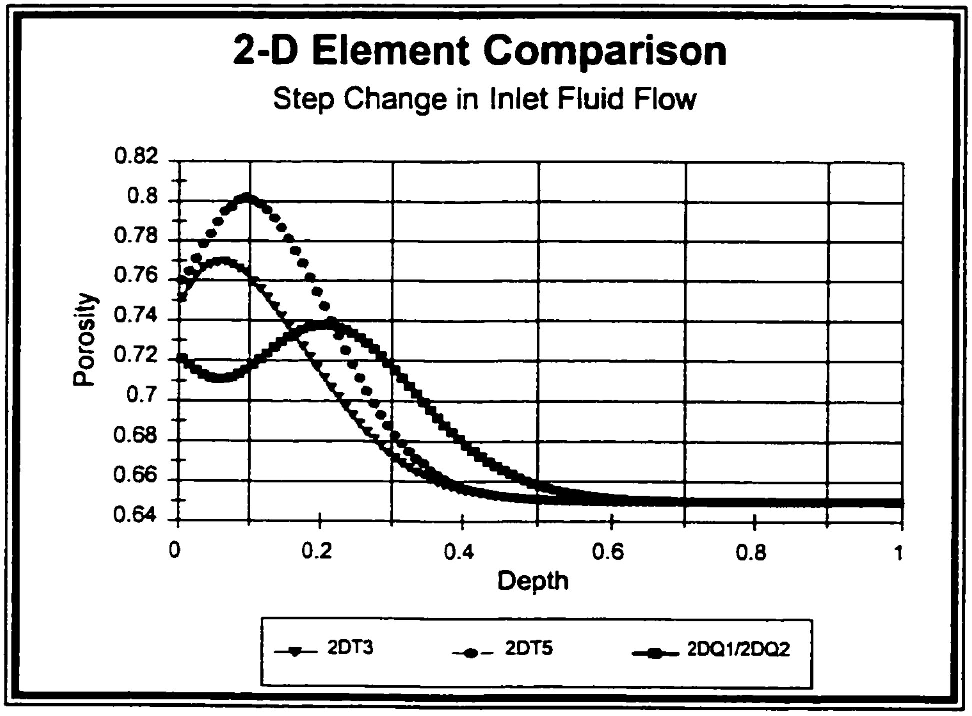

**Figure 4.4**: Comparison of 2-D Element Response

Referring to Figure 4.5, suppose a wave front travels through an element where velocity goes from one level to another with a sharp gradient. Owing to the characteristic of the quadratic interpolation, the element is forced to predict a reversal of the velocity change through the element, whereas a linearly interpolated element is able to correctly track the wave front. This reversal of the velocity is believed to initiate an instability in the solution, which increases with successive time steps.

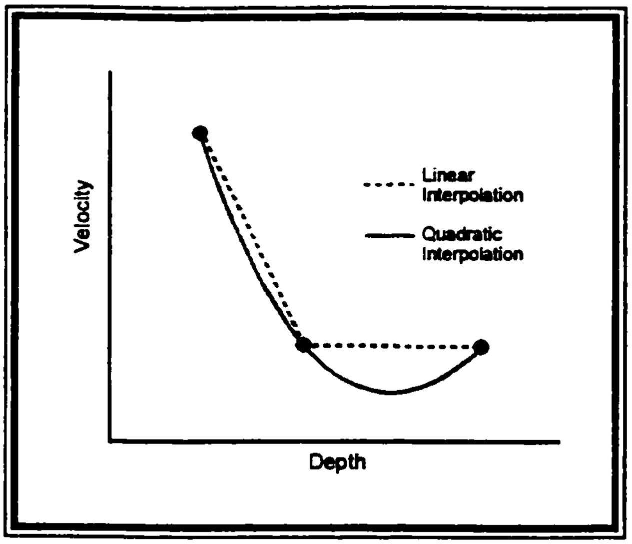

**Figure 4.5**: Velocity Reversal due to Quadratic Interpolation

Four of the two-dimensional linear velocity interpolation elements provided stable solutions for the one-dimensional test problem. Unfortunately, two of those elements have fatal flaws preventing their use in fully two-dimensional analyses. The first of these elements is the linear velocity, constant pressure element (2DT3). As explained in Zienkiewicz and Taylor (1989), this element suffers from locking due to the incompressible condition. Consider Figure 4.6 which shows two elements in a corner of the domain. Incompressibility in element 1 limits the movement of node A to horizontal velocities only. Additionally, incompressibility in element 2 limits the velocity of node A to the vertical direction. Therefore, the only admissible velocity of node A is zero in both directions. This locking propagates throughout the domain, and hence, this element is not useful in general two-dimensional elements.

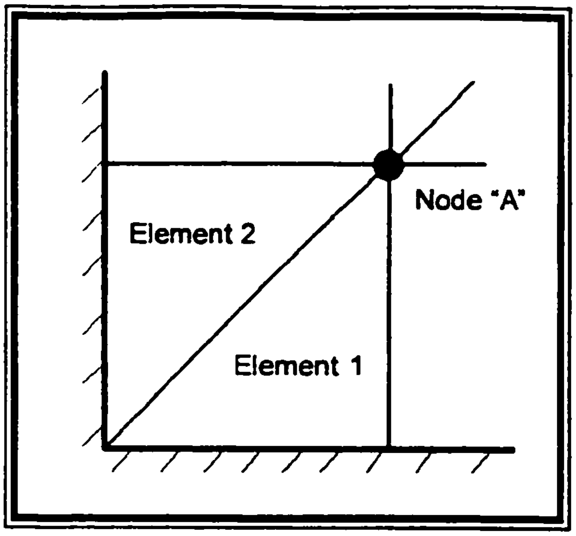

**Figure 4.6**: Incompressible Locking

To possibly overcome this locking phenomenon, a staggered mesh approach incorporating triangular elements was attempted, whereby the continuity equations were integrated over local domains different than those corresponding to the momentum equations. This scheme led to the linear velocity co-located pressure element (2DT5). Unfortunately, this element suffered from severe pressure "checker-boarding" where the pressure from one element to the next would oscillate about the correct value. The reader is referred to Figure 4.7 for a plot of the pressure distribution for the one-dimensional test problem. Although solutions to this problem were not pursued, this approach, if the checker-boarding can be overcome, is very attractive, as the 3-node triangular element is highly versatile.

Solutions to the pressure oscillation problem of the 2DT5 element were not pursued because success in modeling two-dimensional problems was achieved using the bi-linear constant pressure, constant porosity element 2DQ1. This element did not suffer from the locking of its triangular brethren, for the problems analyzed in this thesis, and it had the additional benefit of being a simple, low-bandwidth element. For these reasons, it was selected for all future two-dimensional simulations. Chapter 5 presents examples of simulations used to validate the code using this element. It should be noted that the performance of a co-located pressure version of this element (2DQ2) was also tried. It suffered from the same checker-boarding as 2DT5.

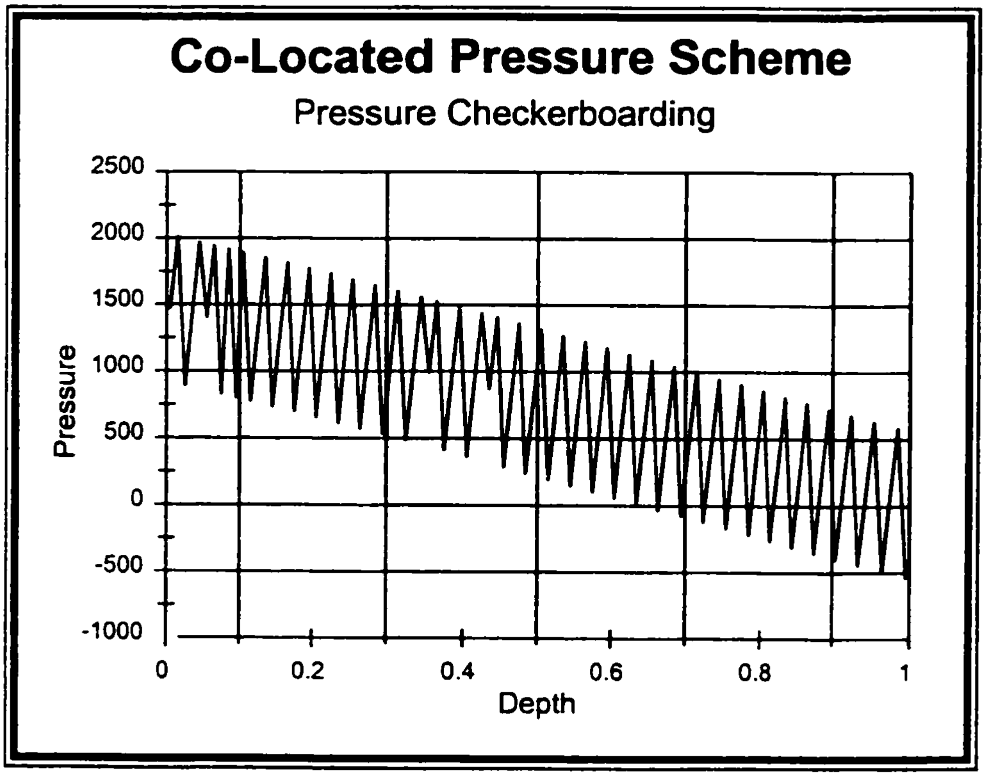

**Figure 4.7**: Pressure Checker-Boarding in 2DT5

### 4.7.3 Axi-symmetric Element with Out of Plane Velocity

Axi-symmetric analyses are a simple extension of a two-dimensional model. A description of the formulation of such analyses is covered thoroughly in Zienkiewicz and Taylor (1989) for example. In usual axi-symmetric analyses, velocity is confined to the plane of symmetry. In some cases however, it is beneficial to include out of plane velocity components in an otherwise axi-symmetric problem. In such problems the inherent computational efficiency of the axi-symmetric formulation (having only a planar domain) may be exploited over a fully three-dimensional analysis (requiring a full three dimensional domain with an associated increase in elements, nodes and degrees of freedom).

Such a case is that of the rotating viscometer discussed in Chapter 3. In this apparatus, the fluid and solid velocity components have, in addition to the usual planar components, an out of plane component generated by the rotating spindle. This results in helical streamlines which may be described using only two co-ordinates.

The generation of the finite element equations is identical to the planar case outlined previously. There are only three things that need to be changed from the standard two-dimensional analysis:

- A third velocity component needs to be added (the three co-ordinate directions are r, z and $\theta$)
- The integration area becomes a toroid traced by the

planar element about the axis of symmetry. In the case of the rotating viscometer, this is the spindle axis.

- The rate of deformation tensor becomes:

$$\left[\frac{\partial u_r}{\partial r},\ \frac{\partial u_z}{\partial z},\ \frac{u_r}{r},\ \frac{\partial u_r}{\partial z}+\frac{\partial u_z}{\partial r},\ \frac{\partial u_\theta}{\partial r}-\frac{u_\theta}{r},\ \frac{\partial u_\theta}{\partial z}\right] \qquad \textbf{(4.50)}$$

where u is a general velocity vector such as the fluid or solid component velocity.

As an initial check on the derivation of the model, a finite element analysis was performed on the rotating viscometer with an imaginary single component fluid having properties similar to a fluidized mixture of sand and water (density of 1600 kg/m$^3$ and a viscosity of 1 Pa·s). Figure 4.8 shows the geometry of the problem including the finite element mesh.

The boundary conditions (see Figure 4.8) consist of a uniform inlet velocity and no slip conditions applied to the wall and rotating cylinder. Figures 4.9, 4.10 and 4.11 show the resulting in-plane and out of plane velocity profiles respectively. Figure 4.12 shows the calculated pressure distribution (with the hydrostatic component removed). The results of the finite element solution in the fully developed region were compared with analytical flow profiles and the resulting error for both in plane and out of plane velocity was less than 2 percent (see Table 4.2).

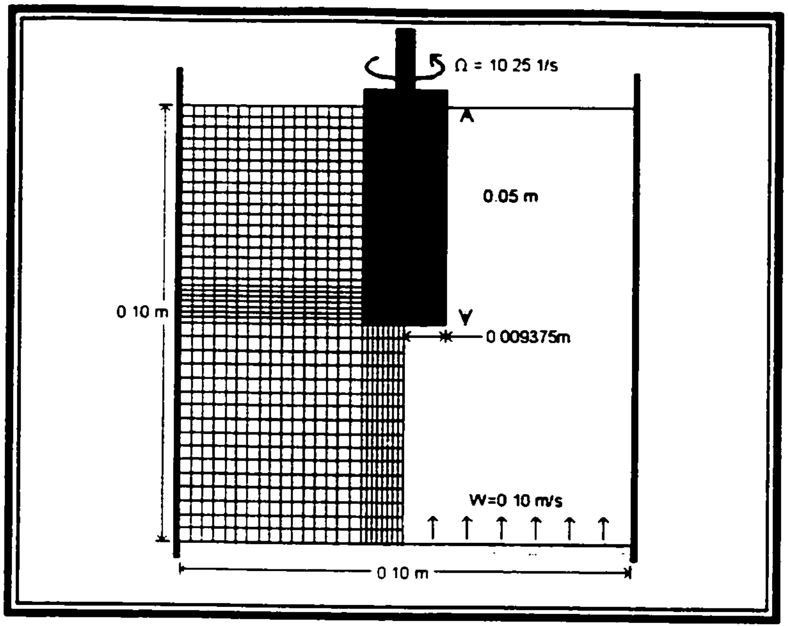

**Figure 4.8**: Rotating Viscometer Geometry

**Table 4.2: Flow Velocity Error**

| Flow Velocity | Error |
|---|---|
| In plane (z-direction) | 1.8% |
| Out of Plane (θ-direction) | 1.6% |

It may be observed in Figure 4.12 that there is slight checker boarding of the pressure field which is to be expected with the 4-node quadrilateral element (LeTallec and Ruas, 1986, Fortin and Fortin, 1985). The effect is slight when compared to the overall distribution of pressure and may be removed via post-processing smoothing.

A similar analysis has been completed with a two-component sand/water mixture. The results of this analysis is found in Chapter 5.

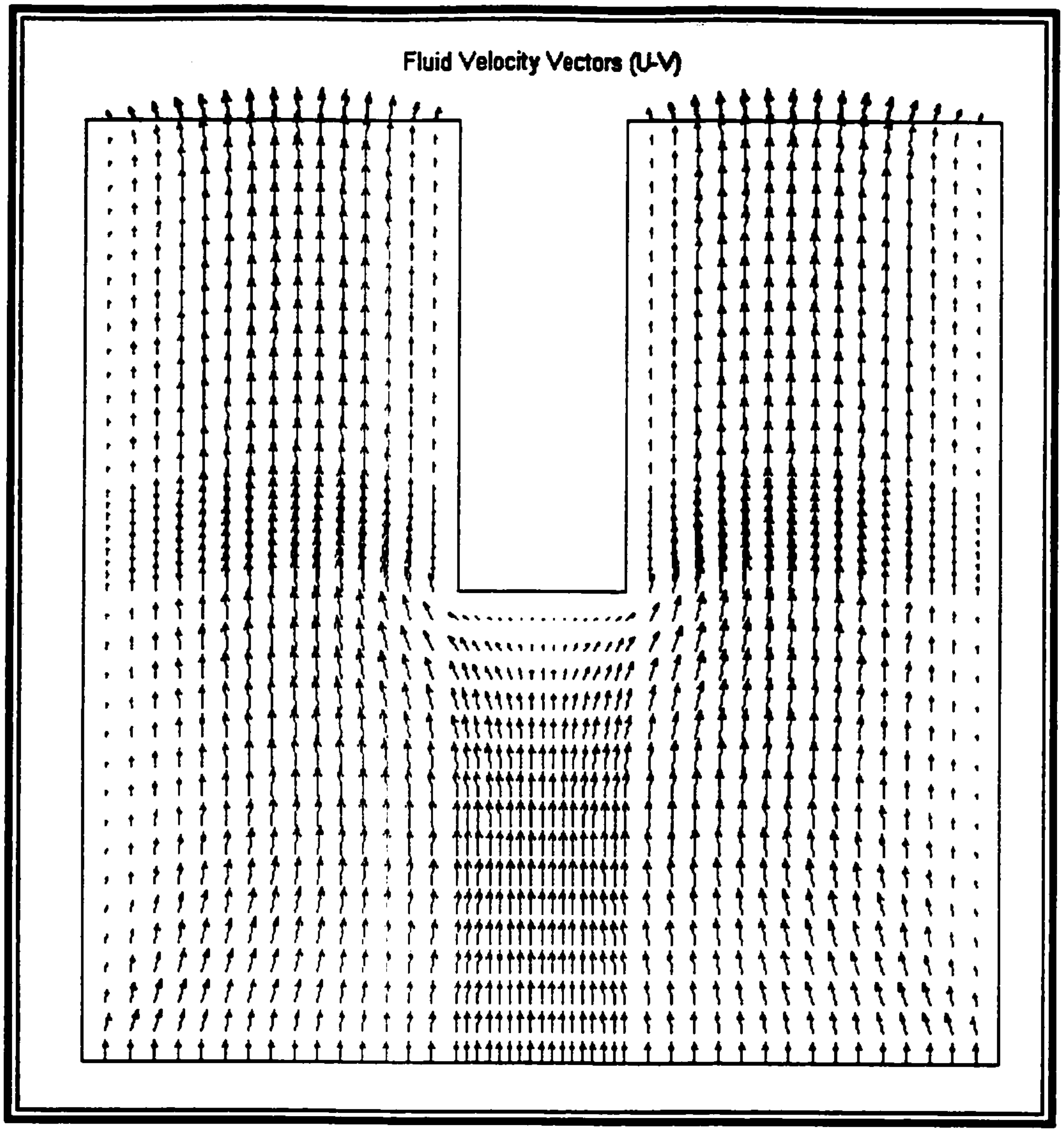

**Figure 4.9**: In-plane (r-z) Velocity Vectors for Rotating Cylinder Viscometer (scale 30mm = 1.0 m/s)

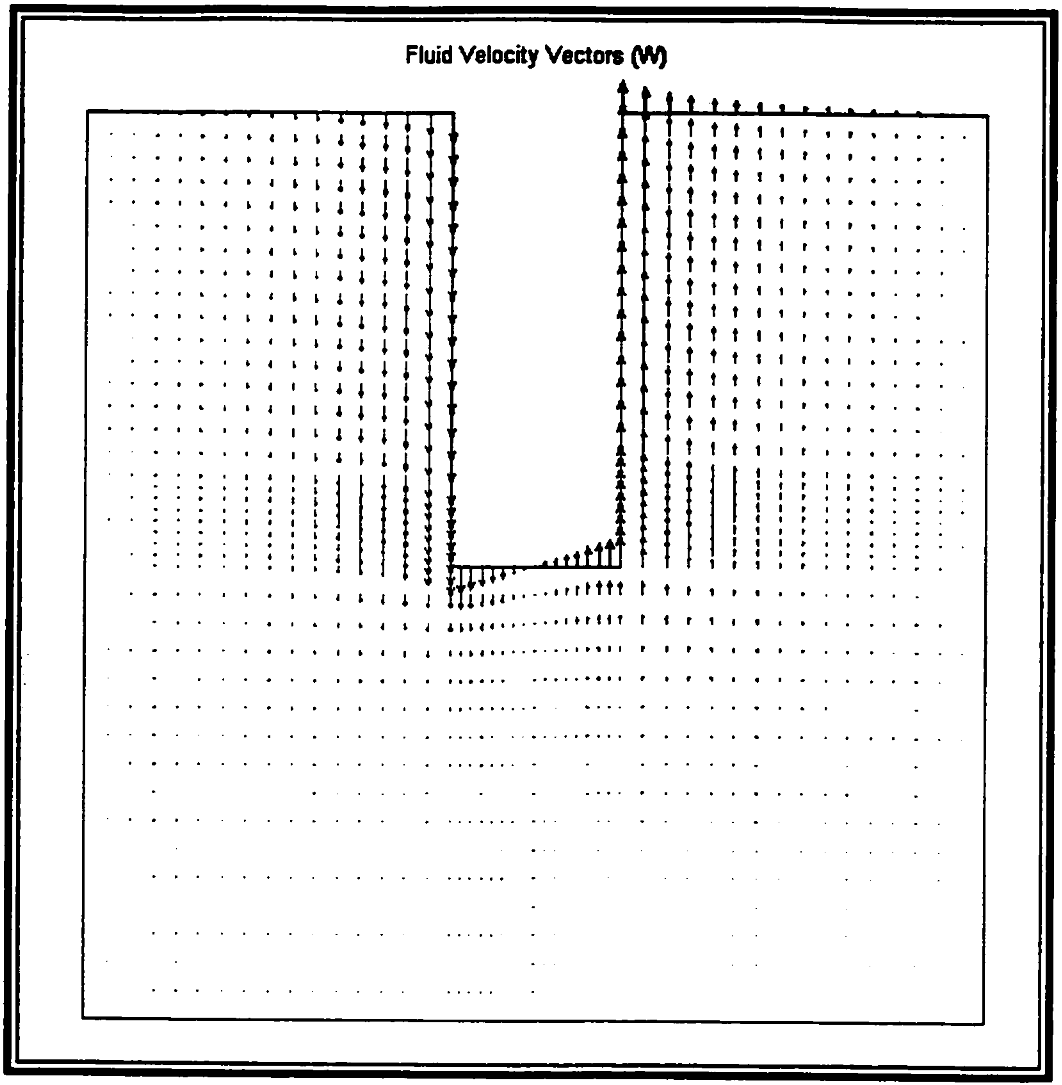

**Figure 4.10**: Out of Plane (θ) Velocity Vectors for Rotating Cylinder Viscometer (45mm = 1.0m/s)

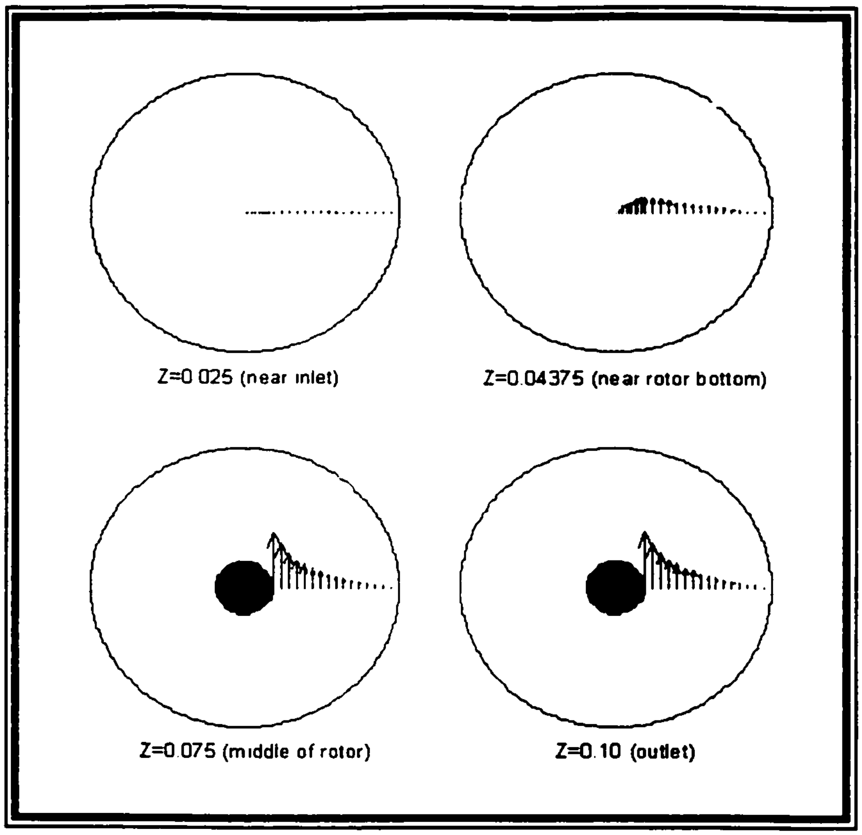

**Figure 4.11**: Section Views of Out of Plane (r-θ) Velocity Vectors for Rotating Cylinder Viscometer (scale 65mm = 1.0 m/s)

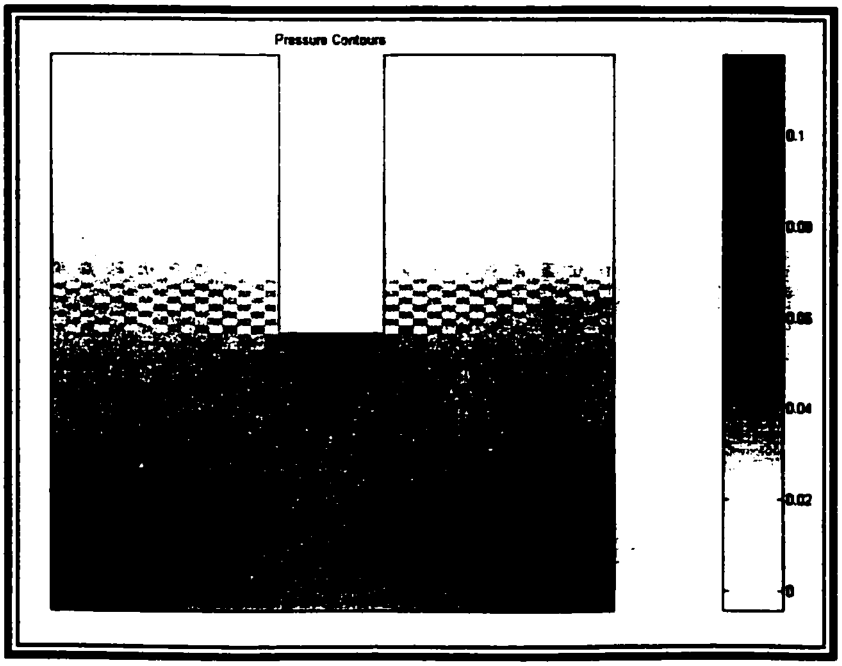

**Figure 4.12**: Pressure Field (in Pa) for Rotating Cylinder Viscometer (Hydrostatic head removed)

## 4.8 Summary

The governing equations derived in Chapter 2 have been recast in their finite element form in this chapter. A detailed explanation of the finite element equations has been provided for one-component systems for clarity. Similar procedures were followed for the two-component equations, the results of which are provided.

Both one and two-dimensional elements were considered and the factors for proper element selection were discussed. A brief discussion of the transient solution technique is provided along with a novel, reduced variable model. Finally, the use of an axi-symmetric formulation for problems having out of plane velocity was presented.

# APPENDIX 4.1 MATRIX ELEMENTS FOR SINGLE COMPONENT FLOW

The following are the individual matrix components for the single component equation system eq. 4.13, i.e.:

$$\begin{bmatrix} \boldsymbol{M}_U & 0 \\ 0 & 0 \end{bmatrix} \begin{bmatrix} \dot{\boldsymbol{U}} \\ \dot{\boldsymbol{P}} \end{bmatrix} + \begin{bmatrix} \bar{\boldsymbol{K}}_U + \boldsymbol{K}_U & \boldsymbol{Q} \\ \boldsymbol{Q}^T & 0 \end{bmatrix} \begin{bmatrix} \bar{\boldsymbol{U}} \\ \bar{\boldsymbol{P}} \end{bmatrix} = \begin{bmatrix} -\boldsymbol{F} \\ 0 \end{bmatrix}$$

where the integration is performed over the element volume.

$$\boldsymbol{M}_U = \int \boldsymbol{N}_U^T \rho \boldsymbol{N}_U \, dV$$

$$\bar{\boldsymbol{K}}_U = \int \boldsymbol{N}_U^T \boldsymbol{U} \boldsymbol{N}_U \, dV \qquad \boldsymbol{K}_U = \int \boldsymbol{B}_U^T \mu \boldsymbol{D} \boldsymbol{B}_U \, dV$$

$$\boldsymbol{Q} = \int \nabla \cdot \boldsymbol{N}_U^T \boldsymbol{N}_P \, dV$$

$$\boldsymbol{F} = \int \boldsymbol{N}_U^T \rho \boldsymbol{g} \, dV$$

## APPENDIX 4.2 MATRIX ELEMENTS FOR TWO-COMPONENT FLOW

The following are the individual matrix components for the two-component mixture equation system eq. 4.26, i.e.:

$$\begin{bmatrix} M_{1V} & M_{1W} & 0 & 0 \\ M_2 & M_2 & 0 & 0 \\ 0 & 0 & 0 & 0 \\ 0 & 0 & 0 & M_n \end{bmatrix} \begin{bmatrix} \dot{V} \\ \dot{W} \\ \dot{P}_f \\ \dot{n} \end{bmatrix} + \begin{bmatrix} K_{s_V} & -K_{s_W} & -Q_P & L_{P_s}+L_{n_s} \\ K_f+R & K_f-R & -Q_{P_f} & L_{n_f} \\ Q_P^T & 0 & 0 & 0 \\ 0 & Q_n^T & 0 & 0 \end{bmatrix} \begin{bmatrix} \bar{V} \\ \bar{W} \\ \bar{P}_f \\ \bar{n} \end{bmatrix} = \begin{bmatrix} f+f_{P_s} \\ 0 \\ 0 \\ 0 \end{bmatrix}$$

where the integration is performed over the element volume.

$$M_{1V} = \int N_V^T \left( \frac{\rho_s - \rho_f}{2} \right) N_V \; dV \qquad M_{1W} = \int N_V^T \left( \frac{\rho_s - \rho_f}{2} \right) N_V \; dV$$

$$M_2 = \int N_W^T \left( \frac{\rho_f}{2} \right) N_W \; dV \qquad M_n = \int N_n^T 2 N_n \; dV$$

$$K_{s_V} = \int B_V^T \mu_s D B_V \; dV \qquad K_{s_W} = \int B_W^T \mu_s D B_W \; dV$$

$$K_f = \int B_W^T \mu_f D B_W \; dV$$

$$Q_P = \int \nabla \cdot N_V^T N_P \; dV \qquad Q_{P_f} = \int \nabla \cdot N_W^T n N_P \; dV$$

$$Q_n = \int \nabla \cdot N_W^T N_n \; dV$$

$$L_{P_s} = \int \nabla \cdot N_V \left( \frac{\partial P_s}{\partial n} \right) N_n \; dV \qquad L_{n_s} = \int N_V^T (\rho_s - \rho_f) g N_n \; dV$$

$$L_{n_f} = \int N_W^T \rho_f g N_n \; dV$$

$$f = \int N_W^T \rho_s g \; dV \qquad f_{P_s} = \int \nabla \cdot N_V^T \left[ P_s - \left( \frac{\partial P_s}{\partial n} \right) n \right] dV$$

## APPENDIX 4.3 ANALYTIC SOLUTIONS FOR ROTATING CYLINDER VISCOMETER

In the annular region between the rotating cylinder and the stationary vessel wall, the Navier Stokes Equation is (Brodkey, 1967):

$$\frac{dP}{dz} = \mu \frac{d^2U_z}{dr^2} + \frac{1}{r}\frac{dU_z}{dr}$$

Integrating this equation twice yields:

$$\frac{r^3}{6}\frac{dP}{dz} = \mu \frac{r^3}{6}U_z + \frac{r^2}{2}U_z + Ar + B$$

where $r_i$ is the radius of the rotor, $r_o$ is the radius of the vessel and:

$$A = \frac{1}{6}\frac{dP}{dz}\left(\frac{r_i^3 - r_o^3}{r_i - r_o}\right) \qquad B = \frac{r_i}{6}\frac{dP}{dz}\left(r_i^2 - \frac{r_i^3 - r_o^3}{r_i - r_o}\right)$$

Which may be solved for $U_z$.

The out of plane velocity ($U_\theta$) is given by (Brodkey, 1967)

$$U_\theta = \frac{\omega}{r_i^2 - r_o^2}\left[rr_i^2 - \frac{r_i^2 r_o^2}{r}\right]$$

## NOMENCLATURE

| | |
|---|---|
| $\mathbf{a}$ | General unknown vector |
| $\mathbf{b}$ | Body force vector |
| $c$ | Reduced variable model boundary condition |
| $\mathbf{f}$ | General load vector |
| $\mathbf{F}$ | Body force vector |
| $\mathbf{K}$ | General stiffness or system matrix |
| $\mathbf{M}$ | General mass matrix |
| $n$ | Porosity |
| $\hat{n}$ | Reference porosity (this chapter only) |
| $\mathbf{N}$ | Shape function (vector) |
| $P$ | Pressure |
| $\mathbf{S}$ | Strain operator |
| $t$ | Time |
| $\mathbf{t}$ | Applied tractions |
| $\mathbf{u}$ | Displacement vector |
| $\mathbf{U}$ | Velocity vector |
| $\mathbf{V}$ | Mixture pseudo-velocity |
| $\mathbf{W}$ | Difference pseudo-velocity |

### Greek Symbols

| | |
|---|---|
| $\beta$ | Drag coefficient |
| $\delta$ | Denotes virtual quantity |
| $\varepsilon$ | Strain tensor |
| $\mu$ | Viscosity |
| $\Omega$ | Integration domain |
| $\psi$ | General unknown |
| $\rho$ | Density |
| $\boldsymbol{\sigma}$ | Stress tensor |

| | |
|---|---|
| $\theta$ | Inclination with respect to vertical |

**Subscripts**

| | |
|---|---|
| f | Fluid component |
| n | Porosity |
| P | Pressure |
| s | Granular component |
| U | Velocity |
| V | Mixture pseudo-velocity |
| W | Difference Pseudo-Velocity |

**Superscripts**

| | |
|---|---|
| - | Nodal quantity (except as given in eq. 4.20) |
| • | Time derivative |

## REFERENCES

Bathe, K.J.
*Finite Element Procedures*
Prentice Hall, New Jersey, 1996

Brodkey, Robert S.
*The Phenomena of Fluid Motions*
Dover, Mineola, NY, 1967

Fortin, M., Fortin, A.
*Newer and Newer Elements for Incompressible Flow (Gallagher, R.H., Carey, G.F., Oden, J.T., Zienkiewicz, O.C., eds.)*
Finite Elements in Fluids, Vol. 6, pp. 171 - 187

Hiltunen, K.
*A Stabilized Finite Element Method for Particulate Two-Phase Flow Equations, Laminar Isothermal Flow*
Comput. Meth. Appl. Mech. Engrg., Vol. 147, pp. 387-399, 1997

LeTalluc, P., Ruas, V.
*On the Convergence of the Bilinear-Velocity Constant-Pressure Finite Element Method in Viscous Flow*
Comp. Meth. In Appl. Mech. & Eng., Vol. 54, pp. 235 - 243, 1986

Lyczkowski, R.W., Gidaspow, D., Solbrig, C.W., Hughes, E.D.
*Characteristics and Stability Analyses of Transient, One-Dimensional, Two-Phase Flow Equations and their Finite Difference Approximations*
Nucl. Sci. & Eng., Vol. 66, pp. 378-396, 1978

Malvern, L.E.
*Introduction to the Mechanics of a Continuous Medium*
Prentice Hall, New Jesey, 1969

Masson, C., Baliga, B.R.
*A Control-Volume Finite Element Method for Dilute Gas-Solid Particle Flows*
Comp. Fluid., Vol. 23, pp. 1073-1096, 1994

Nigro, N., Storti, M., Idelsohn, S.
***Two-phase Flow Modelling in Gas-Stirred Liquid Vessels with SUPG-Stabilized Equal-Order Interpolations***
Int. J. Num. Meth. Fluids, Vol. 19, pp. 1 - 22, 1994

Oden, J.T.
***An Introduction to the Mathematical Theory of Finite Elements***
John Wiley & Sons, New York, 1976

Pastor, M., Tongchun, Li, Merodo, J.A.
***Stabilized Finite Element for Harmonic Soil Dynamics Problems Near the Undrained Compressible Limit***
Soil Dynamics and Earthquake Eng., Vol. 16, pp. 161 - 171, 1997

Zienkiewicz, O.C., Taylor, R.L.
***The Finite Element Method, 4th Edition***
Mc-Graw Hill, New York, 1989

# 5 MODEL VERIFICATION AND ANALYSES

The preceding chapters have presented the hydrodynamic model used, the additional models required for closure of the differential equations, and the finite element solution methods that are applicable to the class of problems addressed in this thesis. This chapter verifies the appropriateness of the models by comparing their predictions to the experimental and numerical results of others.

Five basic scenarios have been analyzed using the models developed in this study. The finite element results have been compared to experimental results published in the literature and they have been found to agree to a reasonable degree. The selection of experimental results was made to allow the verification of the models in stages of increasing complexity. In addition to verifying the model, some interesting conclusions have been drawn from the numerical results, which, in some cases, are able to provide a possible explanation for a phenomenon for which a mechanism had not been previously provided.

The first simulation analyzes the transient behavior of a two component mixture that is fluidized in a one-dimensional bed after being subjected to a step change in the fluid inlet velocity. Experimenters have noticed an asymmetry between step increases and step decreases in the flow rate. This phenomenon is captured by the numerical model. A mechanistic explanation of this asymmetry is also provided.

The second simulation tests the capability of the model to simulate the settlement of the solid particles from a state of fluidization to a packed bed configuration. This analysis employs the granular component stress model presented in the third chapter. The results compare favorably to experimental values over the entire duration of the settlement.

The third simulation adds a significant complexity associated with two-dimensional flows. The model is used to simulate the transition to fully developed flow of a two-component mixture in a pipe. The computed velocity vectors and porosity values compare favorably to the measured results.

The fourth simulation is of a one-dimensional column of loose sand that is "subjected" to the El Centro earthquake and the ensuing liquefaction and post liquefaction response is monitored. Owing to the lack of data on such an event, the present model is compared to previous numerical results. The simulations compare favourably, and the capacity to monitor post liquefaction response represents a significant improvement over previously developed models. The post-liquefaction consolidation and settlement is also simulated.

Finally, a flow analysis of the rotating cylinder viscometer discussed in Chapter 3 is presented. The results of this analysis are provided for demonstration only and no verification of the results are included. The analysis shows that the assumptions made in the experimental phase were warranted. An interesting comparison of the flow profile in the two-component mixture to single phase flow is also provided.

## 5.1 Transient Response of a Solid-Liquid Fluidized Bed to a Step Change in Fluid Inlet Velocity

Several researchers have reported both experimental and theoretical investigations of the transient response of a one-dimensional fluidized bed to step changes in the fluidization velocity. Owing to the thoroughness of the reported work, this scenario provides an excellent vehicle to verify some of the capabilities of the model developed in this study. Slis et al. (1958) provide a substantial body of experimental results for a variety of particle sizes, initial conditions and for both bed expansions and contractions. The results of the comparison between the numerical model and the experimental findings are presented in the following sections.

### 5.1.1 Comparison of Finite Element Simulations to Experimental Results

The drag relation used by Slis et al. (1958) differs substantially in form from that used in the current numerical model, however the results of the following simulations demonstrate that the experimentally determined behavior is in fact reproduced by the model. Figures 5.1 and 5.2 show typical predicted porosity distributions through the bed at several time increments. It may be observed that the distribution compares favorably with that described in Slis et al. (1958). Table 5.1 gives the material properties of the solid component. Ordinary tap water was used as the fluidizing liquid.

**Table 5.1:** Material Properties of Solid Component

| **Material** | | **Particle Diameter (mm)** | **Particle Density (kg/m$^3$)** |
|---|---|---|---|
| I | nylon | 3 | 1140 |
| II | nylon | 4 | 1140 |
| III | nylon | 5 | 1140 |

The numerical model was started assuming an initial uniform porosity distribution (table 5.2) over the entire height (0.275 m) of the fluidization column. The inlet velocity of the fluid was then changed to a new value and the transient behavior was observed.

Figure 5.1 shows the porosity distribution profile through the fluidized bed at four different times in the analysis. The important feature in this plot is the decreasing slope of the interface between the original porosity and the final one. This decreasing slope shows that this interface is widening as the disturbance propagates upwards which is exactly what Slis et al. (1958) both predicted and found experimentally. The oscillations about $n = 0.75$, evident in Figure 5.1, are a function of the hydrodynamic model as discussed in Chapter 4.

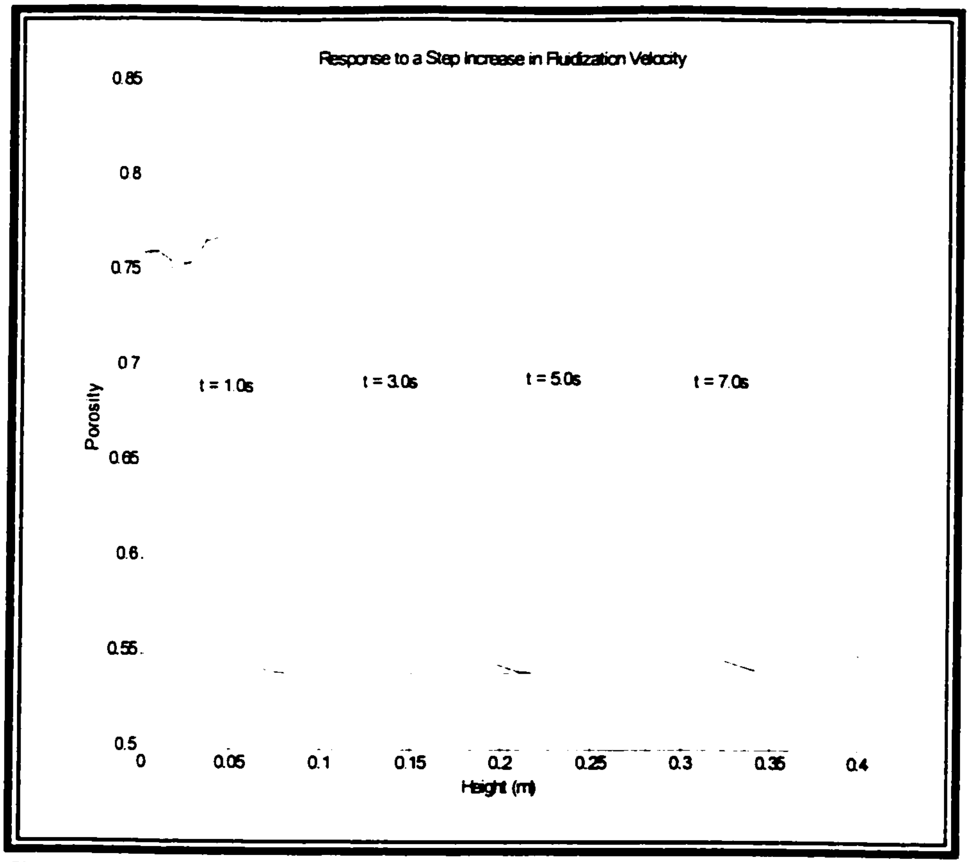

**Figure 5.1:** Typical response to a step increase in fluidization velocity

Slis et al. (1958), performed several experiments on the transient response of fluidized beds to both step increases and step decreases in the flow of the fluidizing liquid. Water was used as the fluidizing liquid and nylon spheres was the granular solid. Unfortunately, the mean particle size (with no definition of "mean") and particle density were the only parameters available on the granular materials. Information on the roundness and distribution of particle size would have been helpful information for explaining discrepancies between the experimental and numerical results.

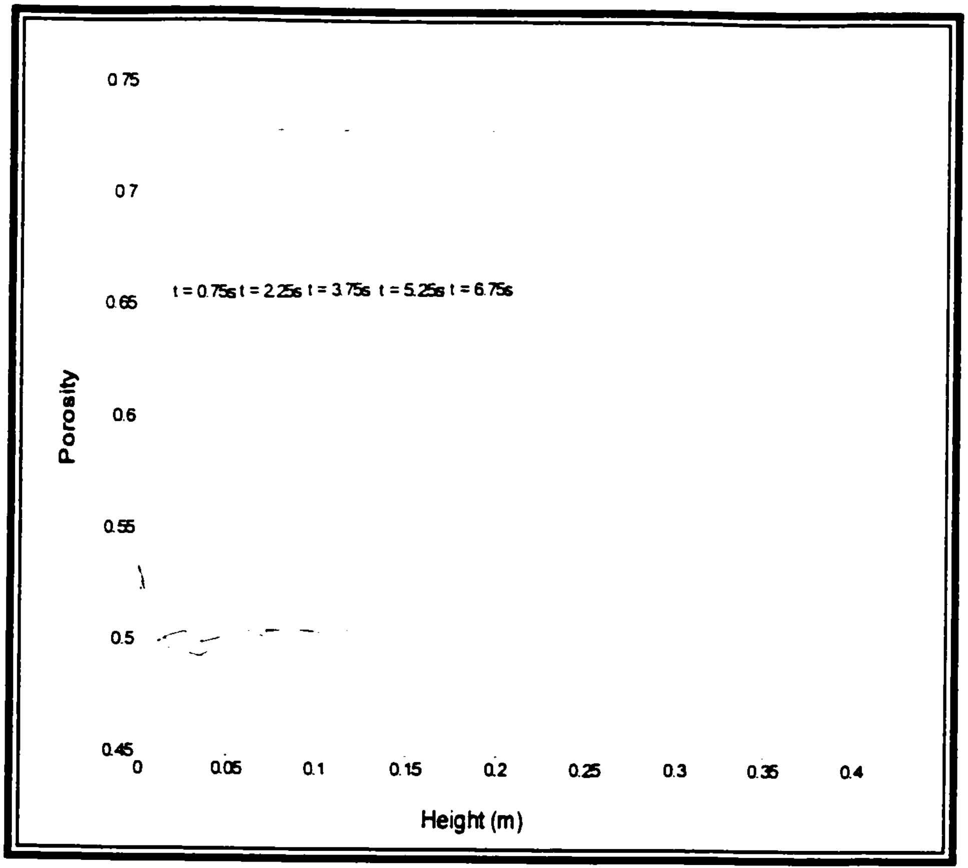

**Figure 5.2:** Typical response to a step decrease in fluidization velocity

The given parameters were programmed into the model and the simulations were performed for a variety of the test conditions measured by Slis et al. (1958). Table 5.2 compares the time to reach a new steady state ($t_1$) following a step change in the fluidizing velocity. It may be observed that the results, while not perfect, provide good engineering approximations of the observed results. It should be noted that these results were obtained by providing nothing more than the mean particle diameter and density. One would expect that, had more information been available, the drag model could have been improved and the resulting simulations would have been more accurate. It may be noted that the results are generally better when the final porosity is relatively high. This is due to the fact that the drag model predictions are closer to the experimentally measured values given in Slis et al. (1958) at higher porosities than at the lower ones.

Owing to the ability of the numerical model to capture the essential elements of this one-dimensional fluidization problem (including the asymmetric response) with reasonable engineering accuracy given a minimum of information on the components in the flow, it may be concluded that the model provides a reasonable description of two component flow for medium to high porosity levels.

**Table 5.2**: Experimental vs. Finite Element Results for Fluiziding Velocity Step Change

| Material | Initial Porosity | Final Porosity | $t_f$(exp) (s) | $t_f$(FEA) (s) | % Difference |
|---|---|---|---|---|---|
| I | 0.54 | 0.76 | 15 | 13.8 | 8.7 |
| I | 0.68 | 0.80 | 19 | 18 | 5.3 |
| II | 0.53 | 0.83 | 17 | 16 | 5.9 |
| II | 0.62 | 0.73 | 9 | 7.2 | 20.0 |
| III | 0.66 | 0.85 | 18 | 15 | 16.7 |
| III | 0.72 | 0.78 | 10 | 11 | 10.0 |
| I | 0.63 | 0.54 | 9.3 | 5.6 | 39.7 |
| I | 0.73 | 0.53 | 10 | 7.4 | 26.0 |
| II | 0.70 | 0.61 | 6.8 | 4.9 | 27.9 |
| II | 0.67 | 0.57 | 6.0 | 4.3 | 28.3 |
| III | 0.69 | 0.64 | 5.2 | 4.0 | 23.1 |
| III | 0.80 | 0.73 | 11 | 7.3 | 33.6 |

### 5.1.2 Qualitative Behavior to Increased and Decreased Fluidization Velocity

It is well established in the literature that there are important similarities and differences in the response of a fluidized bed to step increases and step decreases in the fluidization velocity; see for example, Slis et al. (1958), Thelen and Ramirez (1999). When a fluidized bed is subjected to a step ***increase*** in the fluidization velocity, the porosity of the bed near the inlet changes rapidly from an initial porosity ($n_o$) to a new steady state value ($n_f$), which creates an interface between the initial and final porosities. This interface propagates upwards through the bed until the entire bed is at the final state. Owing to the qualities of the drag/porosity relationship, this interface becomes gradually larger as it propagates upwards. In other words, the interface is not as well defined at later stages of the propagation.

The response of the fluidized bed to a step ***decrease*** in fluidization velocity is similar in that an interface between the initial and final states begins at the inlet and propagates upwards. However, due to the nature of the drag/porosity relationship, this interface begins and remains sharp as it propagates upwards. Figures 5.1 and 5.2 illustrate these features.

The differences in behavior have been explained by Slis et al. (1958), paraphrased below, to which the reader is referred for greater detail. The relationship between fluidization ($U_l$) velocity and porosity for a steady (no movement of particles) fluidized bed can be expressed by:

$$U_l = U_l' n^k \tag{5.1}$$

where $U_l'$ and k are parameters of individual particle/fluid combinations. The relationship of equation 5.1 differs substantially from the drag law relationship of the hydrodynamic model in that, equation 5.1 is a simple correlation of experimental data whereas the drag model presented in Chapter 3 is a mechanistic model. However, there is an important similarity between the two models in the power relation between fluidization velocity and porosity. Owing to this similarity, it is possible to use equation 5.1 to explain the overall qualitative behavior. A similar, but much more complex, explanation may be made using the drag model of Chapter 3. The results of the simulations show that this is indeed the case.

The continuity equation for the granular component yields:

$$\frac{\partial(1-n)u}{\partial x} + \frac{\partial(1-n)}{\partial t} = 0 \tag{5.2}$$

where u is the velocity of the granular component. Defining the actual fluid velocity as:

$$u_f = \frac{U_l}{n} \tag{5.3}$$

where $U_l$ is the superficial fluid velocity. It may be stated that:

$$u_f - u = U_l' n^{k-1} \tag{5.4}$$

Now, if the inlet flow is increased to $U_l^{\triangleright t_0}$, then the equation of overall continuity requires that:

$$n u_f + (1-n)u = U_l^{\triangleright t_0} \tag{5.5}$$

Combining equations 5.4 and 5.5 yields:

$$U_l^{\triangleright t_0} - u = U_l' n^k \tag{5.6}$$

If eq. 5.6 is substituted into eq. 5.2, the resulting partial differential equation is:

$$\left(\left[k n^{k-1} - (k+1)n^k\right]U_l' + U_l^{\triangleright t_0}\right)\frac{\partial n}{\partial x} + \frac{\partial n}{\partial t} = 0 \tag{5.7}$$

Equation 5.7 reveals that a disturbance δn travels with a velocity w equal to the bracketed expression (Slis et al., 1958):

$$w = \left[kn^{k-1} - (k+1)n^{k}\right]U_l' + U_l^{>t_0} \tag{5.8}$$

This means that the disturbance propagation velocity increases as n decreases. The ramification of this is that, if $n_1 > n_0$, the interface between the two regions will grow as it travels upward since the leading edge of the disturbance is at a lower porosity (and hence this leading edge travels faster than the trailing edge). Conversely, if $n_1 < n_0$, the discontinuity will remain sharp as the trailing edge always keeps pace with the leading edge.

The above explanation for the asymmetric behavior was given by Slis et al. (1958) and it has been, in essence, re-transcribed here for the benefit of the reader. For more details, the reader is referred to the original source.

### 5.1.3 Parameter Sensitivity

An important consideration of any modeling effort is the sensitivity of the results to changes in the parameters. If a model is overly sensitive to the parameters, the model will likely provide erroneous results when no validation data are available.

In order to determine the effect of the parameters (see Table 5.3) on the solution, the time to reach steady state (i.e., t1) for the first case presented in Table 5.2 is compared against the original solution for small changes (10% increase) in parameters. The results are given in Table 5.3.

Table 5.3: Effect of Changes in Numerical Model Parameters

| Parameter | Original Value | 10% Increase | t1 | % Change |
|---|---|---|---|---|
| Original Result | - | - | 13.8 | - |
| Particle Diameter | 3 mm | 3.3 mm | 13.0 | -5.8 |
| Time Step | 0.01 s | 0.011 s | 13.9 | <0.1 |
| Element Size | 9 mm | 9.9 mm | 14.0 | 1.1 |

It may be observed from these results that simulations are quite insensitive to changes in the parameter values.

## 5.2 Transient Response with Settling

In the previous model verification example, the granular component was held in suspension in the fluid component. That is, little or no interaction was assumed to occur between individual granules. However, this interaction cannot be ignored in the case where the particles settle out of suspension. In this, section, the capability of the numerical model, with the addition of the granular component spherical stress model, will be verified against experimental results for a two component mixture settling out of suspension. As in the previous section, a comparison between the finite element and experimental results is first presented followed by a brief theoretical explanation of the qualitative behavior.

### 5.2.1 Comparison of Finite Element Simulations to Experimental Results

Shih et al. (1986) present experimental results for the settling of fine illite particles (a clay-like material) in toluene. This experiment was simulated with the current model. The parameters provided by Shih et al. for the model were the effective particle diameter, particle density, fluid viscosity, fluid density and the initial concentration of solid particles. Estimates of the solids pressure model parameters, A and ñ were also provided. Table 5.4 lists these parameters. It should be noted that clay particles are plate-like and not spherical. Thus, one should expect some deviation of predictions from experimental results.

Using the particle diameter of 62.5 µm as given in the paper resulted in settling rates much higher than those observed experimentally. This can be explained by the fact that illite, being a clay-like material, has plate shaped particles rather than spheroids. Gidaspow (1994) provides an improvement to the drag model for cases such as this, where the particles differ from a spherical shape.

The particle diameter as found in the drag model is replaced by a corrected diameter, ie.:

$$d_p' = \varphi d_p \tag{5.9}$$

where φ is the sphericity of the particle. For these experimental results, φ=0.088 provided excellent results.

Table 5.4: Settling Model Parameters

| Parameter | Value |
|---|---|
| Particle Diameter | 62.5 μm |
| Sphericity | 0.088 |
| Particle Density | 2460 kg/m$^3$ |
| Fluid Viscosity | 0.586 c.p. |
| Fluid Density | 870 kg/m$^3$ |
| A | 0.1075 |
| $\bar{n}$ | 0.95 |
| Element Length | 6.25 mm |
| Time Step | 0.1 s |

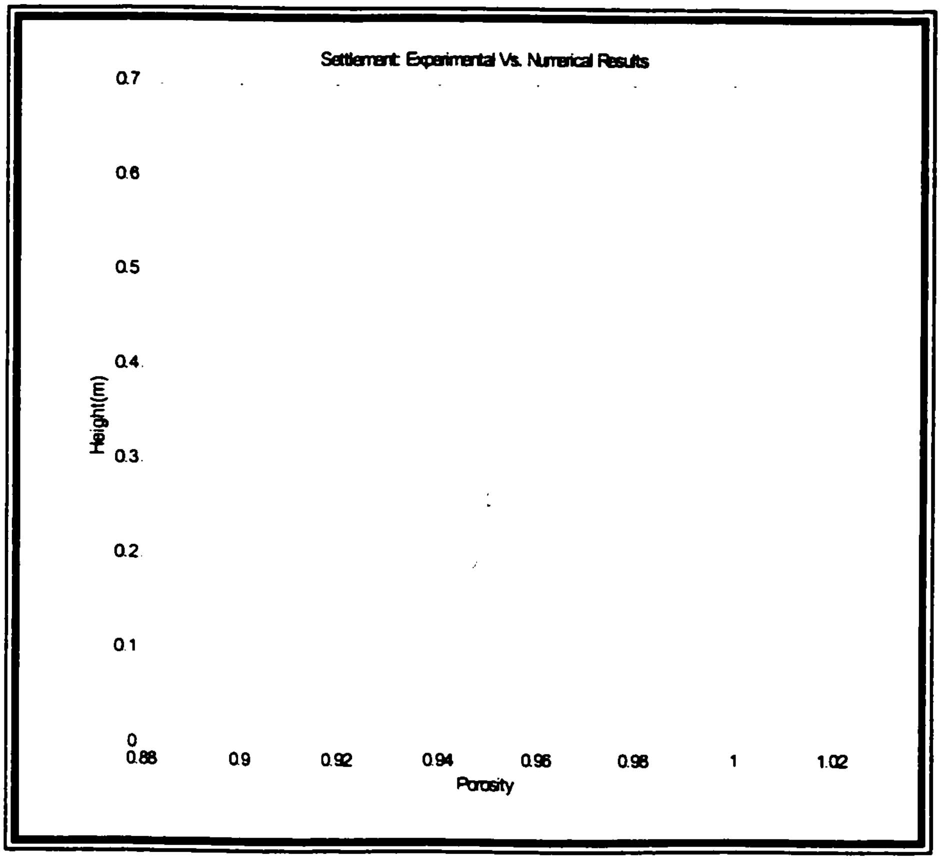

Figure 5.3: Comparison of experimental and numerical results (t=90s)

Figures 5.3 through 5.5 show plots of the porosity distribution in the column at three different times for both the numerical model (solid line) and experimental results (open circles). Table 5.5 lists the average error in the porosity prediction at three times during settlement. The error was calculated from the difference between the experimental and numerical values at each of the three times and dividing by the range of experimental determined porosities (in this case approximately 1.0-0.87 = 0.13). Average error was chosen over maximum error as the overall behavior is of primary

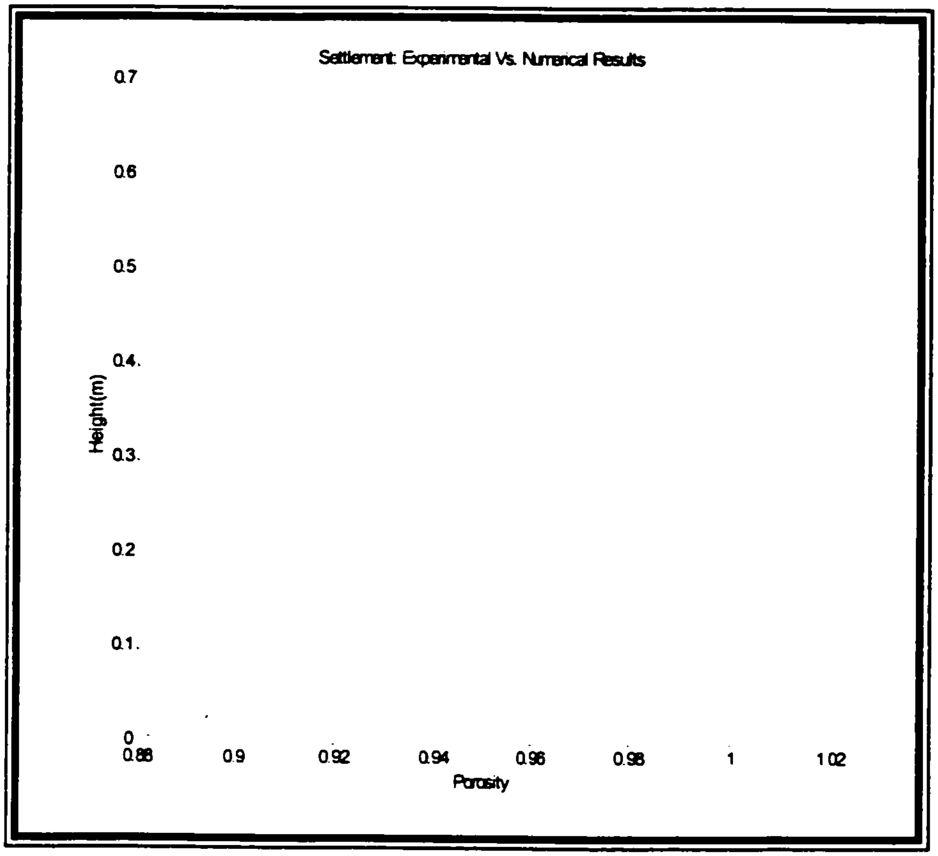

**Figure 5.4:** Comparison of experimental and numerical results (t=180s)

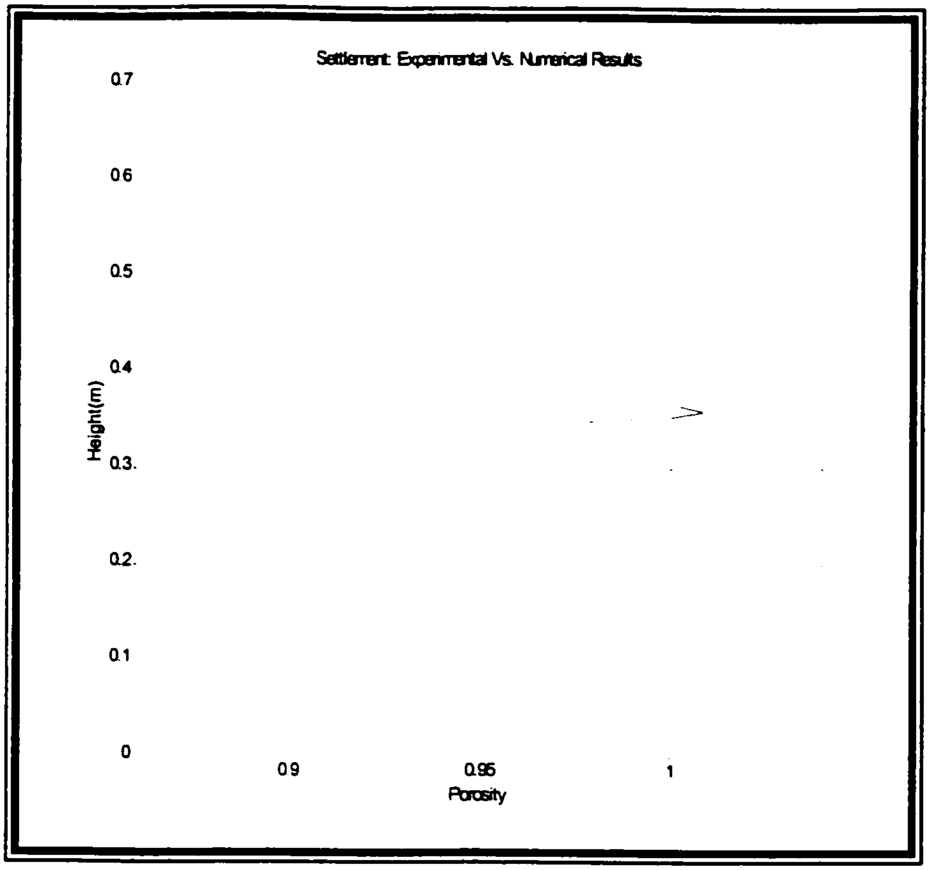

**Figure 5.5**: Comparison of experimental and numerical results (t=300s)

interest. One observes that the current model predictions agree well with the experimental results. Such agreement lends support for the appropriateness of the model for simulating settlement scenarios.

**Table 5.5**: Error in Settling Results

| Time (s) | Average Error |
|---|---|
| 90 | 12.4% |
| 180 | 8.0% |
| 300 | 17.2% |

### 5.2.2 Qualitative Behavior of Settling

According to Gidaspow (1994), the particle mass balance (assuming incompressibility of both components) is

$$\frac{\partial(1-n)}{\partial t} + v\frac{\partial(1-n)}{\partial x} = 0 \tag{5.10}$$

where $v$ is the settling velocity of the particles. If one assumes that the particles reach the settling velocity instantaneously, equation 5.9 is equivalent to

$$\frac{d(1-n)}{dt} = 0 \tag{5.11}$$

along the path

$$\frac{dx}{dt} = v \tag{5.12}$$

Equations 5.10 and 5.11 reveal that during settling, there exists a zone in which the porosity remains constant, at its initial value. The simulations presented in the preceding section confirm this trait (see Figures 5.3 and 5.4).

### 5.2.3 Parameter Sensitivity

To improve the confidence in the numerical results, the sensitivity to variability in the model parameters must be determined. To this end, simulations were performed for the first ninety seconds of settling and the average error was calculated for ten percent increases to each of the parameters listed in Table 5.4 (except for $\bar{n}$ since an increase of ten percent would make this value greater than unity, an impossibility). The results of this analysis are given in Table 5.6, which lists the change in error at t=90s resulting from a change in a parameter. It can be seen that in all cases, an increase of a parameter by ten percent causes only small change in the error. In fact, in some cases, the error at t=90s was significantly reduced. Such insensitivity to changes in model parameters is important as it gives confidence that the good agreement is not a result of a contrived combination of parameters. The reader should further note that two numerical parameters, element length and time step, did not change the solution significantly. It is therefore expected, the chosen element length and time step do not require further refinement.

**Table 5.6:** Sensitivity Analysis of Model Parameters (t=90s)

| **Parameter** | **Increased Value** | **Average Error with Increased Parameter Value** | **Change in Average Error due to Increase in Parameter Value** |
|---|---|---|---|
| Particle Diameter | 68.75 μm | 5.5% | -6.9% |
| Sphericity | 0.0968 | 5.5% | -6.9% |
| Particle Density | 2706 $kg/m^3$ | 5.7% | -6.7% |
| Fluid Viscosity | 0.645 c.p. | 13.0% | 0.6% |
| Fluid Density | 957 $kg/m^3$ | 12.8% | 0.4% |
| A | 0.1183 | 13.3% | 0.9% |
| $\bar{n}$ | 0.9665 | 14.6% | 2.2% |
| Element Length | 6.875 mm | 12.5% | 0.1% |
| Time Step | 0.11 s | 12.4% | 0% |

## 5.3 Steady Two-Dimensional Pipe Flow

The first two validation results were for one-dimensional flow. In many practical situations, the one-dimensional model is adequate. However, there are many other cases where the flow is truly two-dimensional or axi-symmetric and hence a two-dimensional model is required. Clearly, it is much more difficult to determine flow velocities and porosity distributions experimentally in a two-dimensional domain. Furthermore, many experimental flows, which may seem superficially two-dimensional, are in fact three-dimensional due to the effects of end walls. Owing to these problems, suitable experimental results against which the numerical model may be verified are few in number. An article by Liang and Zhu (1997) on the flow structure of a liquid-solid (tap water/glass-beads) mixture on a pipe has been selected for comparison purposes as it provides experimental results for two-dimensional, axi-symmetric conditions.

As in the previous examples, the information required for the model are the granular component particle diameter and density as well as the fluid component density and viscosity. The fluid component in this case is tap water and the solid component is glass beads. Table 5.7 lists the parameters used in this analysis. Figure 5.6 shows the boundary conditions for the simulation.

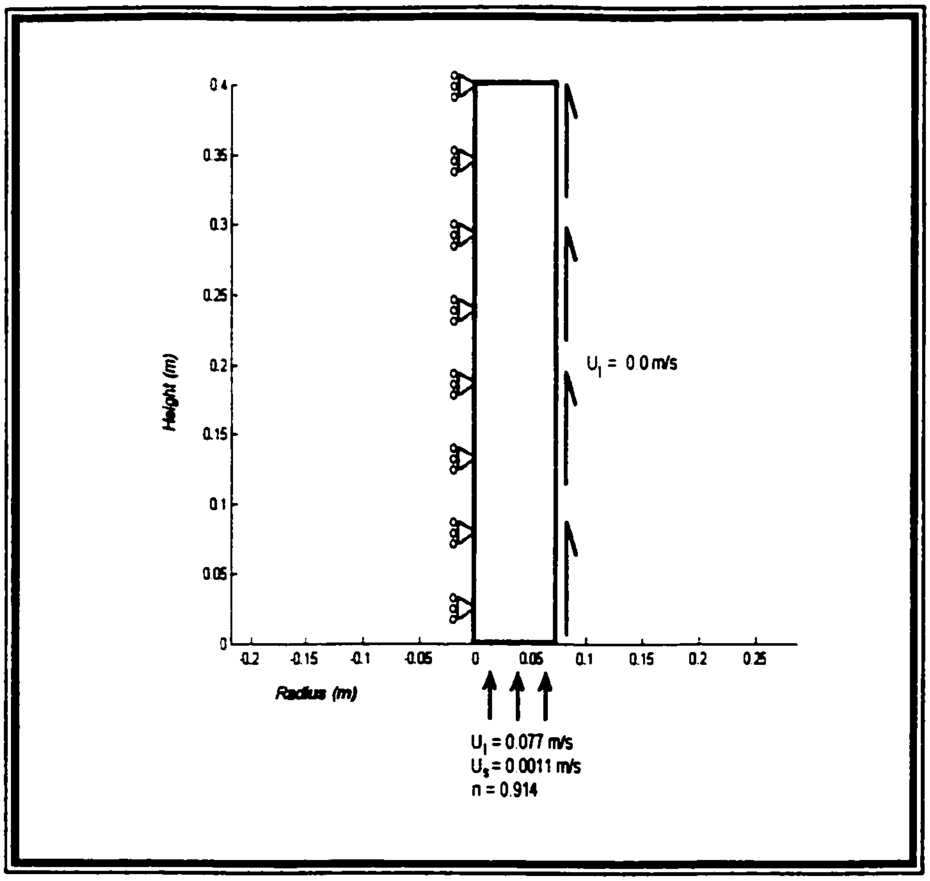

**Figure 5.6**: Finite Element Mesh (100 vertical X 50 horizontal elements) and Boundary Conditions

**Table 5.7**: Two Dimensional Model Parameters

| **Parameter** | **Value** |
|---|---|
| Particle Diameter | 403 μm |
| Particle Density | 2460 kg/m$^3$ |
| Fluid Viscosity | 1.75 cp |
| Fluid Density | 1000 kg/m$^3$ |

A transient analysis was carried out until steady state, fully developed conditions were reached. The resulting distributions of liquid velocity and porosity at a fully developed elevation were compared to the experimentally determined values. These comparisons are plotted in figures 5.7 and 5.8.

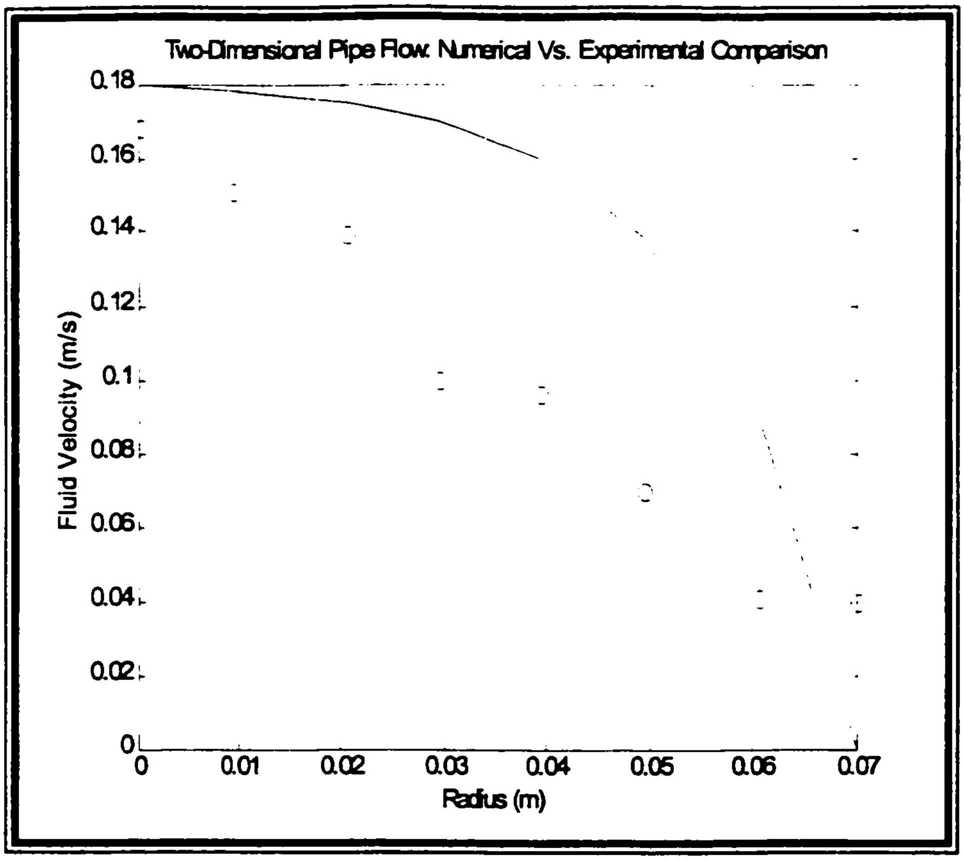

**Figure 5.7:** Comparison of numerical and experimental radial plane fluid velocity distribution results

These figures show that the numerical results (solid line) follow the general trends provided by the experimental results with good agreement for the porosity distribution. Table 5.8 lists the error in the numerical fluid velocity and porosity profiles as compared to the experimental results. Once again, support has been given for the appropriateness of the numerical model for the simulation of two-dimensional flows of granular solid/liquid mixtures.

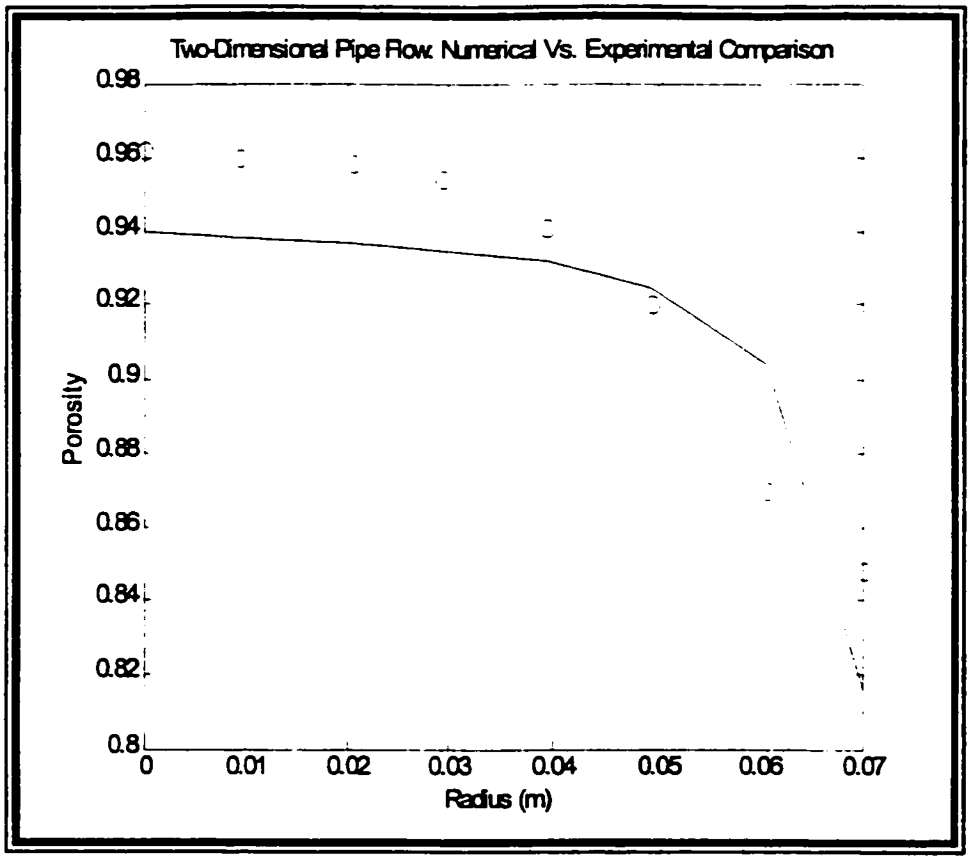

**Figure 5.8:** Comparison of numerical and experimental radial plane porosity distribution results

**Table 5.8: Two-Dimensional Flow Analysis Error**

| Variable | Average Error |
|---|---|
| Fluid Velocity | 37.3% |
| Porosity | 5.5% |

The error in porosity was calculated as described in section 5.2.1. It may be seen that there is both good qualitative and quantitative agreement between the experimental and simulated porosity distributions. However, there is considerable error in the fluid velocity profile. An approximate integration of the velocity profile reported in Liang and Zhu (1997), reveals that the volume flow rate is substantially different than the reported inlet flow rate. Therefore, the differences between the finite element simulation and the reported results may be attributable not only to errors in the numerical results but to errors in the reported data.

### 5.3.1 Parameter Sensitivity

Once again, to improve our confidence in the results of the finite element analysis, the sensitivity of the results to changes in the parameters was assessed. Since the effects of material properties on the results have been established in the previous sections and because reliable measurements of the properties can be made, the sensitivity analysis of this case focuses on the finite element mesh and on the boundary conditions. Table 5.9 lists the effect on both the fluid velocity and porosity errors of increases of ten percent of specific model parameters from the values listed in Table 5.8.

**Table 5.9:** Sensitivity Analysis of Model Parameters

| Parameter | Parameter Value after 10% Increase | Change in Average Fluid Velocity Error | Change in Average Porosity Error |
|---|---|---|---|
| Element Size | 2.2 mm | 0.1% | 1.3% |
| Inlet Fluid Velocity | 0.0847 m/s | 5.1% | -1.4% |

It may be observed that again, increases of ten percent in these parameters results in a less than ten percent change in the error. As with previous analyses, the effect of the mesh size was minor. Since the results are for steady state, the time step has no effect on the results.

## 5.4 Liquefaction of One-Dimensional Sandy Soils Under Earthquake Loading

The following analysis demonstrates the objective of the thesis, that of modeling the liquefaction of soils under the influence of earthquake loading. The mechanism of liquefaction was considered in the introductory chapter. This type of analysis makes use of all the components of the model including:

- Granular component spherical stress
- Neural network model of changes in the reference porosity
- Fluidization
- Settlement

While this is a one dimensional problem, with depth being the only co-ordinate system required, there is motion in both the horizontal and vertical directions. Therefore, the one-dimensional element must be supplemented by an additional equilibrium equation for the granular component (ignoring the effect of the fluid component in the horizontal direction):

$$\frac{\partial \sigma_{s_{xy}}}{\partial y} = \rho_s \dot{V}_{s_x} \tag{5.13}$$

It is assumed that the shear stress in the fluid is negligible compared to that in the granular component. The additional equation enables the horizontal velocity of the soil deposit to be calculated via the finite element method in a manner identical to that outlined in Chapter 4. The reader is referred to Pietruszczak and Stolle (1987) for greater detail. Unfortunately, there is little or no field data with which to compare the numerical results. Instead, it will be shown that the results compare favorably, in a qualitative sense, with another numerical simulation provided in Pietruszczak and Stolle (1987).

Figure 5.9 shows the soil deposit under consideration and lists the parameters of the model. The soil deposit was "constructed" by allowing solid particles to settle out of suspension. The soil modeled is that tested by the VELCAS program as described in Chapter 3. The N-S El Centro strong motion record was used as the simulated earthquake. The motion was scaled to a maximum of 0.1g acceleration to be consistent with the Pietruszczak and Stolle (1987) study. Figure 5.10 shows the power spectrum of the ground motion. Most of the significant motion occurs in the region of 2 Hz with smaller peaks near 4 and 6 Hz.

The reader should note that Pietruszczak and Stolle's model is fundamentally different from the current model of the soil behavior. Their model treats the soil as a solid and uses a Lagrangian framework to describe equilibrium. Therefore, one should expect that the results from each model will differ quantitatively and in some respects qualitatively. However, it is shown, that there are key similarities in the qualitative behavior.

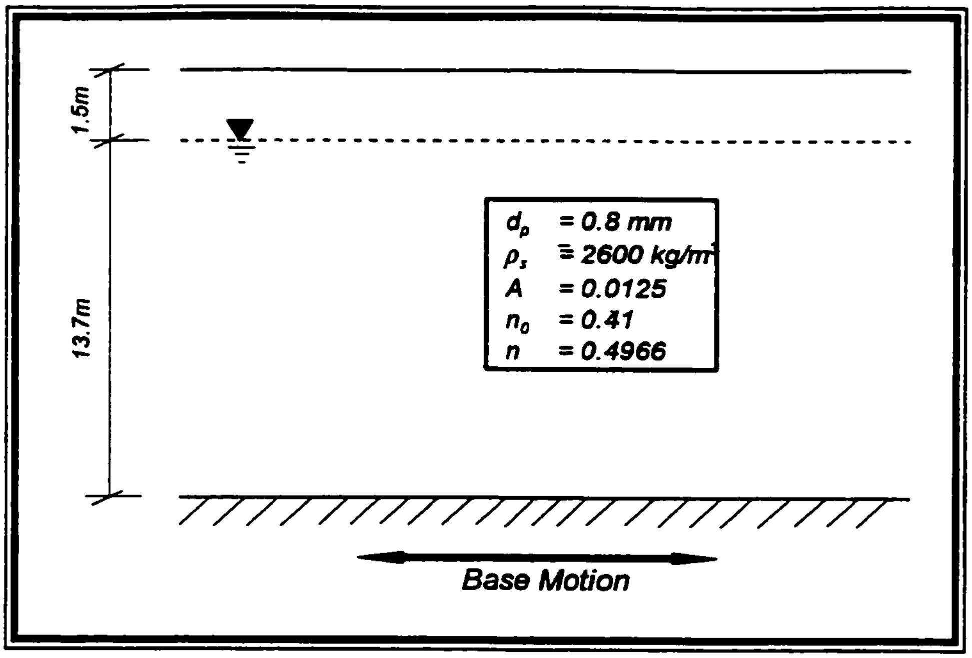

Figure 5.9: Dimensions of Soil Deposit

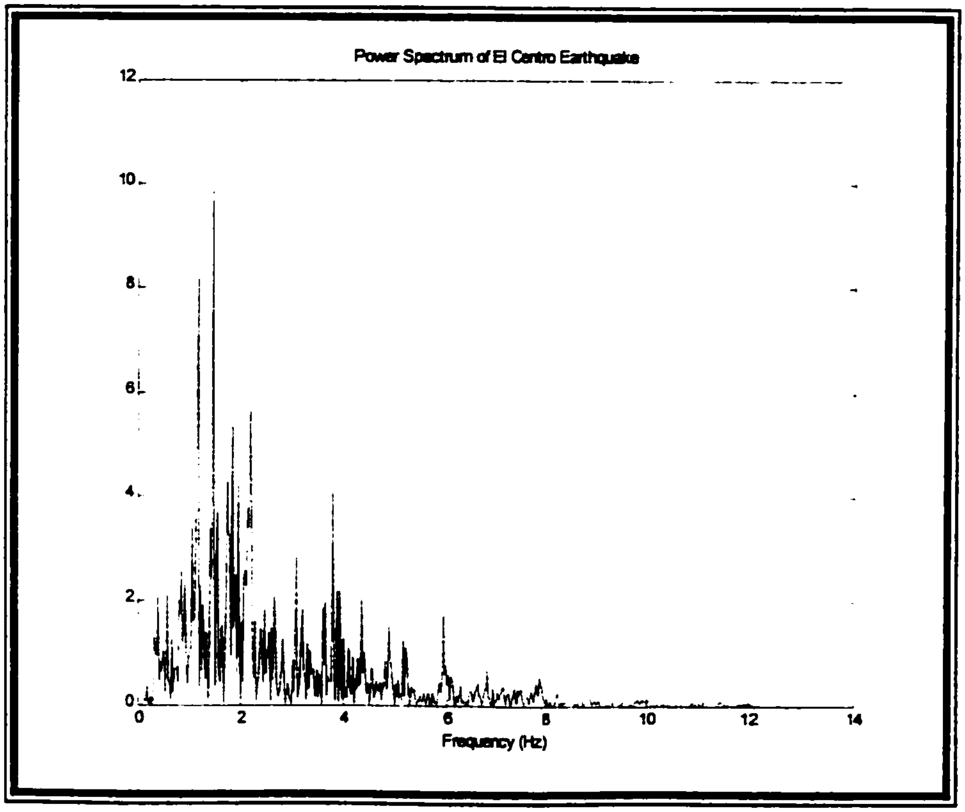

Figure 5.10: Power Spectrum of N-S El Centro (May, 1940) Ground Motion

Figure 5.11 shows the results of Pietruszczak and Stolle (1987) for a soil permeability of k=$10^{-6}$ m/s. Although the current model has no direct provision for a permeability value (rather, the permeability is a consequence of the drag model), the particle diameter was set to give a similar permeability. This is an important advantage of the proposed model when compared with more traditional methods since it accommodates the effect of porosity changes on the evolution of hydraulic conductivity during the liquefaction and post-liquefaction event.

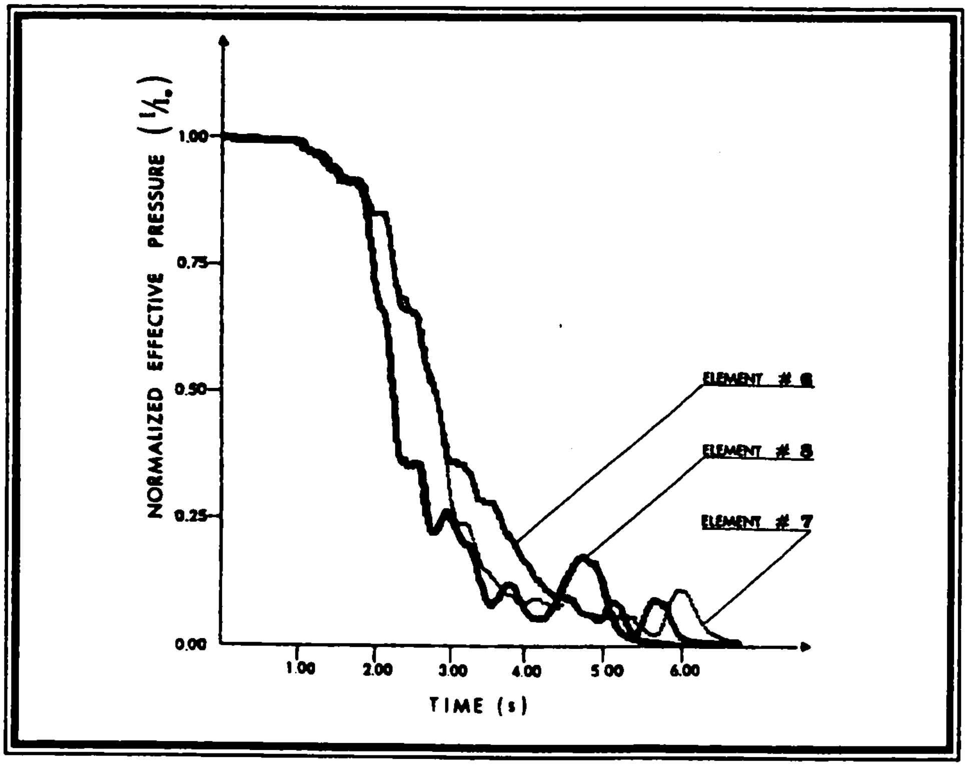

Figure 5.11: Liquefaction of a Soil Deposit (Pietruszczak and Stolle (1987)

The results of a simulation using the current model is presented in Figures 5.12 and 5.13. The effective vertical stress plotted in Figure 5.12 was normalized by the effective vertical stress at time zero. It may be

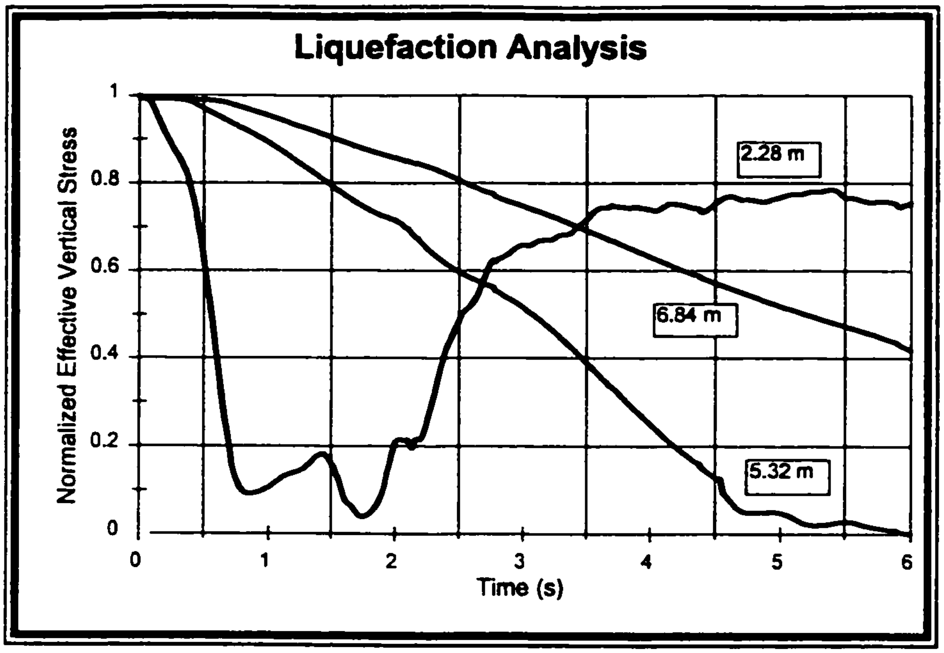

**Figure 5.12:** Results of Liquefaction Analysis Using Current Model ($d_p$=0.8mm)

observed, when comparing the results of the current study to that of Figure 5.11, that significant differences are present. For instance, in Figure 5.12, the plot of normalized effective vertical stress at a depth of 2.28m (corresponding to Pietruszczak and Stolle (1987) element #9) shows that for the soil considered in the present study, liquefaction nearly occurs at around 1.8 seconds. The sand modeled by the artificial neural network tended to experience rapid drops in $\bar{n}$, which explains the sudden liquefaction at a depth of 2.28m. However, because of it's proximity to the surface, the excess pore pressure quickly dissipates to the surface. This is in contrast with Pietruszczak and Stolle (1987) which does not exhibit this build up of pore pressure at a shallow depth. The reader should note however, that differences between the two results were not a surprise. These differences stem from at least three potential sources; (i) two different sands are being modeled; (ii) in Pietruszczak and Stolle's model the shear modulus of the soil is constant whereas in the current model it changes; (iii) the permeability of the soil deposit evolves over time in the current model but is constant in the Pietruszczak and Stolle model.

An important similarity exists however between the two models in that both predict the onset of liquefaction at an intermediate depth. It may be observed in Figures 5.11 and 5.12 that liquefaction is predicted at a depth of 5.32 m before it occurs at either deeper or more shallow depths. A significant benefit of the current model however, is that the analysis may continue, after the onset of liquefaction, to observe the growth and propagation of liquefaction zones (refer to Figure 5.13). With the other, more traditional analysis approaches, the simulations are typically terminated upon the onset of liquefaction.

Additional analyses were performed using different particle diameters for the granular phase, $d_p$=0.08 mm and $d_p$=8mm, which represent a very fine sand and a fine gravel. The resulting pore pressure and total vertical stress are given in Figures 5.14 and 5.15. It may be seen that, as expected; (i) the fine sand produces a more extensive liquefaction zone because of it's low permeability, whereas the gravel deposit is not able to liquefy at all; (ii) owing to its proximity to drainage, the surface does not liquefy.

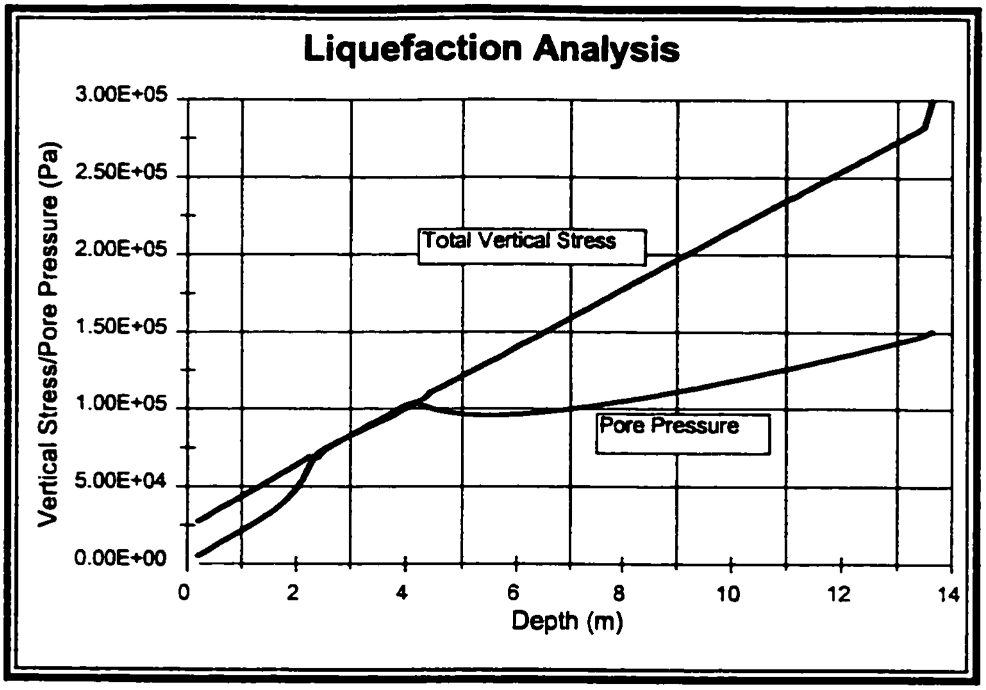

Figure 5.13: Zone of Liquefaction at 6s ($d_p$=0.8mm)

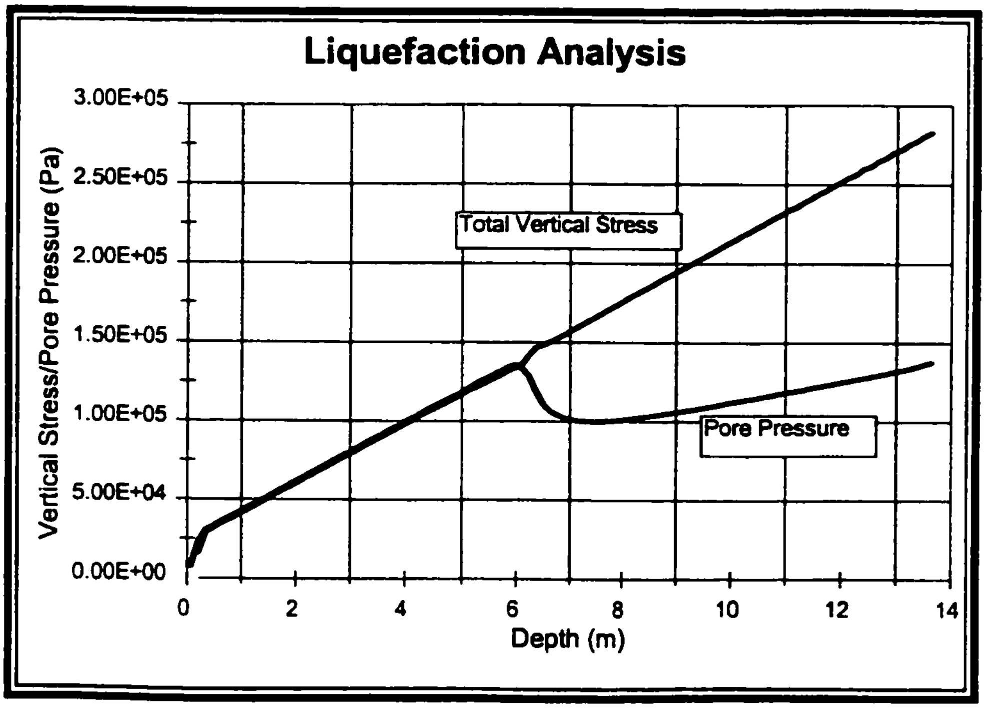

Figure 5.14: Zone of Liquefaction at 6s ($d_p$=0.08mm)

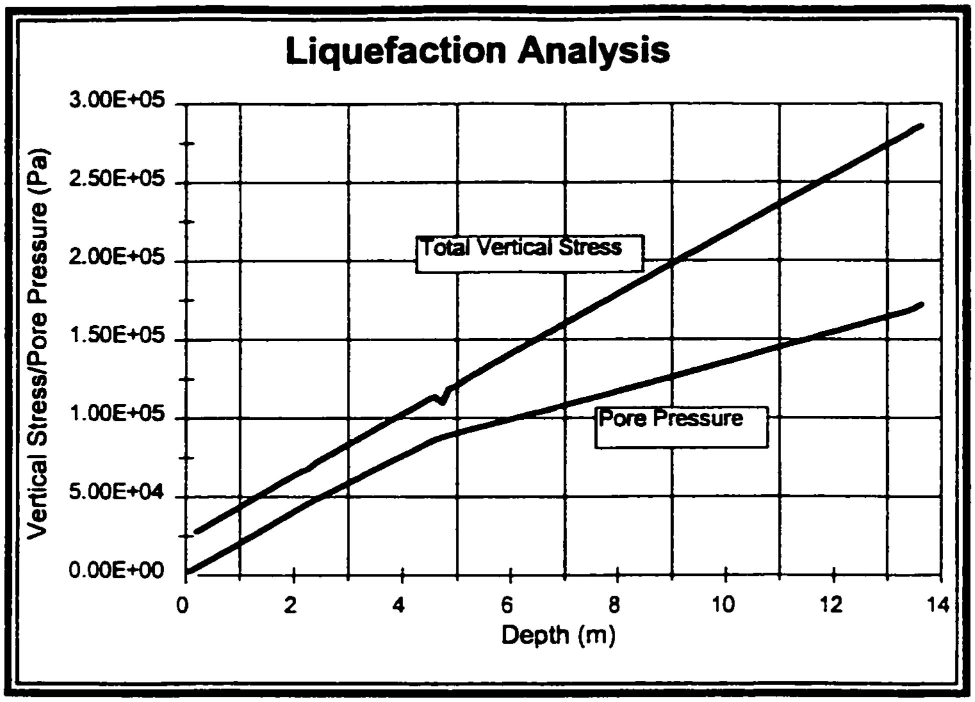

**Figure 5.15:** Zone of Liquefaction for Gravel at 6s ($d_p$=8.0mm)

It may be observed that there are several qualitative similarities between the current study and the results of Pietruszczak and Stolle (1987) such as:

- Similar time to initial liquefaction
- Isolated zone of liquefaction for $d_p$=0.8mm
- Expanded zone of liquefaction for smaller particle diameter

These similarities are largely qualitative, given that the sand for each constitutive model was different. Despite the differences that exist between the two results, it has been shown that the simple constitutive model used in this thesis is suitable for modeling liquefaction in a soil deposit. The reader should further note that the constitutive model of the current analysis was calibrated against experimental data whereas the Pietruszczak and Stolle model did not; owing to the focus on conceptual development in that study.

## 5.5 Re-consolidation and Settlement

One significant advantage of the current model over more traditional techniques is the ability to capture post-liquefaction phenomenon. One such phenomenon is the re-consolidation and settlement of the soil following liquefaction. After an earthquake has ceased motion, excess pore pressures in the soil deposit will gradually dissipate. As the pore pressure returns to hydrostatic equilibrium, vertical stress is transferred from the pore fluid to the granular soil. This, as discussed previously will cause the granular structure to compress, which in turn results in settlement of the soil surface below its original level.

As a demonstration of this phenomenon, consider the soil deposit modeled in Section 5.4. The simulated earthquake shakes this deposit for the first six seconds of the analysis. At this point, there is localized liquefaction (see Figure 5.13). For the remainder of the analysis, the excess pore pressure dissipates as the soil deposit consolidates, resulting in the settlement of the soil nearly 40 cm below it's original height. This represents a settlement of approximately 3% of the original deposit depth.

The pore fluid pressure profile at the base of the soil deposit is plotted in Figure 5.16. It may be observed that the pressure here peaks shortly after the end of the earthquake. This may be attributed to the continued shaking in the deposit after the earthquake has ended. Once this shaking dies out, the pore pressure begins to dissipate and the settlement takes place more gradually due to consolidation.

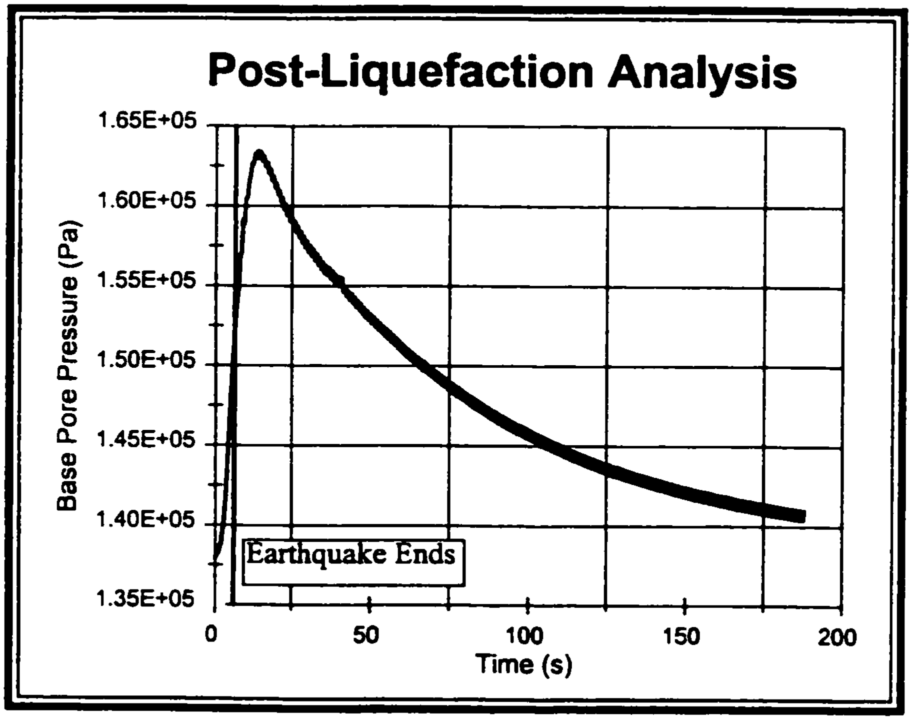

Figure 5.16: Base Pore Pressure Profile

Finally, Figure 5.17 shows the surface settlement as a function of time. It may be observed that a little more than half of the total settlement occurs during the earthquake with the remainder taking place thereafter. It should be noted that the analysis was stopped 3 minutes after the initiation of ground excitation. It may be observed in Figure 5.16 that there is still a small amount of excess pore pressure at the base.

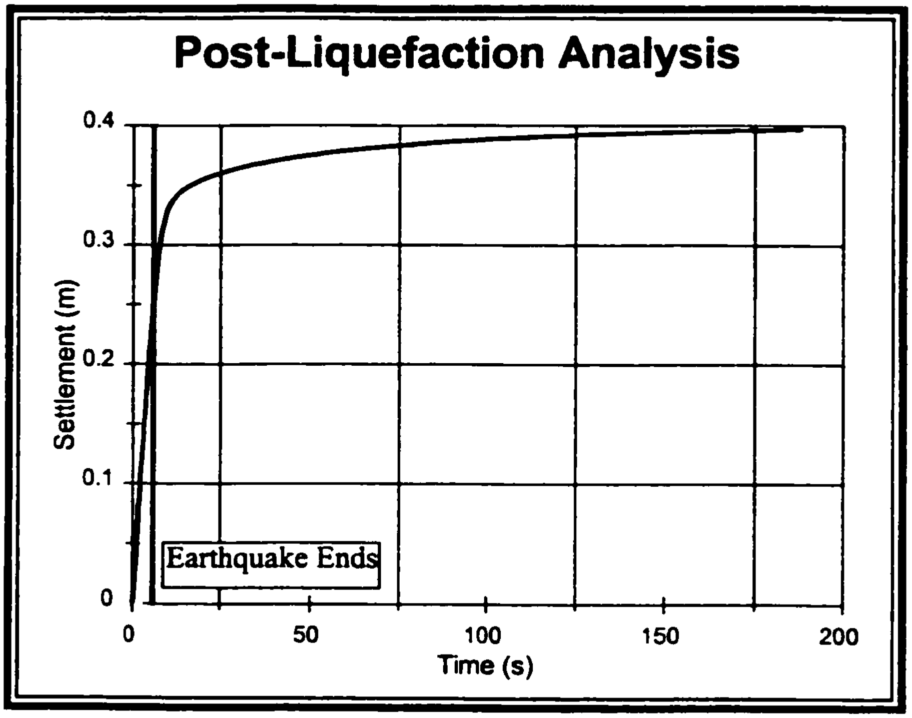

**Figure 5.17:** Surface Settlement

## 5.6 Porosity Distribution in Rotating Cylinder Viscometer

A rotating cylinder viscometer was used to determine the rheological properties of fluidized sand/water mixtures. A discussion of these results was presented in Chapter 3. A basic assumption of that study was that the porosity of the mixture was generally uniform through out the test region. In order to determine the validity of that assumption, a finite element analysis of the experiment was performed using the current model. The reader should note that the following analysis is presented as a demonstration rather than a verification of the model.

The geometry of the device is given in Figure 5.18. It should be noted that, as discussed in Chapter 4, the problem is axi-symmetrical with out of plane velocity components due to the rotating cylinder. The resulting porosity distribution as well as the solid and fluid velocity components are given in Figures 5.19 through 5.21 for steady state conditions.

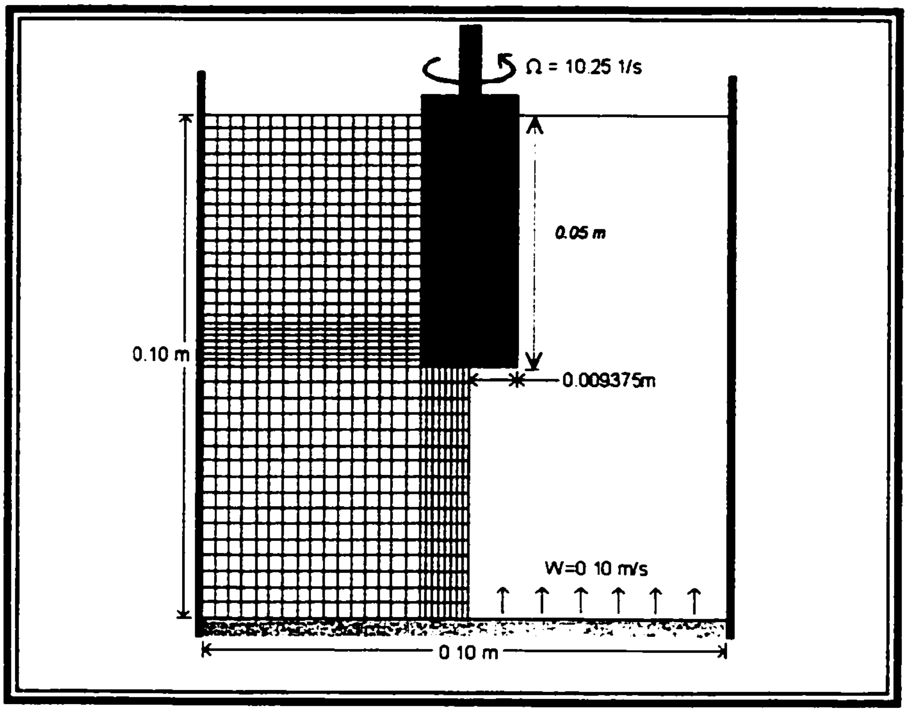

**Figure 5.18:** Rotating Viscometer

Figure 5.19 shows that indeed, the porosity distribution is reasonably uniform in the region of the rotating cylinder. There is a small area in the vicinity of the bottom end of the cylinder where the porosity is nearly unity, indicating that there is little or no sand in that location. This is caused by the disturbance in the fluid flow field from the cylinder. Directly below the cylinder, the fluid velocity is low (see Figure 5.21) causing the sand to "drop" (see Figure 5.20) out of that region. The resulting high porosity in this region is visible in Figure 5.19. To the right side of the cylinder tip, the fluid velocity is comparatively high causing the sand to be "pushed" out of that region.

Another interesting feature of the analysis is the fluid flow profile (see Figure 5.21) in the fully developed region which is clearly very flat. This is contrast to the parabolic shape of a single-component pipe flow (see figure 5.22). The unique shape of the fluid flow in a static, two-component fluidized bed may be attributed to the hydrodynamic drag caused by the sand. Were this not the case, and the fluid had a more parabolic distribution, there would be a great deal of solids circulation with particles flowing upwards in the middle of the bed and downwards towards the sides. This result agrees well with the numerical findings of Durst et al. (1984). The reader should note that the anomalous features of the two-component flow profile at X=0.015m and 0.045m are numerical. These result from the steep flow gradients at the end points. It is anticipated that a finer mesh could reduce these features. Unfortunately, computational limitations prevented the use of a finer mesh.

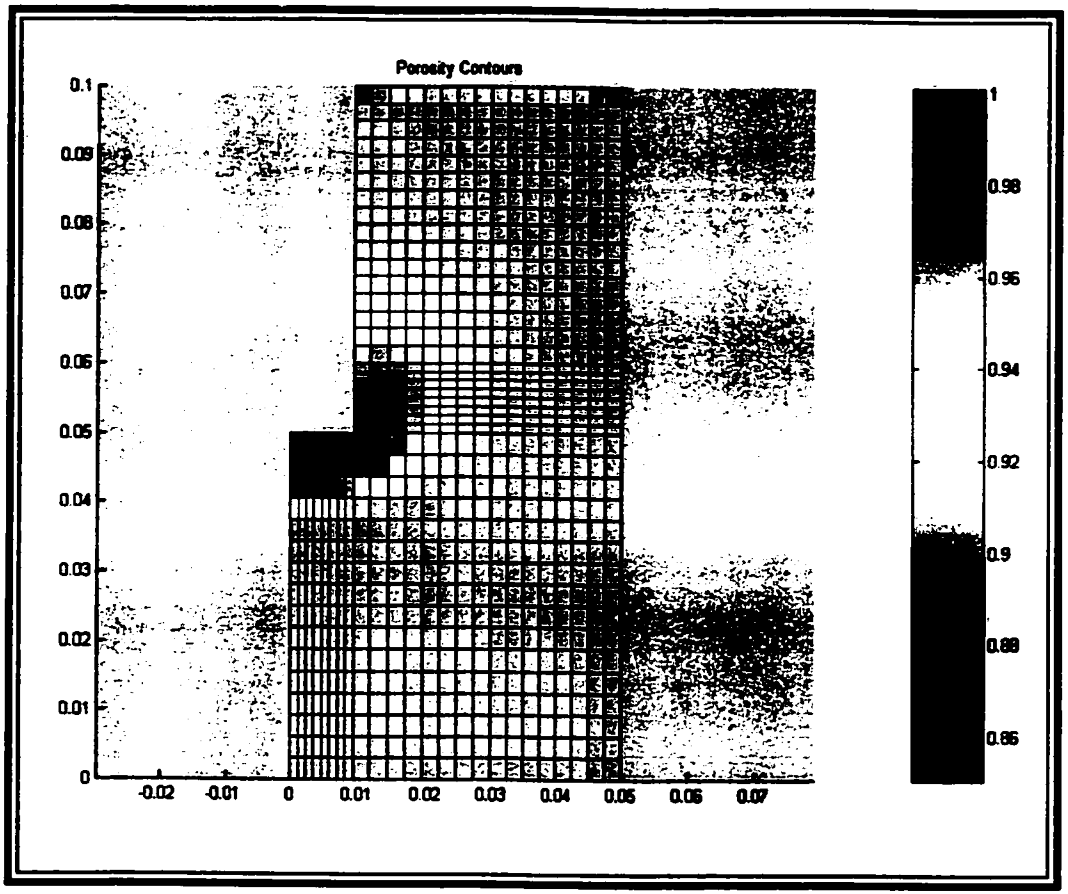

Figure 5.19: Porosity Distribution in Rotating Cylinder Viscometer

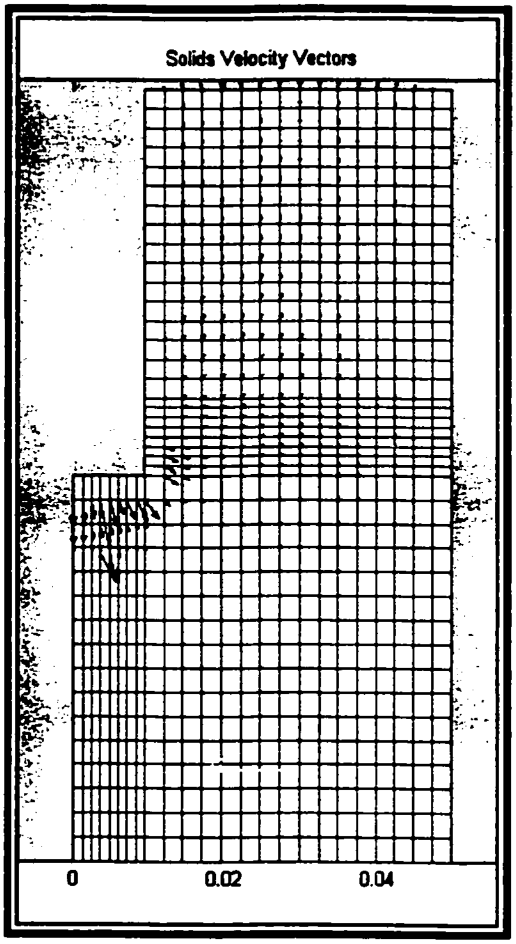

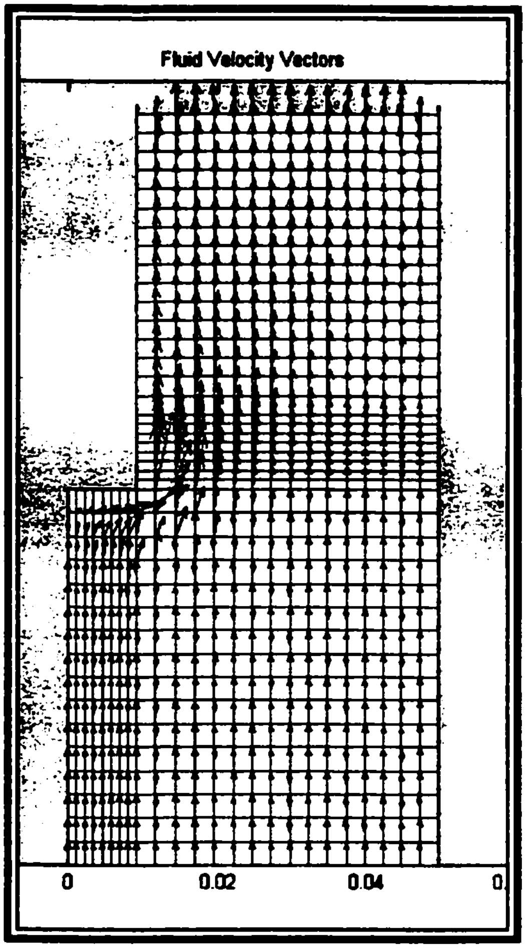

**Figure 5.20:** Solid Component Velocity Profile (scale 30mm = 1.0 cm/s)

**Figure 5.21:** Fluid Component Velocity Profile (30 mm=1.0 m/s)

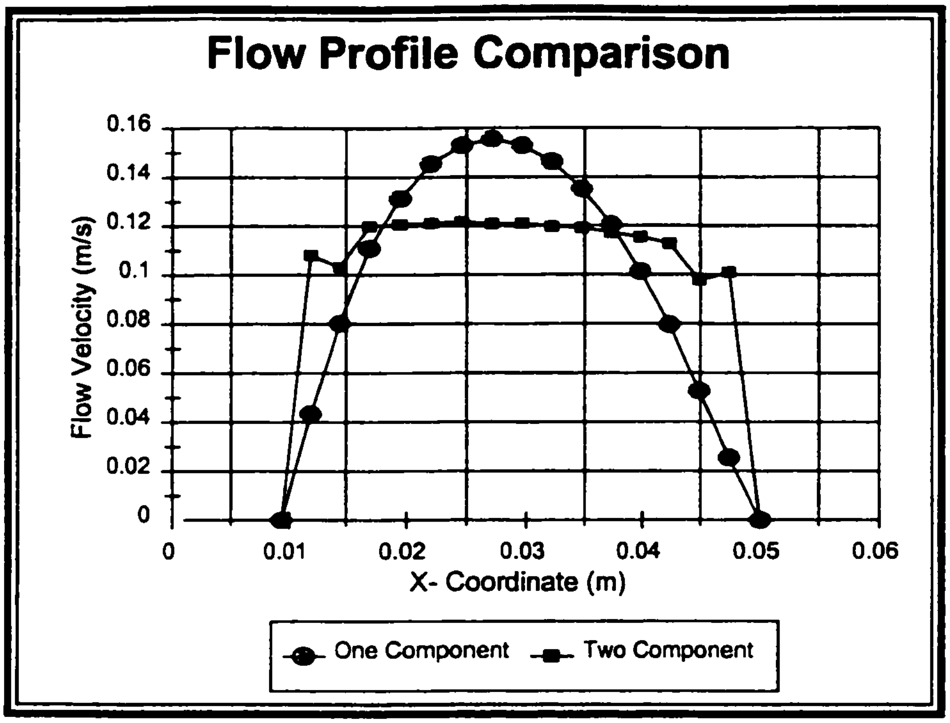

Figure 5.22: Fluid Flow Profile Comparison for One and Two Component Flows

## 5.7 Summary

It has been shown that the model presented in Chapters 2 through 4 is capable of a wide range of analyses of liquid-solid, two component flows. The results of the numerical simulations using the current model compares favorably with experimental and numerical results outlined in this chapter. The types of analyses considered include:

- One-dimensional, transient fluidization
- One-dimensional, transient settlement
- Two-dimensional, transient fluidization
- One-dimensional, transient liquefaction
- One-dimensional, post liquefaction

# NOMENCLATURE

| | |
|---|---|
| $A$ | Granular component compressibility parameter |
| $d_p$ | Representative particle diameter |
| $k$ | Fluidization parameter |
| $n$ | Porosity |
| $\bar{n}$ | Reference porosity |
| $t_1$ | Time to reach steady state |
| $u$ | Granular component velocity |
| $U_l$ | Superficial fluidization velocity |
| $U_l'$ | Fluidization parameter |
| $V_{sx}$ | Solid component velocity in x-direction |
| $v$ | Fluid velocity (section 5.1.2) |
| $v$ | Settling velocity of particles (section 5.2.2) |
| $w$ | Disturbance velocity |

## Greek Symbols

| | |
|---|---|
| $\varphi$ | Sphericity |
| $\rho_s$ | Solid component density |
| $\sigma_{sxy}$ | Shear stress in solid component |

# REFERENCES

Durst, F., Milojevic, D., Schönung, B.
***Eulerian and Lagrangian Predictions of Particulate Two-phase Flows: a Numerical Study***
Appl. Math. Modelling, Vol. 8, pp. 101 - 115

Gidaspow, D.
***Multiphase Flow and Fluidization, Continuum and Kinetic Theory Descriptions***
Academic Press, London, 1994

Liang, W.G., Zhu, J.X.
***A Core-Annulus Model for the Radial Flow Structure in a Liquid-Solid Circulating Fluidized Bed***
Chem. Eng. J., Vol. 68, pp. 51-62, 1997

Pietruszczak, S., Stolle, D.F.E.
***Modelling of Sand Behavior Under Earthquake Excitation***
Int. J. Num. Ana. Geomech., Vol. 11, pp. 221-240, 1987

Shih, Y.T., Gidaspow, D., Wasan, D.T.
***Sedimentation of Fine Particles in Nonaqueous Media***
Colloids and Surface, Vol. 21, pp. 393 - 429, 1986

Slis, P.L., Willemse, T.W., Kramers, H.
***The Response of the Level of a Liquid Fluidized Bed to a Sudden Change in the Fluidizing Velocity***
App. Sci. Res., Sec. A, Vol. 8, pp. 209 - 218, 1958

Thelen, T.V., Ramirez, W.F.
***Modelling of Solid-Liquid Fluidization in the Stokes Flow Regime Using Two-Phase Flow Theory***
A.I.Ch.E.J., Vol. 45, pp. 708 - 723, 1999

# 6 CONCLUDING REMARKS AND RECOMMENDATIONS

## 6.1 Summary

The scope of this thesis is to present a framework for studying the flow of liquefied and fluidized materials. In the preceding chapters, the results of investigations on the constitutive and finite element modelling of liquefied (and fluidized) liquid/solid mixtures have been outlined.

There are five main contributions stemming from the work detailed herein, which have been presented in Chapters 2 through 4. Chapter 5 confirms the utility of these contributions through comparison of results from the numerical model to experimental and numerical results of others.

Chapter 2 begins by developing the Navier-Stokes equations for a single component fluid. This is followed by an extension of these principles to a two component fluid wherein the solid component is treated as a continuous media. The fundamental unknowns of these equations for two component flow are:

- The solid component velocity
- The fluid component velocity
- The fluid pressure
- The porosity of the solid component

Stemming from the basic hydrodynamic equations are several secondary unknowns in addition to the four fundamental ones. To solve these equations, closure relations have been provided, which make the secondary unknowns functions of the fundamental variables. The need for these closure equations is identified in Chapter 2.

Finally, through preliminary analyses, the author observed that numerical solutions of the hydrodynamic equations can be difficult or impossible to achieve due to numerical stability problems. A revised set of equations is presented in which the solid and fluid component velocities are substituted by two new variables. This revised equation set is shown to be stable and solutions can be found. This revised set of equations constitutes the first contribution of the thesis.

Chapter 3 focuses on the closure equations, the need for which was identified in the second chapter. The two components are strongly coupled via the hydrodynamic drag between the fluid and the granular solid particles. Owing to the thoroughness and success of previous work on this phenomenon, the drag model used in this work has been taken from published literature.

The shear stress in the solid component presented the most significant challenge of the thesis. The shear stress in dilute two component mixtures is discussed first. Owing to the uniqueness of the behavior in dilute mixtures, an experimental investigation was performed on mixtures of a particular sand type in water. An apparatus was designed and fabricated for this investigation that allowed a Brookfield type viscometer to be immersed in a fluidized bed. A new correlation, that achieves a coefficient of determination of over 97%, is presented for this mixture, indicating an excellent fit of the data. The data also compared favorably to previous studies using more complex measurement techniques. When the porosity of the mixture is reduced to a particular threshold, a Newtonian description of the shear stress no longer applies. A simple constitutive model presented in the literature was adopted when such conditions apply.

Finally, owing to the particulate nature of the solid component, a model of its volumetric strain behavior is critical to capturing both the consolidation and liquefaction phenomena. A novel model for the solid component pressure is presented based on the use of porosity as a state variable. The pressure in the solid component is assumed to be a function of the difference between the current porosity and a reference porosity. Furthermore, Artificial Neural Networks (ANN) are used to determine the variation of the reference porosity in the presence of shear strain. The use of this novel model and the ANN represent two further contributions of the thesis.

Chapter 4 is primarily concerned with the formulation of the finite element equivalents of the revised hydrodynamic equations. In keeping with the presentation of the second chapter, the finite element equations for a single component fluid are presented first. These are followed by the extension to a two component mixture. Owing to the numerically stable form of the revised equation set, it is shown that standard Galerkin techniques are sufficient for generating the finite element equations. This contrasts with the use of complex stabilizing schemes and staggered grid techniques others have used to solve the basic hydrodynamic equations. Chapter 4 also outlines a manipulation of the revised equation set that permits, for certain circumstances, the equations to be reduced from four in number to one. The use of such a reduction has clear computational benefits and this manipulation represents the final contribution to the thesis.

To the model presented in Chapters 2 through 4, results from the numerical model were compared to experimental and numerical results of others. To this end, Chapter 5 contains five examples of applications for the model. Simulations using the current model are compared with experimental results on transient fluidization in one and two dimensions, and one-dimensional settlement. Finally, the full capacity of the model has been verified in analyzing liquefaction of a one-dimensional soil deposit and the results are compared to previously published numerical predictions. In all cases, the model was found to provide reasonable predictions.

## 6.2 Recommendations

As with all things, a thesis must come to an end, even when there remains several questions which remain partially answered. Of course these questions may lead to extensions of the work by others in the future.

Some questions, which remain to be answered, are:

1) Quantifying the mass diffusion in the solid component due to gradients of porosity (Chapter 2)
2) Providing a mechanistic explanation for the rheological behavior of dilute two component, liquid/solid mixtures (Chapter 3)
3) Improving the efficiency of the finite element solution method for the current model to allow more complex simulations to be performed (Chapter 4)
4) Using the current model to simulate two-dimensional post-liquefaction events.